

PHYSICS STUDIES

EDITED BY

Mehriban EMEK

AUTHORS

Belgin TUNALI

Cristian Ştefan DUMITRIU

Deniz TÜRKÖZ ALTUĞ

Firdevs Banu ÖZDEMİR,

H. Eslem GULER

Mehmet KABAK

Mecit ÖGE

Murat KIRANŞAN

Neslihan KAYA KINAYTÜRK

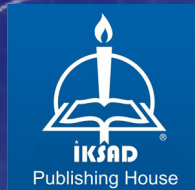
Okan ÇİÇEK

Rabia CAGLAYAN

Selcuk TOPAL

Tuba ÖZDEMİR ÖGE

Yesim MOGULKOC



PHYSICS STUDIES

EDITED BY

Mehriban EMEK

AUTHORS

Belgin TUNALI

Cristian Ştefan DUMITRIU

Deniz TÜRKÖZ ALTUĞ

Firdevs Banu ÖZDEMİR,

H. Eslem GULER

Mehmet KABAK

Mecit ÖGE

Murat KIRANŞAN

Neslihan KAYA KINAYTÜRK

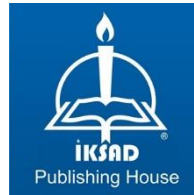
Okan ÇİÇEK

Rabia CAGLAYAN

Selcuk TOPAL

Tuba ÖZDEMİR ÖGE

Yesim MOGULKOC



Copyright © 2021 by iksad publishing house
All rights reserved. No part of this publication may be reproduced,
distributed or transmitted in any form or by
any means, including photocopying, recording or other electronic or
mechanical methods, without the prior written permission of the publisher,
except in the case of
brief quotations embodied in critical reviews and certain other
noncommercial uses permitted by copyright law. Institution of Economic
Development and Social
Researches Publications®
(The Licence Number of Publisher: 2014/31220)
TURKEY TR: +90 342 606 06 75
USA: +1 631 685 0 853
E mail: iksadyayinevi@gmail.com
www.iksadyayinevi.com

It is responsibility of the author to abide by the publishing ethics rules.
Iksad Publications – 2021©

ISBN: 978-625-7562-96-6
Cover Design: İbrahim KAYA
September / 2021
Ankara / Turkey
Size = 16x24 cm

CONTENTS

PREFACE

Mehriban EMEK.....1

CHAPTER 1

MOLECULES IN THE UNIVERSE

Selcuk TOPAL.....3

CHAPTER 2

THE MOLECULAR GAS, DUST AND STELLAR POPULATION ACROSS THE DISK OF SPIRAL GALAXIES

Selcuk TOPAL.....43

CHAPTER 3

ON THE COPPER-BASED MATERIALS CORROSION

Cristian Ştefan DUMITRIU.....67

CHAPTER 4

PRINCIPLES AND ENVIRONMENTAL APPLICATIONS OF THE SONOCHEMISTRY AND SONOCHEMICALLY ASSISTED ADVANCED OXIDATION PROCESSES

Murat KIRANŞAN.....101

CHAPTER 5

FUNDAMENTALS OF OPHTALMIC LENS DECENTRATION

*Tuba ÖZDEMİR ÖGE & Firdevs Banu ÖZDEMİR &
Mecit ÖGE & Okan ÇİÇEK*.....129

CHAPTER 6

ELECTRONIC STRUCTURE PROPERTIES OF BSb/Ga₂SSe HETEROSTRUCTURE UNDER ELECTRIC FIELD EFFECT

*H. Eslem GULER & Rabia CAGLAYAN & Mehmet KABAK &
Yesim MOGULKOC.....149*

CHAPTER 7

INVESTIGATION OF THE EFFECT OF LAMBDA CYHALOTHRIN ON SOME EGGSHELLS AS WASTE MATERIAL USING AFM IMAGING AND UV-VIS SPECTROSCOPY

*Neslihan KAYA KINAYTÜRK & V Belgin TUNALI &
Deniz TÜRKÖZ ALTUĞ.....163*

PREFACE

It is an honor for us to present the book named Physics Studies. We are happy to contribute to the interenational scientific studies mentioned in this book.

This book was published for the first time and prepared in chapters. The book consists of seven chapters explaining new and current issues. It is a professional book in the field of physics with important methods and applications.

This study contains very valuable studies by Assist. Prof. Dr. Selcuk Topal (Molecules in the Universe; The Molecular Gas, Dust and Stellar Population Across the Disk of Spiral Galaxies); Dr. Cristian Stefan Dumitriu (On the Copper-Based Materials Corrosion); Assist. Prof. Dr. Murat Kiransan (Principles and Environmental Applications of Sonochemistry and Sonochemically Assisted Advanced Oxidation Processes); Assoc. Prof. Dr. Tuba Ozdemir Oge, Asst. Prof. Dr. Firdevs Banu Ozdemir, Res. Asst. Dr. Mecit Oge and Inst. Okan Cicek (Fundamentals of Ophtalmic Lens Decentration); H. Eslen Guler, Rabia Caglayan, Prof. Dr. Mehmet Kabak and Assoc. Prof. Dr. Yesim Mogulkac (Electronic Structure Properties of BSb/Ga₂SSe Heterostructure Under Electric Field Effect); Assist. Prof. Dr. Neslihan Kaya Kınayturk, Prof. Dr. Belgin Tunalı, Assist. Prof. Dr. Deniz Turkoz Altug (Investigation of the Effect of Lambda Cyhalothrin on Some Eggshells as Waste Materials Using AFM Imaging and UV-VIS Spectroscopy).

We would like to thank the managers and employees of IKSAD Publishing for their careful and patient work during the arrangement, typesetting and printing of the book named Physics Studies.

Assist. Prof. Dr. Mehriban EMEK¹

¹Adiyaman University, Golbası Vocational High School, Department of Computer Technologies, memek@adiyaman.edu.tr

CHAPTER 1

MOLECULES IN THE UNIVERSE

Assist. Prof. Selçuk TOPAL¹

¹Yüzüncü Yıl University, Faculty of Science, Department of Physics, Van, Turkey.
selcuktopal@yyu.edu.tr ORCID ID: 0000-0003-2132-5632

INTRODUCTION

At the beginning of the 20th century, there was still no consensus on the true shape of our galaxy and whether there are any other galaxies in the universe. Heber D. Curtis and Harlow Shapley had a debate to understand our place in the universe better (i.e. Great Debate; Shapley & Curtis 1921; Trimble 1995). Although Shapley and Curtis were not right at all aspects that they defended, the Great Debate was surely led us to question our place in the universe like never before.

Thanks to the studies that coincided with the same period, we realized that the universe is expanding as opposed to Einstein's idea of a static universe (Friedmann 1924; Lemaître 1927; Hubble 1929). By the power of the developing telescope in the first quarter of the 20th century, we had begun to realize that there are many galaxies of different evolutionary types in the universe (Hubble 1936; de Vaucouleurs et al. 1991; Kormendy & Bender 2012). At the beginning of the 20th century, not only the structure of the universe but also star formation (SF) was not well understood compared to what we know today. Until the 1970s, the universe was thought to be mostly atomic. Although some discoveries before 1970 gave some clues on the possible existence of molecules in the interstellar medium (ISM), it was in the 1970s that an increasing number of molecules began to be discovered in the ISM (Swings & Rosenfeld 1937; Wilson et al. 1970; Penzias et al. 1971; Solomon et al. 1971). Today more than 200

molecules have been discovered in the ISM². Molecules are the key to understand not only SF but also the structure and evolution of galaxies.

Hydrogen (H) is the most abundant element in the universe and it tends to be molecular (H₂) in cold and dense star-forming regions. H₂, the fuel for SF, is the key molecule that leads other molecules to form in the ISM. Putting all the complexity of SF aside (for now), we can roughly say that supersonic turbulence, radiation field in the medium, irregularities in the gravitational field, and some other physical and/or mechanical energy inputs could cause the gas clouds to compress and break up into fragments which can trigger SF (McKee & Ostriker 2007). In addition, other atoms, ions and molecules found in abundance in the ISM after H₂ could also help the gas clouds to cool down more quickly and collapse inward. However, please note that the ability of an atom, ion or molecule to be a dominant coolant in the ISM depends on many parameters, such as the chemical composition of the medium, its average temperature, density, the presence of dust acting as a shield against the interstellar radiation field, and also the optical depth of the gas. For example, if the carbon monoxide (CO) is abundant in the medium, it may become a dominant coolant in dense ($n_{H_2} \geq 10^3 \text{ cm}^{-3}$) clouds with the right temperature ($T < 100 \text{ K}$). However, in regions with higher temperatures ($T > 100 \text{ K}$) and more H₂ dominating the chemical composition, H₂ can act as an important coolant instead (Klessen & Glover 2016; Girichidis et al. 2020).

² <https://zeus.ph1.uni-koeln.de/cdms/molecules>

Molecular emissions, therefore, have a vital role in SF. However, as the studies of our own galaxy and other galaxies indicated, not every molecular cloud bright in CO emission forms stars, and 40% – 50% of such molecular clouds are in diffuse phase, i.e. hydrogen molecule column density of $N_{H_2} < 10^{22} cm^{-2}$ (Goldsmith et al. 2008; Liszt et al. 2010; Roman-Duval et al. 2016). This indicates that a significant portion of molecular clouds does not form stars.

SF involves many variables, and the star formation rate (SFR) could be different in different scales from individual molecular clouds to the whole disk across a galaxy. To fully understand the evolution of galaxies, we first need to understand SF and the physical properties of the ISM driving it. The Kennicutt-Schmidt (*KS*) law, first discovered using HI observations (Schmidt 1959) and then molecular gas observations (Kennicutt 1998), represents the relationship between total gas (HI+H₂) surface density, $\Sigma_{gas} [M_{\odot} pc^{-2}]$, and the SFR surface density, $\Sigma_{SFR} [M_{\odot} yr^{-1} kpc^{-2}]$, and expressed as follows (Kennicutt 1998).

$$\Sigma_{SFR} = A \Sigma_{gas}^N \quad (1)$$

$$\Sigma_{SFR} = (2.5 \pm 0.7) \times 10^{-4} \left(\frac{\Sigma_{gas}}{1 M_{\odot} pc^{-2}} \right)^{1.4 \pm 0.15} \quad (2)$$

where $N \approx 1 - 2$ and A represents the absolute SFR efficiency. As the relation states, there is a linear relationship between these two parameters, i.e. as the gas surface density increase, SFR also increases (Figure 1). This supports the idea that gas clouds cool down by molecular emissions, and this triggers SF causing an increase in SFR.

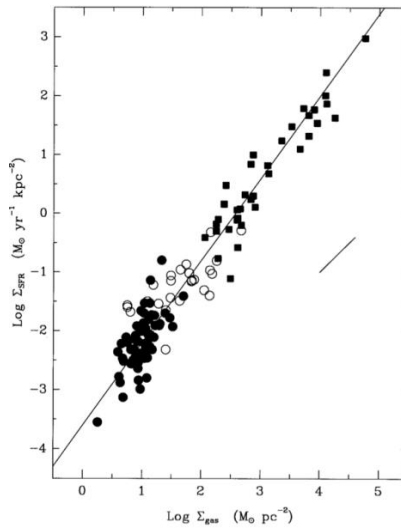


Figure 1: Kennicutt-Schmidt Law³. Credit: Kennicutt 1998.

In *KS* law, the values of N depends on many factors, such as angular resolution, the fitting method, the tracer used to estimate SFR (e.g. H_α or infrared), gas surface density, and difference in atomic and molecular constituents of the gas clouds (Kennicutt et al. 2007; Bigiel et al. 2008; Krumholz et al. 2009). The studies on *KS* law also support the scenario that a large portion of gas clouds is in diffuse phase, and

³ Filled black circles and squares indicate normal and starburst galaxies, respectively. Open black circles represent the values in the center of normal spirals. Fit shown by black solid line has a slope of $N=1.4$.

does not form stars (Heiderman et al. 2010; Krumholz et al. 2012).

Molecular emission lines are one of the most useful tools to study many cosmic phenomena, from SF to the structure of galaxies and the universe. Given its readily observable rotational transitions, CO is one of the most important molecules. In the following sections, such studies will be discussed with the addition of some new data sets⁴.

1. FORMATION OF H₂ AND ADVANTAGES OF USING CO MOLECULE

When the universe was about 100.000 years old (i.e. before the first galaxies at around $z \sim 2500$) H₂ was formed through different processes compared to today's H₂ formation scenario (Tytler et al. 2000; Lepp & Dalgarno 2002; Hirata & Padmanabhan 2006). Although H₂ forms slowly and in low abundance in the early universe by following different paths (through H^- , H_2^+ and HeH^+ mechanisms; Hirata & Padmanabhan 2006), the molecules started to form at an increased rate as the universe continued to expand and cool. Based on the Standard Big Bang Nucleosynthesis Model, the decrease in temperature caused the matter and radiation to be separated in the early universe. The universe, therefore, became neutral compared to its initial ionized (Wagoner et al. 1967; Boesgaard & Steigman 1985; Cyburt et al. 2016). The neutral atoms (particularly HI) triggered the

⁴ This review/research article is a first in Turkish astronomy and aims to convey the most up-to-date information for future astronomers/astrophysicists who may work in the field.

chemical reactions, and therefore molecules began to form in the universe (Figure 2).

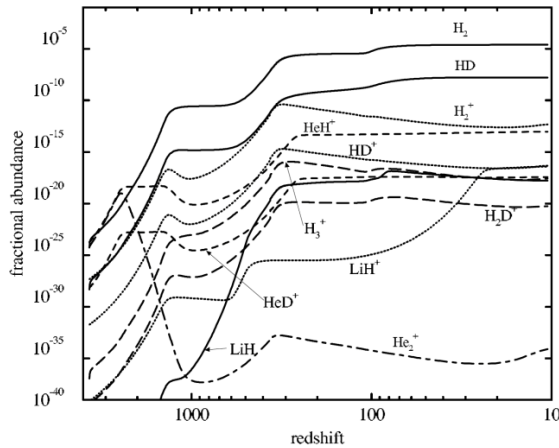


Figure 2: Molecular Abundance in the Early Universe.
Credit: Lepp and Dalgarno 2002

Given the currently observed abundance of H_2 , we now know that H_2 forms on the surfaces of dust grains rather than by a direct combination of two hydrogen atoms in space (Gould & Salpeter 1963; Hollenbach, Werner & Salpeter 1971; Duley 1996; Cazaux & Tielens 2002, 2004; Perets & Ofer 2006). The dust grains, about μm in size, act as a catalyst. In this scenario, the structure and temperature of the dust grains play a vital role (Perets & Ofer 2006).

Although H_2 is by far the most copious molecule in the ISM, it is extremely hard to observe it directly. Therefore, the first molecules detected in the ISM was not H_2 but CN , CH , CH^+ , OH and NH_3 (Dunham 1937; Swing & Rosenfeld 1937; McKellar 1940; Douglas &

Herzberg 1941; Weinreb et al. 1963; Cheung et al. 1968). The first detection of H₂ at far-ultraviolet (FUV) wavelength was in 1970 (Carruthers 1970).

The difficulty of direct observation of H₂ in star-forming regions is due to its quantum structure. Since H₂ is a homo-nuclear diatomic molecule (that is, its electric dipole moment is zero), electronic transitions between $J = 1 \rightarrow 0$ energy levels do not occur. Although the $J = 2 \rightarrow 0$ transition can take place, the temperature required for this (~ 500 K) is much higher than the average temperature of star-forming cold gas clouds (~ 10 K). However, the difference between the energy levels of the CO molecule is very small compared to H₂, and it can shine brightly even in cold star-forming gas clouds (Krumholz 2011). CO, therefore, is one of the most useful molecules to indirectly probe the physics of the molecular clouds.

The formation of H₂ on dust surfaces has led to the formation of other molecules. In our galaxy, there is roughly 1 CO molecule in every 10000 H₂ in the ISM (Lee et al. 1996), making CO the second most abundant molecule after H₂. CO is, therefore, widely used to probe the gas clouds indirectly. Other molecules tracing the dense gas, such as HCN, HCO⁺, HNC, and HNCO, are used to study the denser regions of the gas clouds. Some of the major extragalactic CO surveys (also including some high-density tracers) are listed in Table 1.

Table 1: Some Extragalactic CO (and also HCN, HCO⁺ and HNC) Surveys.

Name	Transition	Telescope*	Resolution (arcsec)	Number of galaxy	Method**	Ref.***
FCRAO CO Survey	¹² CO(1-0)	FCRAO 10m	45	300	SD-MP	1
The BIMA Survey of Nearby Galaxies (BIMA SONG)	¹² CO(1-0)	BIMA NRAO 12m	6	44	SD+IM	2
Nobeyama CO Atlas of Nearby Galaxies	¹² CO(1-0)	Nobeyama 45m	15	40	SD-OTF	3
The HERA CO-Line Extragalactic Survey (HERACLES)	¹² CO(2-1)	IRAM 30m	13	18	SD-OTF	4
An Extragalactic CO(3–2) Survey With The Heinrich Hertz Telescope (HHT)	¹² CO(3-2)	HHT 10m	22	125	CP	5
The James Clerk Maxwell Telescope (JCMT) Nearby Galaxies Legacy Survey (NGLS)	¹² CO(3-2)	JCMT 15m	14,5	155	SD-RJM	6
CO Multi-line Imaging of Nearby Galaxies (COMING)	¹² CO(1-0), ¹³ CO(1-0), ¹² C ¹⁸ O(1-0)	Nobeyama 45m	17	147	SD-OTF	7
EMPIRE: The IRAM 30 m Dense Gas Survey of Nearby Galaxies	HCN(1-0) HCO ⁺ (1-0) HNC(1-0) ¹² CO(1-0)	IRAM 30m	25-34	9	SD-OTF	8

* FCRAO: Five College Radio Astronomical Observatory; BIMA: Berkeley-Illinois-Maryland Association; IRAM: the Institute for Radio Astronomy in the Millimeter Range; HHT: Heinrich Hertz Submillimeter Telescope; JCMT: James Clerk Maxwell Telescope.

** SD-MP: Single-dish Multiple Pointing, SD+IM: Single-dish and Interferometric Map, SD-OTF: Single-dish On-The-Fly Mapping, CP: Central pointing, SD-RJM: Single-dish Raster/Jiggle Map Mode.

***(1) Young et al. 1995; (2) Helfer et al. 2003; (3) Kuno et al. 2007; (4) Leroy et al. 2009; (5) Mao et al. 2010; (6) Wilson et al. 2012; (7) Sorai et al. 2019; (8) Jiménez-Donaire et al. 2019.

2. EFFECTS OF STAR FORMATION ACTIVITIES ON THE PHYSICS OF MOLECULAR CLOUDS

Young and massive stars fill the ISM with ultraviolet (UV) radiation. Studies have shown that UV radiation can have both positive and negative effects on SF (Medina et al. 2014, Kim, Kim & Ostriker 2018). CO abundance could also be affected by UV radiation (van Dishoeck & Black 1988; Bialy & Sternberg 2015). There is a strong connection between UV and infrared (IR) emission. Dust heated by strong UV radiation emits in the IR region in a range from a few μm to several hundred μm . Among these, $24\mu\text{m}$ dust emission is important as it correlates well with the SFR (Calzetti et al. 2005). On the other hand, while the ratio between the far-infrared (FIR) and FUV flux densities can give us information about the extinction and SF efficiency (SFE), it can correlate with many other parameters, such as heavy element abundance, distance from the galaxy center, molecular gas mass and radiation field throughout the galaxy's disk (e.g. Dale et al. 2007; Topal 2020).

Other IR band emissions that provide valuable insights on stellar populations are $3.6\mu\text{m}$ and $4.5\mu\text{m}$ emissions. The source of $3.6\mu\text{m}$ emission, which is hardly affected by interstellar extinction, maybe the old stars and/or dust grains heated by strong FUV radiation. On the other hand, $3.3\mu\text{m}$ polycyclic aromatic hydrocarbon (PAH) dust emission close to the $3.6\mu\text{m}$ region can contaminate the old stellar light observed in the $3.6\mu\text{m}$ region by 5% – 15% (Meidt et al. 2012). The values of $[3.6] - [4.5]$ color are in the range of $-0.2 < [3.6] -$

$[4.5] < 0$ for old stellar populations. Because strong CO absorption occurs in the $4.5\mu\text{m}$ region, which causes a decrease in emission at that wavelength (Peletier et al. 2012). As a result, $[3.6] - [4.5]$ color becomes bluer (Wilner et al. 2004; Pahre et al. 2004; Peletier et al. 2012; Meidt et al. 2014). On the other hand, $[3.6] - [4.5]$ color is almost always positive for dust emission, i.e. emission not directly originating from old stellar atmospheres (Querejeta et al. 2015).

FUV radiation has significant effects on the physics and chemistry of interstellar gas clouds. Intense FUV radiation can create a photon-dominated region (PDR) in the near-surface of HI gas clouds, while intense X-ray radiation can reach much deeper into the cloud to form an X-ray dominated region (XDR) (Hollenbach & Tielens 1999; Maloney, Hollenbach & Tielens 1996; Meijerink, Spaans & Israel 2007).

Cosmic radiation (CR) also provides another energy input to the ISM and has a significant impact on the physics of the medium. CRs are high-energy relativistic particles with energies ranging from 100 MeV to 1 TeV. CRs with relatively low energy (~ 100 MeV) are responsible for ionization in the ISM and could ionize H_2 to form H_3^+ (Indriolo & McCall 2012). Molecules such as OH and HCO^+ found in dense parts of the gas clouds are sensitive to CRs. The CRs have more effects on diffuse atomic or molecular gas with relatively low column density compared to its effects on denser gas (Padovani et al. 2009). Supernova remnants (SNRs) are also an essential source of CRs (Costagliola et al. 2011). However, the CR source at the center of

active galaxies could be the active galactic nuclei (AGN) itself (Ferrari 1998; Achterberg et al. 2001; Guo & Mathews 2011). As a result, there are CR-dominated regions (CRDRs) besides the PDRs and XDRs in galaxies. Such diversity of radiation sources can dramatically change the chemical composition of the medium.

Since each molecular transition requires different physical conditions to excite, having data of multiple CO transitions gives valuable insights on SF activity in galaxies. There is a relationship between the turning point (i.e. J_{max}) on the CO spectral line energy distribution, (SLED) based on multiple CO transitions and the SFE. In regions with high SF, J_{max} occurs at higher transitions of CO, while the opposite is true in regions with low SF. For example, it varies between $J_{max} \approx 6 - 7$ in the central regions of galaxies NGC 253 and M82, which show extreme SF in the nearby universe (Bayet et al. 2004; Weiß, Walter & Scoville 2005). It can reach the value of $J_{max} \approx 9$ in galaxies with high SFR located at $z \approx 4$ (Weiss et al. 2007). On the other hand, the physics of molecular clouds in the center of a galaxy could also be different than that in the arms and inter-arms. As a result, the value of J_{max} for the central region of a galaxy could be different than the value determined for a region located in the arms (Figure 3). As an example, an extremely star-forming region Orion located in our own galaxy could have $J_{max} \approx 13$ (Habart et al. 2010), while it is $J_{max} \approx 4$ in the central region of our galaxy (Fixsen, Bennett & Mather 1999).

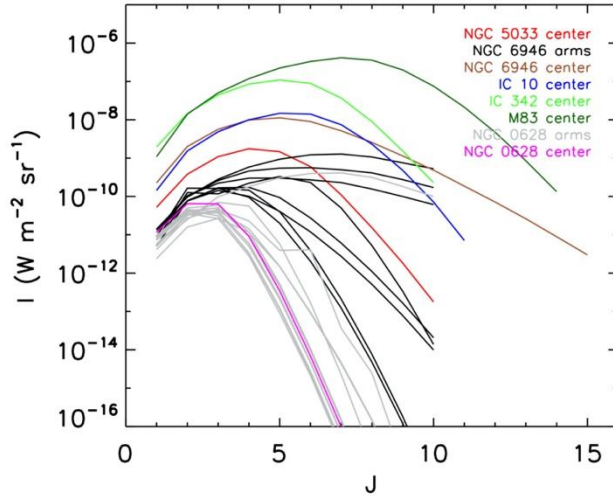


Figure 3: CO Spectral Line Energy Distribution (SLED) for some spiral galaxies. The data for the spiral galaxy NGC 5033 (red) were taken from Topal 2021, and the data for NGC 6946 (brown), M83 (dark green), IC10 (blue) and IC342 (green) galaxies were taken from Bayet et al. 2006. The data for the disk of NGC 6946 (black) were taken from Topal et al. 2014. The model data for the center (magenta) and the disk of NGC 0628 (gray) belong to this study.

As seen in Figure 3, J_{max} can have different values in different galaxies, and even at different locations over the same galaxy. The SLEDs based on the best-fitting model data shown in Figure 3 were obtained using the line ratios of multiple CO transitions and the same radiative transfer code (RADEX; see Chapter 6).

On a different note, there is a relationship between the CO line width and the bolometric luminosity of young stellar objects (YSOs) during the early stage of stellar evolution (Wang 2009). Young stellar objects with high luminosity ($> 10^3 L_{\odot}$) tend to be associated with molecular clouds with greater mass and higher turbulence (Wang ,2009).

3. H₂ MASS

Given the difficulties in detecting H₂ in the ISM, there are some other tracers used to calculate the total H₂ mass, M_{H_2} , in the gas clouds. CO is a well-known indirect probe for the physics of molecular clouds. To estimate the H₂ mass CO-to-H₂ conversion factor ($X_{CO} = \frac{N_{H_2}}{W_{CO}}$, where N_{H_2} is the hydrogen column number density and W_{CO} is the integrated CO line intensity) should be known. However, X_{CO} is not the same for all galaxies, and it could also change across the disk of the same galaxy based on the region of interest, i.e. the center, arms, inter-arms. Most information on X_{CO} we know comes from Galactic studies. Based on such and some other extragalactic studies, the value of $X_{CO} = 2 \times 10^{20} \text{ cm}^{-2} (\text{K km s}^{-1})^{-1}$ is considered a reasonable value for our own galaxy and nearby spiral galaxies (Dame, Hartmann & Thaddeus 2001; Rosolowsky et al. 2003; Bolatto et al. 2008; Abdo et al. 2010; Donovan Meyer et al. 2012; Bolatto, Wolfire, & Leroy 2013). X_{CO} could also be defined as the ratio of M_{H_2} to the CO luminosity, L_{CO} , i.e. $\alpha_{CO} = M_{gas}/L_{CO}$. The relationship between X_{CO} and α_{CO} can be written as follows (Narayanan et al. 2012),

$$X_{CO} [\text{cm}^{-2}(\text{K kms}^{-1})^{-1}] = 6.3 \times 10^{19} \times \alpha_{CO} [M_{\odot}\text{pc}^{-2}(\text{K kms}^{-1})^{-1}] \quad (3)$$

The value of X_{CO} could be 5 to 10 times lower at the center of galaxies (Bolatto et al. 2013; Sandstrom et al. 2013). The reasons for the central depression in X_{CO} could be some physical characteristics typically seen in the center of galaxies, such as high excitation

temperature, strong turbulence, high density, effects of CRs, heavy element abundance and velocity dispersion (Stacey et al. 1991; Downes & Solomon 1998; Narayanan et al. 2011).

Using the integrated CO line intensity the M_{H_2} could be calculated using the expression below (Bolatto et al. 2013).

$$M_{H_2} = 1.05 \times 10^4 \left(\frac{X_{CO}}{2 \times 10^{20} \frac{\text{cm}^{-2}}{\text{K km s}^{-1}}} \right) \frac{S_{CO} \Delta_v D_L^2}{1+z} \quad (4)$$

where $S_{CO} \Delta_v$ represents the CO intensity in the unit of Jy K kms⁻¹, D_L is the luminosity distance in the unit of Mpc and z is the redshift. IR data could also be used to calculate M_{H_2} (Gratier et al. 2017).

H₂ correlates with many physical properties. How efficiently H₂ clouds could form stars depends on the abundance of heavy elements in the medium (Gardan et al. 2007; Hunt et al. 2015), and the amount of M_{H_2} (also gas surface density ΣH_2) could change across the disk of a galaxy, i.e. M_{H_2} decreases from the center to the outskirts (e.g. Gardan et al. 2007; Topal 2020, 2021). The studies show that there is a close relation between ΣH_2 and SFR (Schruba et al. 2011). However, the relationship between SF and ΣH_2 could depend on the location over the galaxy's disk, and it could show a radial gradient (Schinnerer et al. 2013). There is also a positive correlation between M_{H_2} and the ratio of 24 μm / FUV (i.e. the extinction) in galaxies (e.g.

Topal 2021). The physics of H_2 , the fuel for SF, depends on many factors, such as the abundance of heavy elements, position over the galaxy, presence of young massive stars or supernova explosions in the vicinity, all contributing to the complexity of SF processes in galaxies.

4. MOLECULAR TRANSITIONS AS A KINEMATICAL TRACER IN GALAXIES

4.1. Intensity Map and Position Velocity Diagram

It is not trivial to study the kinematics of external galaxies and their stellar populations since such galaxies are located at large distances, causing a lower angular resolution. It is, therefore, almost impossible to observe an individual star in external galaxies. We, therefore, need to use some other proxies instead to be able to study stars in external galaxies.

By studying the kinematics of molecular gas clouds we can probe whether the galaxy had a past merger and/or collision with other galaxies nearby. During such minor collisions, some part of the gas clouds could not be affected by that and falls back to the galaxy's disk. However, major collisions could create larger shock waves ejecting the gas at large distances although the gas may still fall back to its original location over the galaxy (Mazzuca et al. 2006; Eliche-Moral et al. 2010). Any orbital irregularities caused by such collisions could be tracked down using atomic, molecular and ionized gas observations. As an example, Davis et al. (2011a) used optical, CO

and HI data obtained for fast-rotating early-type galaxies (ETGs) taken from a larger sample of CO bright ETGs (ATLAS^{3D}; Cappellari et al. 2011). It has been found that the gas in 36% of the selected ETGs has an external origin, i.e. galactic collisions and/or cold gas flow into the galaxy's disk (Davis et al. 2011a).

4.2. CO Tully-Fisher Relation

The Tully-Fisher Relation (TFR; Tully & Fisher 1977) states that there is a relationship between the stellar masses (or total stellar luminosity) of galaxies and their maximum rotational speed (or the total mass of the galaxy). This relationship is also frequently used as a distance estimator for galaxies, so the *Hubble Constant*, H_0 (Sakai et al. 1999; Tully & Pierce 2000; Russell 2009). Most TFR studies in the literature consider HI as a kinematic tracer to calculate the galaxy's maximum rotational velocity (e.g. Tully & Fisher 1977; Pizagno et al. 2007; Meyer et al. 2008; Williams, Bureau & Cappellari 2010; den Heijer et al. 2015). However, there are only a few studies in the literature that used CO as a kinematic tracer instead (Davis et al. 2011b; Tiley et al. 2016), including the first CO TFR study for galaxies outside the nearby universe (Topal et al. 2018).

There are some advantages of using CO for TFR studies instead of using HI. First and foremost, CO could be observed in galaxies at larger distances, particularly the galaxies with high SFR located at

$z = 1 - 7$ (or equivalently 7.8 and 12.9 billion years lookback time⁵, respectively) are now routinely observed in CO (Riechers et al. 2009; Tacconi et al. 2010; Wang et al. 2011; Genzel et al. 2015). Secondly, the angular resolution of CO will be much better for an observed galaxy compared to HI. Thirdly, CO is more centrally concentrated in galaxies, and therefore not affected by collisions or interactions with other galaxies as HI does (Lavezzi & Dickey 1998). Galaxies suitable for TFR studies should not have any collisions or interactions significantly affecting their rotational speed. Additionally, the tracer used to calculate the rotational velocity should minimally be affected by such galactic-scale collisions and/or interactions. CO is, therefore, a useful kinematic tracer and an alternative to HI to study TFR in galaxies throughout the cosmic sea.

5. THE RELATIONSHIP BETWEEN CO VELOCITY WIDTH AND BLACK HOLE MASS

Although supermassive black holes (SMBHs) at the heart of galaxies are extreme objects, only a few parameters can define them, such as mass, angular momentum and electric charge. The SMBHs occupy a relatively small area in the host galaxy ($r \leq 100 pc$), there is a correlation between some physical properties of the SMBH-host galaxies and the mass of the SMBH (M_{BH}). Examples of such physical properties that correlate with the M_{BH} are the velocity dispersion of stars, σ_* , ($M_{BH} - \sigma_*$ relationship; Ferrarese & Merritt 2000; Barai et

⁵ Ned Wright's Cosmology Calculator
<http://www.astro.ucla.edu/~wright/CosmoCalc.html>

al. 2014), the bulge mass of the galaxy (Kormendy & Richstone 1995), and the total luminosity of the galaxy (Lasker & van de Ven 2014). SMBHs can co-exist with AGN phenomena, and thus SMBH can have widespread effects on the galaxy. AGN structures show strong broad emission lines over a wide wavelength range, creating a large-scale influence on galaxy evolution (Kormendy & Ho 2013). Indeed, some studies show a close relationship between galaxy evolution and SMBH growth (Silk & Rees 1998).

According to some studies, there is also a similar relationship between CO line width, $\Delta_{CO} [km s^{-1}]$, and the M_{BH} . The *millimetre-Wave Interferometric Survey of Dark Object Masses* (WISDOM) project indicated that the M_{BH} could be estimated using high angular resolution CO data (Onishi et al. 2017; Davis et al. 2017). That provides an unprecedented opportunity to calculate the M_{BH} of galaxies located at larger distances in the universe like never before.

6. PROBING THE PHYSICS OF STAR-FORMING GAS CLOUDS USING MOLECULAR LINE RATIOS

Different emission characteristics allow us to study the different phases of the ISM (e.g. different kinetic temperatures, density and opacity), as each molecular emission occurs under a different physical conditions. The ratios between CO and its isotope ^{13}CO give information about the optical depth of the gas, so the column density (the higher the ratio, the thinner the CO gas), and also the mechanical feedback in the medium (i.e. the existence of strong stellar winds or

supernova explosions). The ratio often shows a radial gradient in galaxies (e.g. Paglione et al. 2001) and could have different values in galaxies with different SFRs (Henkel et al. 1994; Baan et al. 2008; Israel et al. 2009a,b). Additionally, although the line ratios could be different in galaxies with different SF histories, some studies indicate that the center of ETGs could have similar line ratios to that found in spiral galaxies (Crocker et al., 2012; Topal et al., 2016).

The CO line ratios of different transitions could also give information on the temperature and density (Lamperti et al. 2020). Other complex molecules, such as HCN, HCO^+ , HNC ve HNCO, give insights into the physics of dense gas clouds (Krips et al. 2008, 2010; Privon et al. 2015). The ratio of dense gas tracers to CO, such as the ratio of HCN/CO, provides us with information on the dense gas fraction, i.e. the lower the ratio, the higher the dense gas fraction vice versa (Gao & Solomon 2004; Brouillet et al. 2005; Topal et al. 2016). The HCN/CO ratio could also correlate with the hydrostatic pressure, i.e. as the ratio increases, the pressure also increases (Helfer & Blitz 1997).

Some molecular line ratios allow us to probe the existence of supernovae, so the CRs, in the medium. In general HCN is brighter than HCO^+ in galaxies, i.e. $\text{HCN}/\text{HCO}^+ > 1$. However, in regions where supernova explosions are happening, the ratio could be $\text{HCN}/\text{HCO}^+ < 1$ because of the increase in the CRs (Dickinson et al. 1980; Wootten 1981; Elitzur 1983; Joulain et al.1998; Costagliola et al. 2011). Additionally, the line ratios in the XDRs could also be different from the regions with much lower X-ray radiation.

Meijerink, Spaans & Israel (2007) argued that in XDRs with high gas density, i.e. $n(H_2) > 10^5 \text{ cm}^{-3}$, the ratio could become $\text{HCN}/\text{HCO}^+ > 1$, while in PDRs it could have values of $\text{HCN}/\text{HCO}^+ < 1$. These indicate that the dominant radiation field in the medium (CRs, X-rays or FUV) strongly affects the physics and chemical composition of the gas clouds, so the observed line ratios.

There are many radiative transfer codes in the literature, allowing us to study the physics of the ISM numerically. Examples of such codes are *UCL_PDR* (Papadopoulos, Thi & Viti 2002; Bell et al. 2005), *Meudon* (Le Petit et al. 2006) and *RADEX* (van der Tak et al. 2007). Röllig et al. (2007) compared many radiative transfer codes aiming to probe the physics and chemical compositions in PDRs. They found that although the change of resulting physical properties (produced using different codes with the same inputs) show a similar trend, absolute values show some differences, and the results strongly depend on the chemical composition of the medium.

CONCLUSIONS

Observations of molecular emission lines not only provide us with a invaluable information on SF but also the physics and kinematics of the gas, so the structure and evolution of galaxies located within a large range of z . With the power of molecular line ratio diagnostics, we are able to understand the effects of young massive stars and supernova explosion, and the true nature of PDRs, XDRs, and CRDRs better. Multi-wavelength data are particularly useful as each molecular

emission has a unique finger print helping us to track down the true physical properties of the ISM. Given the advantages of using CO as a kinematic tracer, we are now in the era of studying galaxies at the high- z universe, the time when the universe was a toddler, by the power of telescopes such as the Atacama Large Millimeter Array. Our understanding of the universe is improving dramatically by today's more advanced observational and analysis methods and state-of-art telescopes, with a promise for more yet to come.

REFERENCES

- Achterberg A., Gallant Y. A., Kirk J. G., Guthmann A. W., (2001), Particle acceleration by ultrarelativistic shocks: theory and simulations, *Monthly Notices of the Royal Astronomical Society*, Vol. 328 (2), pp 393-408.
- Abdo, A. A., Ackermann, M., Ajello, M., Baldini, L., Ballet, J., Barbiellini, G., Bastieri, D., Baughman, B. M., Bechtol, K., Bellazzini, R. et al., (2010), Fermi Observations of Cassiopeia and Cepheus: Diffuse Gamma-ray Emission in the Outer Galaxy, *The Astrophysical Journal*, Vol. 710 (1), pp 133-149..
- Baan W. A., Henkel C., Loenen A. F., Baudry A., Wiklind T., (2008), Dense gas in luminous infrared galaxies, *Astronomy and Astrophysics*, Vol. 477 (3), pp 747-762.
- Barai, P., Viel, M., Murante, G., Gaspari, M., Borgani, S., (2014), Kinetic or thermal AGN feedback in simulations of isolated and merging disc galaxies calibrated by the M- σ relation, *Monthly Notices of the Royal Astronomical Society*, Vol. 437 (2), pp 1456-1475.
- Bayet E., Gerin M., Phillips T. G., Contursi A., (2004), The submillimeter C and CO lines in Henize 2-10 and NGC 253, *Astronomy and Astrophysics*, Vol. 427, pp 45-59.
- Bayet E., Gerin M., Phillips T. G., Contursi A., (2006), A survey of submillimeter C and CO lines in nearby galaxies, *Astronomy and Astrophysics*, Vol. 460 (2), pp 467-485.
- Bell T. A., Viti S., Williams D. A., Crawford I. A., Price R. J., (2005), The chemistry of transient microstructure in the diffuse interstellar medium, *Monthly Notices of the Royal Astronomical Society*, Vol. 357 (3), pp 961-966.
- Bialy, S., Sternberg. A., (2015), CO/H₂, C/CO, OH/CO, and OH/O₂ in dense interstellar gas: from high ionization to low metallicity, *Monthly Notices of the Royal Astronomical Society*, Vol. 450, pp 4424-4445.
- Bigiel, F., Leroy, A., Walter, F., Brinks, E., de Blok, W. J. G., Madore, B., &

- Thornley, M. D., (2008), The Star Formation Law in Nearby Galaxies on Sub-Kpc Scales, *The Astronomical Journal*, Vol. 136 (6), pp 2846-2871.
- Boesgaard, A. M.; Steigman, G., (1985), Big Bang nucleosynthesis: theories and observations, *Annual Review of Astronomy and Astrophysics*, Vol. 23, pp 319-378,
- Bolatto A. D., Leroy A. K., Rosolowsky E., Walter F., Blitz L., (2008), The Resolved Properties of Extragalactic Giant Molecular Clouds, *The Astrophysical Journal*, Vol. 686 (2), pp 948-965.
- Bolatto A. D., Wolfire M., Leroy A. K., (2013), The CO-to-H₂ Conversion Factor, *Annual Review of Astronomy and Astrophysics*, Vol. 51 (1), pp 207-268.
- Brouillet N., Muller S., Herpin F., Braine J., Jacq T., (2005), HCN and HCO⁺ emission in the disk of M 31, *Astronomy and Astrophysics*, Vol. 429, pp 153-159.
- Calzetti, D., Kennicutt, R. C. Jr., Bianchi, L., Thilker, D. A., Dale, D. A., Engelbracht, C. W., Leitherer, C., Meyer, M. J., Sosey, M. L., Mutchler, M. et al., (2005), Star Formation in NGC 5194 (M51a): The Panchromatic View from GALEX to Spitzer, *The Astrophysical Journal*, Vol. 633, pp 871-893.
- Cappellari, M., Emsellem, E., Krajnović, D., McDermid, R. M., Scott, N., Verdoes K. G. A., Young, L. M., Alatalo, K., Bacon, R., Blitz, L. et al., (2011), The ATLAS3D project - I. A volume-limited sample of 260 nearby early-type galaxies: science goals and selection criteria, *Monthly Notices of the Royal Astronomical Society*, Vol. 413 (2), pp 813-836.
- Carruthers, George R. (1970), Rocket Observation of Interstellar Molecular Hydrogen, *The Astrophysical Journal*, Vol. 161, pp L81-L85.
- Cazaux, S. and A. Tielens, (2002), Molecular hydrogen formation in the interstellar medium. *The Astrophysical Journal*, Vol. 575 (1): pp L29-L32.
- Cazaux, S. and A. Tielens, (2004), Formation on grain surfaces. *The Astrophysical Journal*, 604 (1), pp 222-237.
- Cheung A. C., Rank D. M., Townes C. H., Thornton D. D., Welch W. J., (1968), Detection of NH₃ Molecules in the Interstellar Medium by Their

- Microwave Emission, *Physical Review Letters*, Vol. 21 (25), pp 1701-1705.
- Costagliola, F., Aalto, S., Rodriguez, M. I., Muller, S., Spoon, H. W. W., Martín, S., Pérez-Torres, M. A., Alberdi, A., Lindberg, J. E., Batejat, F., et al., (2011), Molecules as tracers of galaxy evolution: an EMIR survey. I. Presentation of the data and first results, *Astronomy and Astrophysics*, Vol. 528, pp 30-57.
- Crocker, A., Krips, M., Bureau, M., Young, L. M., Davis, T. A., Bayet, E., Alatalo, K., Blitz, L., Bois, M., Bournaud, F. et al., (2012), The ATLAS3D project - XI. Dense molecular gas properties of CO-luminous early-type galaxies, *Monthly Notices of the Royal Astronomical Society*, Vol. 421 (2), pp 1298-1314.
- Cyburt, Richard H., Fields, Brian D., Olive, Keith A., Yeh, Tsung-Han, (2016), Big bang nucleosynthesis: Present status, *Reviews of Modern Physics*, Vol. 88 (1), id.015004
- Dale, D. A., Gil de Paz, A., Gordon, K. D., Hanson, H. M., Armus, L., Bendo, G. J., Bianchi, L., Block, M., Boissier, S., Boselli, A. et al., (2007), An Ultraviolet-to-Radio Broadband Spectral Atlas of Nearby Galaxies, *The Astrophysical Journal*, Vol. 655, pp 863-884.
- Dame T. M., Hartmann D., Thaddeus P., (2001), The Milky Way in Molecular Clouds: A New Complete CO Survey, *The Astrophysical Journal*, Vol. 547 (2), pp 792-813.
- Davis, T. A., Alatalo, K., Sarzi, M., Bureau, M., Young, L. M., Blitz, L., Serra, P., Crocker, A. F., Krajinovic, D., McDermid, R. M. et al., (2011a), The ATLAS3D project – X. On the origin of the molecular and ionized gas in early-type galaxies, *Monthly Notices of the Royal Astronomical Society*. Vol. 417, pp 882–899.
- Davis, T. A., Bureau, M., Young, L. M., Alatalo, K., Blitz, L., Cappellari, M., Scott, N., Bois, M., Bournaud, F., Davies, R. L. et al., (2011b), The ATLAS3D project - V. The CO Tully-Fisher relation of early-type galaxies, *Monthly Notices of the Royal Astronomical Society*, Vol. 414 (2), pp 968-984.

- Davis T. A., Bureau M., Onishi K., Cappellari M., Iguchi S., Sarzi M., (2017), WISDOM Project – II. Molecular gas measurement of the supermassive black hole mass in NGC 4697, *Monthly Notices of the Royal Astronomical Society*, Vol. 468, pp 4675–4690.
- de Vaucouleurs G., de Vaucouleurs A., Corwin, Jr. H. G., Buta R. J., Paturel G., Fouqu_e P., (1991), *Third Reference Catalogue of Bright Galaxies*. Volume I: Explanations and references. Volume II: Data for galaxies between 0h and 12h. Volume III: Data for galaxies between 12h and 24h.
- den Heijer, M., Oosterloo, T. A., Serra, P., Józsa, G. I. G., Kerp, J., Morganti, R., Cappellari, M., Davis, T. A., Duc, P., Emsellem, E. et al., (2015), The HI Tully-Fisher relation of early-type galaxies, *Astronomy & Astrophysics*, Vol. 581, pp 98-108.
- Dickinson D. F., Rodriguez Kuiper E. N., Dinger A. S. C., Kuiper T. B. H., (1980), Shock enhancement of HCO+, *The Astrophysical Journal Letters*, Vol. 237, pp L43-L45
- Donovan M., J., Koda, J., Momose, R., Fukuhara, M., Mooney, T., Towers, S., Egusa, F., Kennicutt, R., Kuno, N., Carty, M., et al., (2012), Resolved Measurements of X_CO in NGC 6946, *The Astrophysical Journal*, Vol. 744 (1), pp 42-52.
- Douglas, A. E., ve Herzberg, G. H., (1941), Note on CH+ in Interstellar Space and in the Laboratory, *The Astrophysical Journal*. Vol. 94, pp 381.
- Downes, D. ve Solomon, P.M., (1998), Rotating Nuclear Rings and Extreme Starbursts in Ultraluminous Galaxies, *The Astrophysical Journal*, Vol. 507 (2), pp 615-654.
- Duley, W. W., (1996), The formation of H₂ by H-atom reaction with grain surfaces, *Monthly Notices of the Royal Astronomical Society*, Vol. 279 (2), pp 591-594.
- Dunham T., (1937), *Interstellar Neutral Potassium and Neutral Calcium*, *Publications of the Astronomical Society of the Pacific*, Vol. 49, pp 26-28.
- Eliche-Moral, M. C., Prieto, M.; Gallego, J., Barro, G.; Zamorano, J., López-Sanjuan, C.; Balcells, M.; Guzmán, R.; Muñoz-Mateos, J. C., (2010), On

- the buildup of massive early-type galaxies at $z \leq 1$. I. Reconciling their hierarchical assembly with mass downsizing, *Astronomy and Astrophysics*, Vol. 519, pp 55-74.
- Elitzur M., (1983), Shock formation of HCO⁺, *The Astrophysical Journal*, Vol. 267, pp 174-178.
- Ferrarese, L., ve Merritt, D., (2000), A Fundamental Relation Between Supermassive Black Holes and Their Host Galaxies, *The Astrophysical Journal Letters*, Vol. 539, pp L9-L12
- Ferrari A., (1998), Modeling Extragalactic Jets, *Annual Review of Astronomy and Astrophysics*, Vol. 36, pp 539-598.
- Fixsen D. J., Bennett C. L., Mather J. C., (1999), COBE Far Infrared Absolute Spectrophotometer Observations of Galactic Lines, *The Astrophysical Journal*, Vol. 526 (1), pp 207-214.
- Friedmann, A., Über die Möglichkeit einer Welt mit konstanter negativer Krümmung des Raumes, *Zeit. Phys.* 21, 326 (1924). English translation in J. Bernstein et G. Feinberg (éds.), *Cosmological Constants. Papers in Modern Cosmology*, New York, Columbia University Press, 1986, p. 59-65.
- Gao Y., Solomon P. M., (2004), The Star Formation Rate and Dense Molecular Gas in Galaxies, *The Astrophysical Journal*, Vol. 606 (1), pp 271-290.
- Gardan, E., Braine, J., Schuster, K. F., Brouillet, N., & Sievers, A. (2007), Particularly efficient star formation in M 33, *Astronomy and Astrophysics*, Vol. 473 (1), pp 91-104.
- Genzel, R., Tacconi, L. J., Lutz, D., Saintonge, A., Berta, S., Magnelli, B., Combes, F., García-Burillo, S., Neri, R., Bolatto, A. et al., (2015), Combined CO and Dust Scaling Relations of Depletion Time and Molecular Gas Fractions with Cosmic Time, Specific Star-formation Rate, and Stellar Mass, *The Astrophysical Journal*, Vol. 800 (1), pp 20-44.
- Girichidis, P., Offner, S. S. R., Kritsuk, A. G., Klessen, R. S., Hennebelle, P., Kruijssen, J. M. D., Krause, M. G. H., Glover, S. C. O., Padovani, M., (2020), Physical Processes in Star Formation, *Space Science Reviews* Vol.

216 (4), pp 68-151.

- Goldsmith, P. F., Heyer, M., Narayanan, G., Snell, R., Li, D., Brunt, C., (2008), Large-Scale Structure of the Molecular Gas in Taurus Revealed by High Linear Dynamic Range Spectral Line Mapping, *The Astrophysical Journal*, Vol. 680 (1), pp 428-445.
- Gould, R. J., Salpeter, E. E., (1963), The Interstellar Abundance of the Hydrogen Molecule. I. Basic Processes, *The Astrophysical Journal*, Vol. 138, pp 393-407.
- Gratier, P. J., Braine, K., Schuster, E., Rosolowsky, M., Boquien, D., Calzetti, F., Combes, C., Kramer, C., Henkel, F., Herpin, F., et al., (2017), The molecular gas mass of M33, *Astronomy and Astrophysics*, Vol. 600, pp A27-A40.
- Guo F., Mathews W. G., (2011), Cosmic-ray-dominated AGN Jets and the Formation of X-ray Cavities in Galaxy Clusters, *The Astrophysical Journal*, Vol. 728 (2), pp 121-129.
- Habart, E., Dartois, E., Abergel, A., Baluteau, J. P., Naylor, D., Polehampton, E., Joblin, C., Ade, P., Anderson, L. D., André, P. et al., (2010), SPIRE spectroscopy of the prototypical Orion Bar photodissociation region, *Astronomy and Astrophysics*, Vol. 518, pp 116-120.
- Heiderman, A., Evans, N. J., II, Allen, L. E., Huard, T., Heyer, M., (2010), The Star Formation Rate and Gas Surface Density Relation in the Milky Way: Implications for Extragalactic Studies, *The Astrophysical Journal*, Vol. 723 (2), pp 1019-1037.
- Helfer, T. T., Thornley, M. D., Regan, M. W., Wong, T., Sheth, K., Vogel, S. N., Blitz, L., Bock, D. C. J., (2003), The BIMA Survey of Nearby Galaxies (BIMA SONG). II. The CO Data, *The Astrophysical Journal Supplement Series*, Vol. 145 (2), pp 259-327.
- Helfer T. T., Blitz L., (1997), Dense Gas in the Milky Way, *The Astrophysical Journal*, Vol. 478 (1), pp 233-245.
- Henkel C., Whiteoak J. B., Mauersberger R., (1994), Dense gas in nearby galaxies. VII. The active nucleus of NGC 4945, *Astronomy and Astrophysics*, Vol.

284, pp 17-27.

- Hirata, C. M., Padmanabhan, N., (2006), Cosmological production of H₂ before the formation of the first galaxies, *Monthly Notices of the Royal Astronomical Society*, Vol. 372, pp 1175–1186.
- Hollenbach D., & Salpeter E. E., (1971), Surface Recombination of Hydrogen Molecules, *The Astrophysical Journal*, Vol. 163, pp 155-164.
- Hollenbach, D., Werner M. W. ve Salpeter, E. E., (1971), Molecular Hydrogen in HI Regions, *The Astrophysical Journal*. Vol. 163, 165-180.
- Hollenbach D. J., ve Tielens A. G. G. M., (1999), Photodissociation regions in the interstellar medium of galaxies, *Reviews of Modern Physics.*, Vol. 71 (1), pp 173-230.
- Hubble, E., A Relation between Distance and Radial Velocity among Extra-Galactic Nebulae, (1929), *Proceedings of the National Academi of Science*, Vol. 15 (3), pp 168-173.
- Hubble, E.P., (1936), *Realm of the Nebulae*, by E.P. Hubble. New Haven: Yale University Press, 1936. ISBN 9780300025002
- Hunt, L. K., García-Burillo, S., Casasola, V., Caselli, P., Combes, F., Henkel, C., Lundgren, A., Maiolino, R., Menten, K. M., Testi, L., Weiss, A., (2015), Molecular depletion times and the CO-to-H₂ conversion factor in metal-poor galaxies, *Astronomy and Astrophysics*, Vol. 583, pp A114-A130.
- Indriolo, N., McCall, B. J., (2012), Investigating the Cosmic-Ray Ionization Rate in the Galactic Diffuse Interstellar Medium through Observations of H⁺₃, *The Astrophysical Journal*, Vol. 745 (1), pp 91-107.
- Israel F. P., (2009a), CI and CO in nearby galaxy centers. The bright galaxies NGC 1068 (M 77), NGC 2146, NGC 3079, NGC 4826 (M 64), and NGC 7469, *Astronomy and Astrophysics*, Vol. 493 (2), pp 525-538.
- Israel F. P., (2009b), CI and CO in nearby galaxy centers. The star-burst galaxies NGC 278, NGC 660, NGC 3628 NGC 4631, and NGC 4666, *Astronomy and Astrophysics*, Vol. 506 (2), pp 689-702.
- Jimenez-Donaire, M. J., F. Bigiel, F., Leroy, A. K., Usero, A., Cormier, D., Puschign, J., Gallagher, M., Kepley, A., Bolatto, A. D., Garc,a-Burillo, S. et

- al., (2019), EMPIRE: The Iram 30m Dense Gas Survey Of Nearby Galaxies, *The Astrophysical Journal*, Vol. 880 (2), pp 127-181.
- Joulain K., Falgarone E., Pineau des Forets G., Flower D., (1998), Non-equilibrium chemistry in the dissipative structures of interstellar turbulence, *Astronomy and Astrophysics*, Vol. 340, pp 241-256.
- Kennicutt, R. C., Jr. (1998), The Global Schmidt Law in Star-forming Galaxies, *The Astrophysical Journal*, Vol. 498 (2), pp 541-552.
- Kennicutt, R. C., Calzetti, D., Walter, F., Helou, G., Hollenbach, D. J., Armus, L., Bendo, G., Dale, D. A., Draine, B. T., Engelbracht, C. W., Gordon, K. D. et al., (2007), Star Formation in NGC 5194 (M51a). II. The Spatially Resolved Star Formation Law, *The Astrophysical Journal*, Vol. 671 (1), pp 333-348.
- Klessen R.S., Glover S.C.O., (2016), Physical Processes in the Interstellar Medium. In: Revaz Y., Jablonka P., Teyssier R., Mayer L. (eds) *Star Formation in Galaxy Evolution: Connecting Numerical Models to Reality*. Saas-Fee Advanced Course, vol 43. Springer, Berlin, Heidelberg. https://doi.org/10.1007/978-3-662-47890-5_2
- Kim J.-G., Kim W.-T., Ostriker E. C., (2018), Modeling UV Radiation Feedback from Massive Stars. II. Dispersal of Star-forming Giant Molecular Clouds by Photoionization and Radiation Pressure, *The Astrophysical Journal*, Vol. 859 (1), pp 68-91.
- Kormendy J., Richstone D., (1995), Inward Bound---The Search For Supermassive Black Holes In Galactic Nuclei, *Annual Review of Astronomy and Astrophysics*, Vol. 33, pp 581
- Kormendy J., Bender R., (2012), A Revised Parallel-sequence Morphological Classification of Galaxies: Structure and Formation of S0 and Spheroidal Galaxies, *The Astrophysical Journal Supplement Series*, Vol. 198 (1), pp 2-41.
- Kormendy & Ho, (2013), Coevolution (Or Not) of Supermassive Black Holes and Host Galaxies, *Annual Review of Astronomy and Astrophysics*, Vol. 51, pp 511-653.

- Krips M., Neri R., Garcia-Burillo S., Martin S., Combes F., Gracia-Carpio J., Eckart A., (2008), A Multi-Transition HCN and HCO⁺ Study of 12 Nearby Active Galaxies: Active Galactic Nucleus versus Starburst Environments, *The Astrophysical Journal*, Vol. 677 (1), pp 262-275.
- Krips M., Crocker A. F., Bureau M., Combes F., Young L. M., (2010), Molecular gas in SAURON early-type galaxies: detection of ¹³CO and HCN emission, *Monthly Notices of the Royal Astronomical Society*, Vol. 407 (4), pp 2261-2268.
- Krumholz, M. R., McKee, C. F., Tumlinson, J., (2009), The Atomic-to-Molecular Transition in Galaxies. II: HI and H₂ Column Densities, *The Astrophysical Journal*, Vol. 69 (1)3, pp 216-235.
- Krumholz, Mark R., (2011), Star Formation in Molecular Clouds, Xv Special Courses at The National Observatory Of Rio De Janeiro. AIP Conference Proceedings, 1386, 9-57.
- Krumholz, M. R., Dekel, A., ve McKee, C. F., (2012), A Universal, Local Star Formation Law in Galactic Clouds, nearby Galaxies, High-redshift Disks, and Starbursts, *The Astrophysical Journal*, Vol. 745 (1), pp 69-84.
- Kuno, N., Sato, N., Nakanishi, H., Hirota, A., Tosaki, T., Shioya, Y., Sorai, K., Nakai, N., Nishiyama, K., Vila-Vilaró, B., (2007), Nobeyama CO Atlas of Nearby Spiral Galaxies: Distribution of Molecular Gas in Barred and Nonbarred Spiral Galaxies, *Publications of the Astronomical Society of Japan* Vol. 59 (1), pp 117-166.
- Lamperti, I., Saintonge, A., Koss, M., Viti, S., Wilson, C. D., He, H., Shimizu, T. T., Greve, T. R., Mushotzky, R., Treister, E. et al., (2020), The CO(3-2)/CO(1-0) Luminosity Line Ratio in Nearby Star-forming Galaxies and Active Galactic Nuclei from xCOLD GASS, BASS, and SLUGS, *The Astrophysical Journal*, Vol. 889 (2), pp 103-130.
- Lasker R., Ferrarese L., van de Ven G., (2014), Supermassive Black Holes and Their Host Galaxies. I. Bulge Luminosities from Dedicated Near-infrared Data, *The Astrophysical Journal*, Vol. 780 (1), pp 69-109.
- Lavezzi T. E., Dickey J. M., (1998), *The Astronomical Journal*, Vol. 116, pp 2672-

2681.

- Le Petit, Franck, Nehmé, C., Le Bourlot, J., Roueff, E., (2006), A Model for Atomic and Molecular Interstellar Gas: The Meudon PDR Code, The Astrophysical Journal Supplement Series, Vol. 164 (2), pp 506-529.
- Lee H., Bettens R. P. A., Herbst E., (1996), Fractional abundances of molecules in dense interstellar clouds: A compendium of recent model results, Astronomy and Astrophysics Supplement Series, Vol. 119, 111-114.
- Lemaître, G., Un univers homogène de masse constante et de rayon croissant, rendant compte de la vitesse radiale des nébuleuses extra-galactiques, Ann. Soc. Sci. Bruxelles, série A 47, 49 (1927). New English translation and Editorial Note in J.-P. Luminet, General Relativity and Gravitation Vol. 45, 1619 (2013).
- Lepp, S., Stancil, P. C., ve Dalgarno, A., (2002), TOPICAL REVIEW: Atomic and molecular processes in the early Universe, Journal of Physics B, Vol. 35 (10), pp R57-R80.
- Leroy, A. K., Walter, F., Bigiel, F., Usero, A., Weiss, A., Brinks, E., de Blok, W. J. G., Kennicutt, R. C., Schuster, K., Kramer, C. et al., (2009), Heracles: The HERA CO Line Extragalactic Survey, The Astronomical Journal, Vol. 137 (6), pp 4670-4696.
- Liszt, H. S., Pety, J., ve Lucas, R. (2010), The CO luminosity and CO-H₂ conversion factor of diffuse ISM: does CO emission trace dense molecular gas?, Astronomy and Astrophysics, Vol. 518, pp A45-A54.
- Maloney P. R., Hollenbach D. J., Tielens A. G. G. M., (1996), X-Ray--irradiated Molecular Gas. I. Physical Processes and General Results, The Astrophysical Journal, Vol. 466, pp 561.
- Mao, R., Schulz, A., Henkel, C., Mauersberger, R., Muders, D., Dinh-V-Trung, (2010), An Extragalactic 12CO J = 3–2 Survey with The Heinrich Hertz Telescope, The Astrophysical Journal, Vol. 724 (2), pp 1336-1356.
- Mazzuca, L. M., Sarzi, M., Knapen, J. H., Veilleux, S., Swaters, R., (2006), Minor Merger Origin for the Circumnuclear Starburst in NGC 7742, The Astrophysical Journal, Vol. 649 (2), pp L79-L82.

- McKee, C. F., Ostriker, E. C., (2007), Theory of Star Formation, *Annual Review of Astronomy and Astrophysics*, Vol. 45, pp 565-687.
- McKellar A. (1940). *Publications of the Astronomical Society of the Pacific*, Vol. 52, pp 187-192.
- Medina S.-N. X., Arthur S. J., Henney W. J., Mellema G., Gazol A., (2014), Turbulence in simulated HII regions, *Monthly Notices of the Royal Astronomical Society*, Vol. 445 (2), pp 1797-1819.
- Meidt, S. E.; Schinnerer, E., Knapen, J. H., Bosma, A., Athanassoula, E., Sheth, K., Buta, R. J., Zaritsky, D., Laurikainen, E., Elmegreen, D. et al., (2012), Reconstructing the Stellar Mass Distributions of Galaxies Using S4G IRAC 3.6 and 4.5 μm Images. I. Correcting for Contamination by Polycyclic Aromatic Hydrocarbons, Hot Dust, and Intermediate-age Stars, *The Astrophysical Journal*, Vol. 744 (1), pp 17-33.
- Meidt, Sharon E.; Schinnerer, Eva; van de Ven, Glenn; Zaritsky, Dennis; Peletier, Reynier; Knapen, Johan H.; Sheth, Kartik; Regan, Michael; Querejeta, Miguel; Muñoz-Mateos, Juan-Carlos, (2014), Reconstructing the Stellar Mass Distributions of Galaxies Using S4G IRAC 3.6 and 4.5 μm Images. II. The Conversion from Light to Mass, *The Astrophysical Journal*, Vol. 788 (2), pp 144-155.
- Meijerink R., Spaans M., Israel F. P., (2007), Diagnostics of irradiated dense gas in galaxy nuclei. II. A grid of XDR and PDR models, *Astronomy and Astrophysics*, Vol. 461 (3), pp 793-811.
- Meyer, M. J., Zwaan, M. A., Webster, R. L., Schneider, S., Staveley-Smith, L., (2008), Tully–Fisher relations from an HI-selected sample, *Monthly Notices of the Royal Astronomical Society*, Vol. 391 (4), pp 1712–1728.
- Narayanan, D.; Krumholz, M.; Ostriker, E.C.; Hernquist, L., (2011), The CO-H₂ conversion factor in disc galaxies and mergers, *Monthly Notices of the Royal Astronomical Society*, Vol. 418 (1), pp 664-679.
- Narayanan, D., Krumholz, M., Ostriker, E. C., Hernquist, L., (2012), A general model for the CO–H₂ conversion factor in galaxies with applications to the

- star formation law, *Monthly Notices of the Royal Astronomical Society*, Vol. 421, pp 3127–3146.
- Onishi K., Iguchi, S., Davis T. A., Bureau M., Cappellari M., Sarzi M., and Blitz L., (2017), WISDOM project – I. Black hole mass measurement using molecular gas kinematics in NGC 3665, *Monthly Notices of the Royal Astronomical Society*, Vol. 468, pp 4663-4674.
- Padovani, M., Galli, D., Glassgold, A. E., (2009), Cosmic-ray ionization of molecular clouds, *Astronomy and Astrophysics*, Vol. 501 (2), pp 619-631.
- Pahre, Michael A., Ashby, M. L. N., Fazio, G. G., Willner, S. P., (2004), Mid-Infrared Galaxy Morphology along the Hubble Sequence, *Astrophysical Journal Supplement Series*, Vol. 154, pp 235-241.
- Paglione, T. A. D., Wall, W. F., Young, J. S., Heyer, M. H., Richard, M., Goldstein, M., Kaufman, Z., Nantais, J., Perry, G., (2001), A Mapping Survey of the 13CO and 12CO Emission in Galaxies, *The Astrophysical Journal Supplement Series*, Vol. 135 (2), pp 183-200.
- Papadopoulos P. P., Thi W.-F., Viti S., (2002), Molecular Gas in Spiral Galaxies: A New Warm Phase at Large Galactocentric Distances?, *The Astrophysical Journal*, Vol. 579 (1), pp 270-274.
- Peletier, R. F., Kutdemir, E., van der Wolk, G., Falcón-Barroso, J., Bacon, R., Bureau, M., Cappellari, M., Davies, R. L., de Zeeuw, P. T., Emsellem, E., (2012), The SAURON project - XX. The Spitzer [3.6] - [4.5] colour in early-type galaxies: colours, colour gradients and inverted scaling relations, *Monthly Notices of the Royal Astronomical Society*. Vol. 419 (3), pp 2031-2053.
- Penzias A. A., Jefferts K. B., Wilson R. W., (1971), Interstellar 12C16O, 13C16O, and 12C18O, *The Astrophysical Journal*, Vol. 165, pp 229.
- Perets, H. B., Ofer, B., (2006), Molecular hydrogen formation on porous dust grains, *Monthly Notices of the Royal Astronomical Society*, Vol. 365 (3), pp 801-806.
- Pizagno, J., Prada, F., Weinberg, D. H., Rix, H., Pogge, R. W., Grebel, E. K., Harbeck, D., Blanton, M., Brinkmann, J., Gunn, J. E., (2007), The Tully-

- Fisher Relation and its Residuals for a Broadly Selected Sample of Galaxies, *The Astronomical Journal*, Vol. 134 (3), pp 945-972.
- Privon, G. C., Herrero-Illana, R., Evans, A. S., Iwasawa, K., Perez-Torres, M. A., Armus, L., Díaz-Santos, T., Murphy, E. J., Stierwalt, S., Aalto, S. et al., (2015), Excitation Mechanisms for HCN (1-0) and HCO⁺ (1-0) in Galaxies from the Great Observatories All-sky LIRG Survey, *The Astrophysical Journal*, Vol. 814 (1), pp 39-53.
- Querejeta, M., Meidt, S. E., Schinnerer, E., Cisternas, M., Muñoz-Mateos, J. C., Sheth, K., Knapen, J., van de Ven, G., Norris, M. A., Reynier, P., (2015), The Spitzer Survey of Stellar Structure in Galaxies (S4G): Precise Stellar Mass Distributions from Automated Dust Correction at 3.6 μm , *Astrophysical Journal Supplement Series*, Vol. 219, pp 5-23.
- Riechers, D. A., Walter, F., Bertoldi, F., Carilli, C. L., Aravena, M., Neri, R., Cox, P., Weiß, A., Menten, K. M., (2009), Imaging Atomic and Highly Excited Molecular Gas in a $z = 6.42$ Quasar Host Galaxy: Copious Fuel for an Eddington-limited Starburst at the End of Cosmic Reionization, *The Astrophysical Journal*, Vol. 703 (2), pp 1338-1345.
- Rosolowsky E., Engargiola G., Plambeck R., Blitz L., (2003), Giant Molecular Clouds in M33. II. High-Resolution Observations, *The Astrophysical Journal*, Vol. 599 (1), pp 258-274.
- Roman-Duval, J., Heyer, M., M. Brunt, C., Clark, P., Klessen, R., Shetty, R., (2016), Distribution and Mass of Diffuse and Dense Co Gas In The Milky Way, *The Astrophysical Journal*, Vol. 818 (2), pp 144-162.
- Röllig, M., Abel, N. P., Bell, T., Bensch, F., Black, J., Ferland, G. J., Jonkheid, B., Kamp, I., Kaufman, M. J., Le Bourlot, J. et al., (2007), A photon dominated region code comparison study, *Astronomy and Astrophysics*, Vol. 467, pp 187–206.
- Russell D. G., (2009), The Ks-band Tully–Fisher Relation – A Determination of the Hubble Parameter from 218 ScI Galaxies and 16 Galaxy Clusters, *Journal of Astrophysics and Astronomy*, Vol. 30, pp 93-118.

- Sandstrom, K. M., Leroy, A. K., Walter, F., Bolatto, A. D., Croxall, K. V., Draine, B. T., Wilson, C. D., Wolfire, M., Calzetti, D., Kennicutt, R. C. et al., (2013), The CO-to-H₂ Conversion Factor and Dust-to-gas Ratio on Kiloparsec Scales in Nearby Galaxies, *The Astrophysical Journal*, Vol. 777 (1), pp 5-37.
- Schmidt, M. (1959), The Rate of Star Formation, *The Astrophysical Journal*, Vol. 129, pp 243.
- Schruba, A., Leroy, A. K., Walter, F., Bigiel, F., Brinks, E., de Blok, W. J. G., Dumas, G., Kramer, C., Rosolowsky, E., Sandstrom, K. et al., (2011), A Molecular Star Formation Law in the Atomic-gas-dominated Regime in Nearby Galaxies, *The Astronomical Journal*, Vol. 142 (2), pp 37-61.
- Schinnerer, E., Meidt, S. E., Pety, J., Hughes, A., Colombo, D., García-Burillo, S., Schuster, K. F., Dumas, G., Dobbs, C. L., Leroy, A. K. et al., (2013), The PdBI Arcsecond Whirlpool Survey (PAWS). I. A Cloud-scale/Multi-wavelength View of the Interstellar Medium in a Grand-design Spiral Galaxy, *The Astrophysical Journal*, Vol. 779 (1), pp 42-70.
- Shapley H., Curtis H.D., (1921), The Scale of The Universe, *Bulletin of The National Research Council*, Vol. 2, Part 3, Number 11, pp. 171-217.
- Sakai, S., Mould, J. R., Hughes, S. M. G., Huchra, J. P., Macri, L. M., Kennicutt, R. C., Gibson, B. K., Ferrarese, J., Freedman, W. L., Han, M. et al., (2000), The Hubble Space Telescope Key Project on The Extragalactic Distance Scale. XXIV. The Calibration of Tully-Fisher Relations and The Value Of The Hubble Constant, *The Astrophysical Journal*, Vol. 529 (2), pp 698-722.
- Silk, J., Rees, M. J., (1998), Quasars and Galaxy Formation, *Astronomy and Astrophysics*, Vol. 331, pp 1-4.
- Solomon P., Jefferts K. B., Penzias A. A., Wilson R.W., (1971), Observation of CO Emission at 2.6 Millimeters from IRC+10216, *The Astrophysical Journal*, Vol. 163, pp L53.
- Sorai, K., Kuno, N., Muraoka, K., Miyamoto, Y., Kaneko, H., Nakanishi, H., Nakai, N., Yanagitani, K., Tanaka, T., Sato, Y. et al. (2019), CO multi-line imaging of nearby galaxies (COMING). IV. Overview of the project,

- Publications of the Astronomical Society of Japan, Vol. 71 (1), pp S14-S60.
- Stacey, G. J., Geis, N., Genzel, R., Lugten, J. B., Poglitsch, A., Sternberg, A., Townes, C. H., (1991), The 158 Micron [C ii] Line: A Measure of Global Star Formation Activity in Galaxies, *The Astrophysical Journal*, Vol. 373, pp 423-444.
- Swings P., Rosenfeld L., (1937), Considerations Regarding Interstellar Molecules, *The Astrophysical Journal*, Vol. 86, pp 483-486.
- Tacconi, L. J., Genzel, R., Neri, R., Cox, P., Cooper, M. C., Shapiro, K., Bolatto, A., Bouché, N., Bournaud, F., Burkert, A. et al., (2010), High molecular gas fractions in normal massive star-forming galaxies in the young Universe, *Nature*, Vol. 463 (7282), pp 781-784.
- Tiley, A. L., Bureau, M., Saintonge, A., Topal, S., Davis, T. A., Torii, K., (2016), The Tully–Fisher relation of COLD GASS Galaxies, *Monthly Notices of the Royal Astronomical Society*, Vol. 461, pp 3494-3515.
- Topal, S., Bayet, E., Bureau, M., Davis, T. A., Walsh, W., (2014), Molecular gas properties of the giant molecular cloud complexes in the arms and inter-arms of the spiral galaxy NGC 6946, *Monthly Notices of the Royal Astronomical Society*, Vol. 437, pp 1434-1455.
- Topal, S., Bureau M., Davis, T. A., Krips, M., Young, L. M., Crocker, A. F., (2016), Molecular gas kinematics and line diagnostics in early-type galaxies: NGC 4710 and NGC 5866, *Monthly Notices of the Royal Astronomical Society*, Vol. 463, pp 4121-4152.
- Topal, S., Bureau M., Tiley, A.L., Davis, T. A., Torii, K., (2018), CO Tully–Fisher relation of star-forming galaxies at $z = 0.05$ – 0.3 , *Monthly Notices of the Royal Astronomical Society*, Vol. 479, pp 3319-3334.
- Topal, S., (2020), Molecular line ratio diagnostics along the radial cut and dusty ultraviolet-bright clumps in a spiral galaxy NGC 0628, *Monthly Notices of the Royal Astronomical Society*, Vol. 495, pp 2682-2712.
- Topal S., (2021), Molecular line ratio diagnostics and gas kinematics in the AGN host Seyfert galaxy NGC 5033, *Monthly Notices of the Royal Astronomical Society*, Vol. 504, pp 5941-5953.

- Trimble, V., (1995), The 1920 Shapley-Curtis Discussion: Background, Issues, and Aftermath, Publications of the Astronomical Society of the Pacific, Vol. 107, pp 1133-1144.
- Tully R. B., Fisher J. R., (1977), A new method of determining distance to galaxies, Astronomy and Astrophysics, Vol. 54, pp 661T, reprint Vol. 500, pp 105-117 (2009).
- Tully, R. B. and Pierce, M. J., (2000), Distances to Galaxies from the Correlation between Luminosities and Line Widths. III. Cluster Template and Global Measurement of H α , The Astrophysical Journal, Vol. 533 (2), pp 744-780.
- Tytler, D., O'Meara, J. M., Suzuki, N., Lubin, D., (2000), Review of Big Bang Nucleosynthesis and Primordial Abundances, Particle Physics and the Universe, Proceedings of Nobel Symposium 109, Haga Slott, Enköping, Sweden, 20-25 August, 1998. Edited by L. Bergström, P. Carlson, and C. Fransson. Physica Scripta, Vol. T85, p.12,
- Wang, K., Wu, Y. F., Ran, L., Yu, W. T., Miller, M., (2009), The relation between $^{13}\text{CO } J = 2-1$ -line width in molecular clouds and bolometric luminosity of associated IRAS sources, Astronomy and Astrophysics, Vol. 507 (1), pp 369-376.
- Wang, R., Wagg, J., Carilli, C. L., Neri, R., Walter, F., Omont, A., Riechers, D. A., Bertoldi, F., Menten, K. M., Cox, P. et al., (2011), Far-infrared and Molecular CO Emission from the Host Galaxies of Faint Quasars at $z \sim 6$, The Astronomical Journal, Vol. 142 (4), pp 101-120.
- Wagoner, R. V., Fowler, W. A., Hoyle, F., (1967), On the Synthesis of Elements at Very High Temperatures, The Astrophysical Journal, Vol. 148, pp 3.
- Weiß A., Walter F., Scoville N. Z., (2005), The spectral energy distribution of CO lines in M 82, Astronomy and Astrophysics, Vol. 438 (2), pp 533-544.
- Weiss A., Downes D., Walter F., Henkel C., (2007), CO Line SEDs of High-Redshift QSOs and Submm Galaxies, in Baker A. J., Glenn J., Harris A. I., Mangum J. G., Yuneds M. S., eds, ASP Conf. Ser. Vol. 375, From Z-Machines to ALMA: (Sub)Millimeter Spectroscopy of Galaxies. Astron. Soc. Pac., San Francisco, p. 25

- Willner, S. P., Ashby, M. L. N., Barmby, P., Fazio, G. G., Pahre, M., Smith, H. A., Kennicutt, R. C. Jr., Calzetti, D., Dale, D. A., Draine, B. T., (2004), Infrared Array Camera (IRAC) Observations of M81, *Astrophysical Journal Supplement Series*, Vol. 154 (1), pp 222-228.
- Williams, M. J., Bureau, M., Cappellari, M., (2010), The Tully-Fisher relations of early-type spiral and S0 galaxies, *Monthly Notices of the Royal Astronomical Society*, Vol. 409 (4), pp 1330-1346
- Wilson R. W., Jefferts K. B., Penzias A. A., (1970), Carbon Monoxide in the Orion Nebula, *The Astronomical Journal*, Vol. 161, pp L43.
- Weinreb S., Barrett A. H., Meeks M. L., Henry J. C., (1963), Radio Observations of OH in the Interstellar Medium, *Nature*, Vol. 200 (4909), pp 829-831.
- Wilson, C. D., Warren, B. E., Israel, F. P., Serjeant, S., Attewell, D., Bendo, G. J., Butner, H. M., Chantal, P., Clements, D. L., Golding, J. et al., (2012), The JCMT Nearby Galaxies Legacy Survey — VIII. CO data and the LCO (3-2)-LFIR correlation in the SINGS sample, *Monthly Notices of the Royal Astronomical Society*, Vol. 424 (4), pp 3050-3080.
- Wootten A., (1981), A dense molecular cloud impacted by the W28 supernova remnant, *The Astrophysical Journal*, Vol. 245, pp 105-114.
- van der Tak, F. F. S., Black, J. H., Schöier, F. L., Jansen, D. J., van Dishoeck, E. F., (2007), A computer program for fast non-LTE analysis of interstellar line spectra. With diagnostic plots to interpret observed line intensity ratios, *Astronomy and Astrophysics*, Vol. 468 (2), June III 2007, pp.627-635.
- van Dishoeck E. F., Black J. H., (1988), The Photodissociation and Chemistry of Interstellar CO, *The Astrophysical Journal*, Vol. 334, pp 771.
- Young, J. S., Xie, S., Tacconi, L., Knezek, P., Viscuso, P., Tacconi-Garman, L., Scoville, N., Schneider, S., Schloerb, F. P., Lord, S. et al., (1995), The FCRAO Extragalactic CO Survey. I. The Data, *The Astrophysical Journal Supplement Series*, Vol. 98, pp 219.

CHAPTER 2

**THE MOLECULAR GAS, DUST AND STELLAR
POPULATION ACROSS THE DISK OF SPIRAL GALAXIES**

Assist. Prof. Selcuk TOPAL¹

¹Yüzüncü Yıl University, Faculty of Science, Department of Physics, Van, Turkey.
selcuktopal@yyu.edu.tr ORCID ID: 0000-0003-2132-5632

INTRODUCTION

There are different types of galaxies in the universe each has its own unique properties (Hubble 1936; de Vaucouleurs et al. 1991; Kormendy & Bender 2012). Spiral galaxies are rich in both molecular gas and dust and show a high level of star formation. However, elliptical galaxies are almost always devoid of gas. Lenticular galaxies, the type of galaxies in the middle of spiral and elliptical galaxies, are also mostly poor in gas, but some lenticulars have a considerable amount of molecular gas (ATLAS^{3D} survey; Young et al. 2011). Spiral galaxies are, therefore, exemplary targets to study star formation processes across the disk of galaxies.

The interplay between gas and dust in the interstellar medium (ISM) of galaxies has a key role in star formation, and the evolution of galaxies. Once hydrogen molecule (H_2) is formed on the surface of dust grains (Cazaux & Tielens 2002; Perets & Ofer 2006) the door for multiple other molecules from simple to more complex ones opens. Since each atomic, molecular and dust emission is a result of different physical properties in the ISM, multi-wavelength data are necessary to understand the structure and evolution of gas clouds, and star formation better.

Nearby galaxies appear to follow a color-magnitude relation, i.e. the galaxies on the red sequence are generally early-type galaxies (i.e. ellipticals and lenticulars) with much less star formation activity and cold gas, while the galaxies on the blue sequence are generally late-

type galaxies (namely spirals) with a high level of star formation (Baldry et al. 2004). It has been shown that the color-magnitude relation is also valid for nearby galaxy clusters and the clusters located up to $z = 1$ (Ellis et al. 1997; Sanchez-Blazquez et al. 2009). It is, therefore, important to study the gas and dust in galaxies to get better insights into galaxy evolution.

$3.6\mu\text{m}$ IR emission is barely affected by the extinction and could be produced by old stars and/or dust heated by young massive stars. The study of a large sample of galaxies showed that up to 30% of the total lights at $3.6\mu\text{m}$ originate from the dust heated by young massive stars (Querejeta et al. 2015). The $[3.6] - [4.5]$ color gradient in early-type galaxies (i.e. elliptical and lenticular galaxies) showed that most galaxies become redder through the outskirts (Peletier et al. 2012). While older stellar populations tend to have colors of $-0.2 < [3.6] - [4.5] < 0$ (Willner et al. 2004; Pahre et al. 2004; Peletier et al. 2012; Meidt et al. 2014), the $[3.6] - [4.5]$ color with a non-stellar origin is mostly positive, possibly due to hot dust, non-thermal emission or the existence of young massive stars (Querejeta et al. 2015). $3.6\mu\text{m}$ and $4.5\mu\text{m}$ dust emissions can be used to estimate the stellar mass, M_* , (Eskew et al. 2012; Querejeta et al. 2015), and the $[3.6] - [4.5]$ color also appears to have a dependence on redshift (Smit et al. 2014; Huang et al. 2016).

We targeted spiral galaxies NGC 5248 and NGC 3938 to study the interplay of gas, dust and stellar population across the disk of both galaxies. The galaxies have the multi-wavelength literature data of

$^{12}\text{CO}(1-0)$, $3.6\mu\text{m}$ and $4.5\mu\text{m}$ emissions at sub-kpc resolution. This allow us to study aforementioned properties of both galaxies in greater detail for the first time.

1. LITERATURE DATA

The disk of both galaxies was observed in $^{12}\text{CO}(1-0)$ emission as part of the BIMA SONG Survey (Helfer et al. 2003). We used the highest resolution CO data available for both galaxies, i.e. the beam size is 6 arcsec or ≈ 400 pc over the galaxies. Near-infrared (NIR) data at $3.6\mu\text{m}$ and $4.5\mu\text{m}$ wavelengths were taken from the *Spitzer Space Telescope Survey* (Werner et al. 2004) conducted using the Infrared Array Camera (IRAC; Fazio et al. 2004). The basic parameters for both galaxies can be found in Table 1.

Table 1. Basic properties of the spiral galaxies NGC 5248 and NGC 3938.

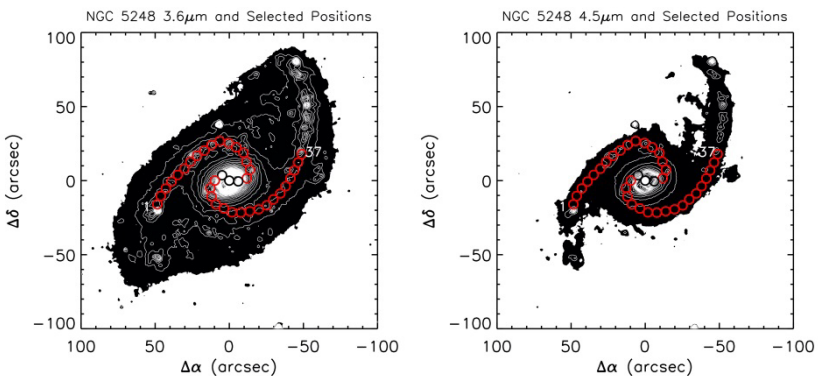
Property	NGC 5248	NGC 3938	Ref.
Hubble type	SAB(rs)bc	SA(s)c	a
RA (J2000)	$13^{\text{h}}37^{\text{m}}32^{\text{s}}$	$11^{\text{h}}52^{\text{m}}49.4^{\text{s}}$	a
Dec (J2000)	$+08^{\circ}53'6.6''$	$+44^{\circ}07'14.6''$	a
Major axis diameter (arcmin)	6.0	5.0	a
Minor axis diameter (arcmin)	5.0	5.0	a
V_{hel} (km/s)	1150	807	a
Distance (Mpc)	14.3	15.0	b
Inclination (degree)	56.4	17.6	b

^aNASA/IPAC Extragalactic Database (NED); ^bHyperLEDA (<http://leda.univ-lyon1.fr>)

2. DATA REDUCTION AND ANALYSIS

2.1. Position Selection

We selected multiple positions (including the center) located over the dusty disc of both galaxies, so the positions are bright at $3.6\mu\text{m}$ and $4.5\mu\text{m}$ wavelengths. The positions are located in the north-eastern (hereafter NE) and south-western (hereafter SW) of the center of each galaxy. There are 16 and 18 positions in the NE and SW, respectively, leading a total of 37 and 33 positions (including the center) in NGC 5248 and NGC 3938, respectively (see the illustration in Figure 1). The angular size of each selected position is 6 arcsec, equal to the beam size of $^{12}\text{CO}(1-0)$ data, i.e. the lowest angular resolution in the data set. Since we aim to compare molecular gas properties with that infrared, we chose 6 arcsec as the common spatial resolution. We, therefore, de-convolved $3.6\mu\text{m}$ and $4.5\mu\text{m}$ data to the common beam size to make the beam match in the data set (see Section 2.3). Selected positions over the disk of each galaxy are shown in Figure 1.



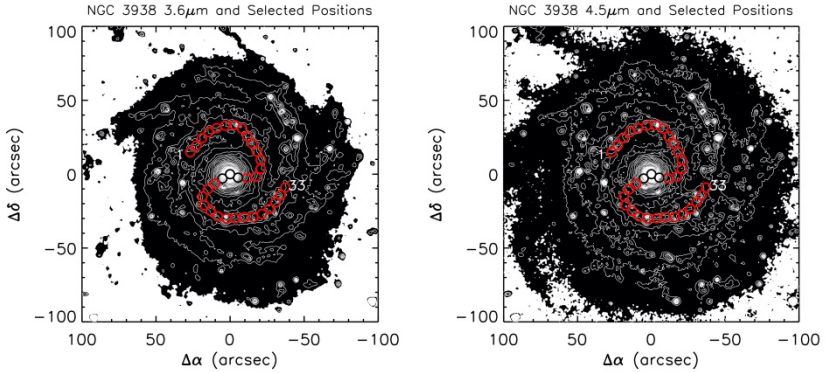


Figure 1: The selected positions (red and black circles) are overlaid on *Spitzer* $3.6\mu\text{m}$ and $4.5\mu\text{m}$ images (grayscale with white contours) of both galaxies. The top panels show the images for NGC 5248 while the bottom panels show the images for NGC 3938. Each circle has a diameter of 6 arcsec or a linear size of ≈ 400 pc at an average distance of 15 Mpc for both galaxies (see Table 1). The three positions within the brighter central region of size 1.2 kpc are shown by black circles. The numbering for the positions starts from the farthest position in the north-eastern, NE, (i.e. position 1), and it ends at the farthest position in the south-western, SW, (i.e. position 37 for NGC 5248 and position 33 for NGC 3938), i.e. the white numbers annotated in the images (see also Section 2.1). The corresponding position number for the center of NGC 5248 and NGC 3938 are 19 and 17, respectively. North is up and east to the left in all images.

2.2. Integrated CO Intensity, H_2 Mass and Surface Density

We extracted CO spectra from the selected positions in the CO data cubes using the *Multichannel Image Reconstruction Image Analysis and Display (MIRIAD; Sault et al. 1995)* task *imspect*. After extracting CO spectra we calculated the integrated CO line intensity, $T_{mb}d\nu$ [K km s^{-1}], by fitting a Gaussian function to the spectra. We carried out the fitting procedure using *Interactive Data Language (IDL)* code *MPFIT* (Markwardt 2009). *MPFIT* optimises the fitting parameters by applying Levenberg–Marquardt minimization algorithm. We defined the best-fitting Gaussian parameters by

applying the χ^2 test, i.e. the parameters with the smallest value of $\Delta\chi^2 = \chi^2 - \chi_{min}^2$ were defined as the best fit. The results of the fitting procedure are shown for the central three positions in Figure 2.

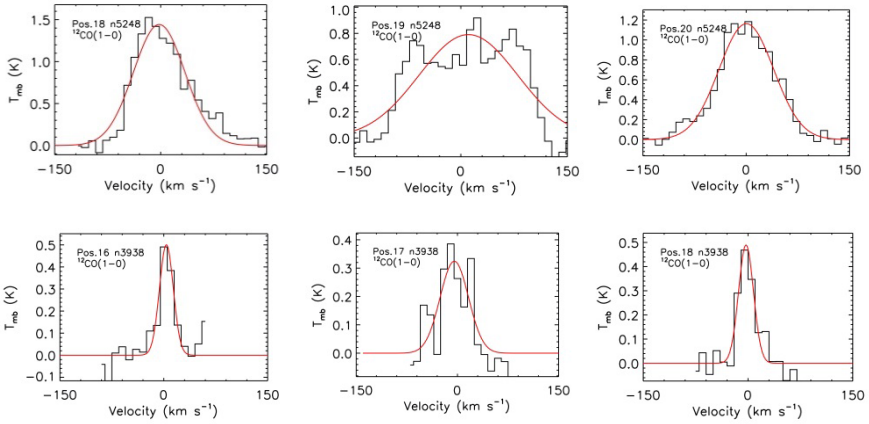


Figure 2: The CO Spectra Extracted from the Central Three Positions (see the black circles in Figure 1) in NGC 5248 (top panels) and NGC 3938 (bottom panels). The Red Line Represents the Best Gaussian Fits to the Spectra.

We estimated the total molecular gas mass (M_{H_2}) at the positions using the CO line intensity, and an adopted CO-to- H_2 conversion factor of $X_{CO} = 0.2 \times 10^{20} \text{ cm}^{-2} (\text{K km s}^{-1})^{-1}$ and $X_{CO} = 2 \times 10^{20} \text{ cm}^{-2} (\text{K km s}^{-1})^{-1}$ for the center (i.e. a region of size 1.2 kpc in diameter) and the disk of the galaxies, respectively. The reasons for these values are twofold; (1) the value of $X_{CO} = 2 \times 10^{20} \text{ cm}^{-2} (\text{K km s}^{-1})^{-1}$ is a widely accepted value for the disk of nearby spiral galaxies (Rosolowsky et al. 2003; Bolatto et al. 2008; Abdo et al. 2010; Donovan Meyer et al. 2012; Bolatto, Wolfire, & Leroy 2013), and (2) there is a depression in X_{CO} in the central region of galaxies compared to the disk, i.e. up to 10 times

lower (Bolatto et al. 2013; Sandstrom et al. 2013). The expression used to estimate the M_{H_2} is shown below (Bolatto et al. 2013).

$$M_{H_2} = C \left(\frac{I_{1-0}}{\text{K km s}^{-1}} \right), \quad (1)$$

where the values of C are $C = 6.4 \times 10^4$ and $C = 6.4 \times 10^5$ for the center and the disk of NGC 5248, respectively, and $C = 6.9 \times 10^4$ and $C = 6.9 \times 10^5$ for the center and disk of NGC 3938, respectively. The gas surface density (ΣH_2) was also estimated at each position as $\alpha_{\text{CO}} = \frac{\Sigma H_2}{I_{1-0}}$, where $\alpha_{\text{CO}} [M_{\odot} \text{pc}^{-2} (\text{K kms}^{-1})^{-1}] = \frac{X_{\text{CO}} [\text{cm}^{-2} (\text{K kms}^{-1})^{-1}]}{6.3 \times 10^{19}}$ (Narayanan et al. 2012), and I_{1-0} is the $^{12}\text{CO}(1-0)$ integrated intensity. The values of α_{CO} for the adopted X_{CO} are $\alpha_{\text{CO}} = 0.43 M_{\odot} (\text{K km s}^{-1})^{-1}$ and $\alpha_{\text{CO}} = 4.3 M_{\odot} (\text{K km s}^{-1})^{-1}$ for the center and disk of the galaxies, respectively (Narayanan et al. 2012). The integrated CO line intensities and corresponding M_{H_2} and ΣH_2 values, as a function of the galactocentric distance, are shown in Figure 3.

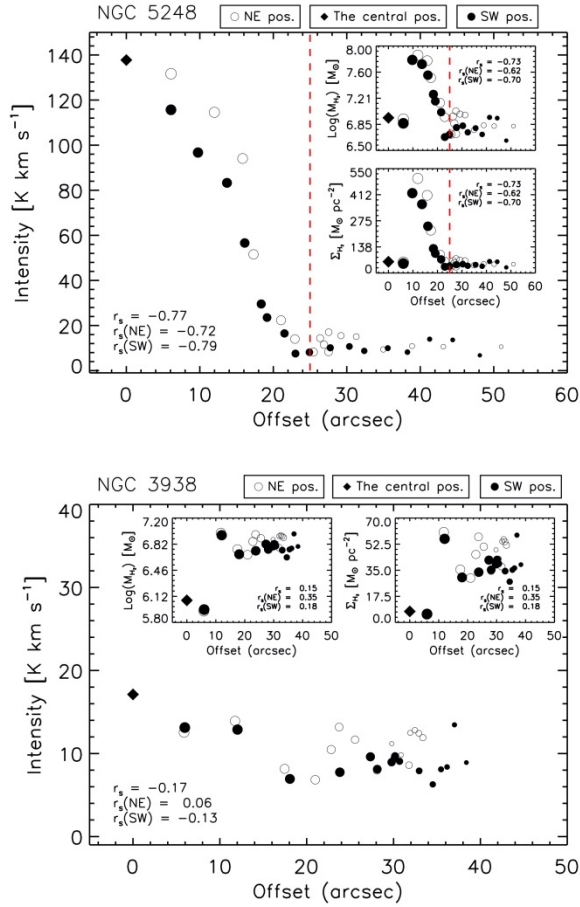


Figure 3: CO line intensities (main panels), molecular gas mass (M_{H_2}) and gas surface densities (Σ_{H_2}) (embedded panels) as a function of galactocentric distance. In all images, open and filled circles represent the values in the north-eastern (NE) and south-western (SW) arms of the galaxies, respectively, while filled black diamond shows the value at the center. The size of the symbols was also arranged specifically so that the smallest symbol represents the farthest position with respect to the center while the largest symbol indicates the closest position to the center. The name of the galaxies and the meaning of each symbol are also shown on the top of each panel. r_s values in the panels (including $r_s(NE)$ and $r_s(SW)$, i.e. the correlation for the positions only in the NE and SW, respectively) represent the *Spearman correlation coefficient* estimated for each pair of physical parameters, i.e. intensity vs. distance, M_{H_2} vs. distance and Σ_{H_2} vs. distance. The vertical dashed red lines in the top panels represent the angular distance of 25 arcsec from the center of NGC 5248 (see Section 3).

2.3. Near-infrared Fluxes, [3.6] – [4.5] Color and Stellar Mass

We calculated the beam averaged 3.6 μ m and 4.5 μ m NIR fluxes (hereafter $F_{3.6}$ and $F_{4.5}$, respectively) at the selected positions as explained below. We first applied a unit conversion necessary for *Spitzer* data (i.e. from MJy sr⁻¹ to Jy). We then multiplied the flux in each pixel in each image by a normalized 2D Gaussian function. The Gaussian function has an FWHM of 6 arcsec, i.e. the common beam size. We finally calculated the Gaussian weighted total NIR fluxes at each position by summing the weighted fluxes in all pixels in the image. We also calculated the stellar mass (M_*) using the $F_{3.6}$ and $F_{4.5}$ fluxes, and the expression below (Eskew et al. 2012),

$$\frac{M_*}{M_\odot} = 10^{5.65} \times \left(\frac{F_{3.6}}{\text{Jy}}\right) \times \left(\frac{F_{4.5}}{\text{Jy}}\right) \times \left(\frac{D}{0.05}\right), \quad (2)$$

where D is the distance to the galaxy in the unit of Mpc (see Table 1).

To calculate the [3.6] – [4.5] color, we first need to estimate the apparent magnitudes at both wavelengths. We, therefore, used the standard expression of $F_\nu = F_0 \times 10^{-m/2.5}$, where F_0 is the zero-point-flux densities at 3.6 μ m and 4.5 μ m, 280.9 Jy and 179.7 Jy, respectively (Reach et al. 2005). F_ν stands for the flux at 3.6 μ m and 4.5 μ m in the unit of Jy (i.e. $F_{3.6}$ and $F_{4.5}$, see above), and finally, m is the apparent magnitude at 3.6 μ m and 4.5 μ m. The [3.6] – [4.5] color as a function of M_* and the distance is shown in Figure 4.

3. RESULTS AND DISCUSSION

As seen from Figure 3, there is a strong negative correlation between the CO intensity and galactocentric distance (*Spearman correlation coefficient* $r_s = -0.77$) in NGC 5248, i.e. the CO intensity decreases sharply up to about 25 arcsec (or equivalently 1.7 kpc over the galaxy) from the center and then flattens (i.e. no considerable change in CO brightness) on each side of the disk. A similar correlation exists between the M_{H_2} and the distance, and between the ΣH_2 and the distance, after excluding the central three regions where there is a considerable decrease in M_{H_2} and ΣH_2 because of the assumed depression in X_{CO} .

However, the situation is quite different in NGC 3938. The CO intensity shows a very weak negative dependence on the galactocentric distance (see Figure 3), i.e. the correlation is more flatter compared to NGC 5248. The dependence of M_{H_2} and ΣH_2 on the distance in NGC 3938 is also weak but positive, after excluding the central positions (see the embedded panels in the bottom image of Figure 3).

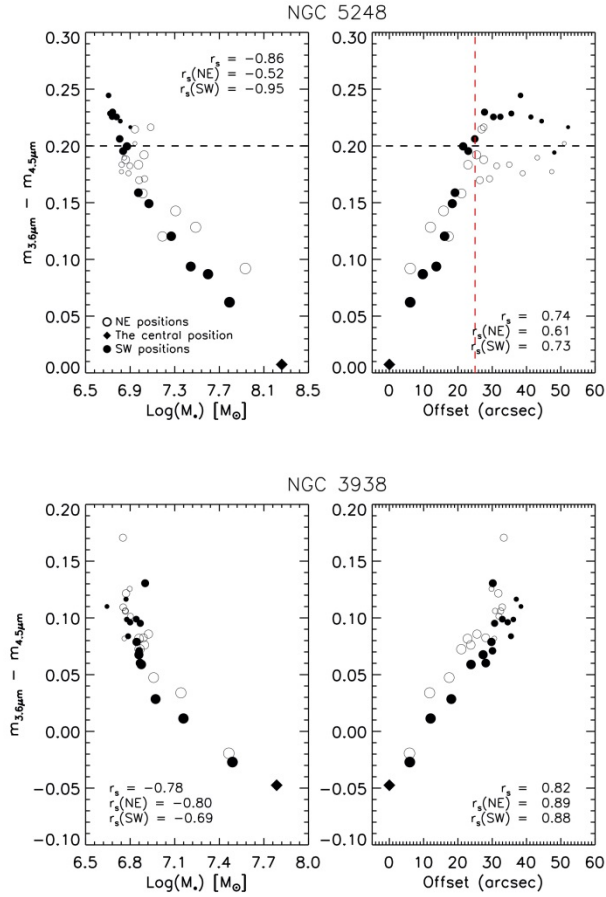


Figure 4: The $[3.6] - [4.5]$ color as a function of the stellar mass (M_*) and the galactocentric distance are shown for NGC 5248 (top) and NGC 3938 (bottom). The shape and size of the symbols were arranged as stated in the caption of Figure 2. The horizontal dashed black lines and the vertical dashed red line in the top panels (i.e. NGC 5248) represent the lowest end of the range for the $[3.6] - [4.5]$ color for diffuse dust (see Section 3), and the angular distance of 25 arcsec from the center, respectively. The *Spearman correlation coefficient*, r_s , is also shown in each panel (including the correlation for the NE and SW positions, $r_s(\text{NE})$ and $r_s(\text{SW})$, respectively).

In Figure 4, the correlation between the $[3.6] - [4.5]$ color and M_* , and between the color and galactocentric distance are shown. In both galaxies, there is a strong negative correlation between the $[3.6] -$

[4.5] color and M_* (i.e. $r_s = -0.86$ and $r_s = -0.78$ for NGC 5248 and NGC 3938, respectively). The correlation is stronger in the SW arm of NGC 5248 (i.e. $r_s(SW) = -0.95$) than the NE arm (i.e. $r_s(NE) = -0.52$), while the situation is the opposite in NGC 3938 (i.e. $r_s(NE) = -0.80$ and $r_s(SW) = -0.69$).

As Figure 4 indicates, there are two main differences between NGC 5248 and NGC 3938. Firstly, the central region and the outskirts of each galaxy shows some differences in terms of stellar population, although both galaxies have bluer colors in the center compared to their disks. While the color in the center of NGC 3938 resembles the color for old stellar populations (i.e. $-0.2 < [3.6] - [4.5] < 0$; Willner et al. 2004; Pahre et al. 2004; Peletier et al. 2012; Meidt et al. 2014), it is the opposite for the center of NGC 5248 (i.e. $[3.6] - [4.5] > 0$). Secondly, although the color continuously gets redder from the center to the outskirts in NGC 3938 it never exceeds 0.2 as opposed to NGC 5248. In NGC 5248, after about 25 arcsec from the center in the SW of the disk, $[3.6] - [4.5] > 0.2$ (except one position only), and then the color rather shows a flat distribution as the distance from the galaxy's center increases (see the top-right panel in Figure 4). However, in the NE arms of NGC 5248, all positions (except three positions only) have $[3.6] - [4.5] < 0.2$. The typical range for the $[3.6] - [4.5]$ color for diffuse dust $0.2 < [3.6] - [4.5] < 0.7$ (Querejeta et al. 2015). This indicates that after about 25 arcsec from the center in the SW of NGC 5248, the diffuse dust is dominating the ISM compared to the NE.

As seen in Figure 5, there is a strong positive correlation between M_* and M_{H_2} in NGC 5248 (i.e. $r_s = 0.83$), while the correlation is much weaker and negative in NGC 3938 ($r_s = -0.24$). The M_* has a strong negative correlation with the galactocentric distance in both galaxies (i.e. $r_s = -0.76$ and $r_s = -0.87$ for NGC 5248 and NGC 3938, respectively). Similar to the CO intensity, M_{H_2} , ΣH_2 , and the [3.6] – [4.5] color, after about 25 arcsec from the center M_* also shows a flat distribution as a function of the distance in the outskirts of NGC 5248 (see the top-right panel in Figure 5). However, the M_* continuously decreases from the center to the outskirts in NGC 3938.

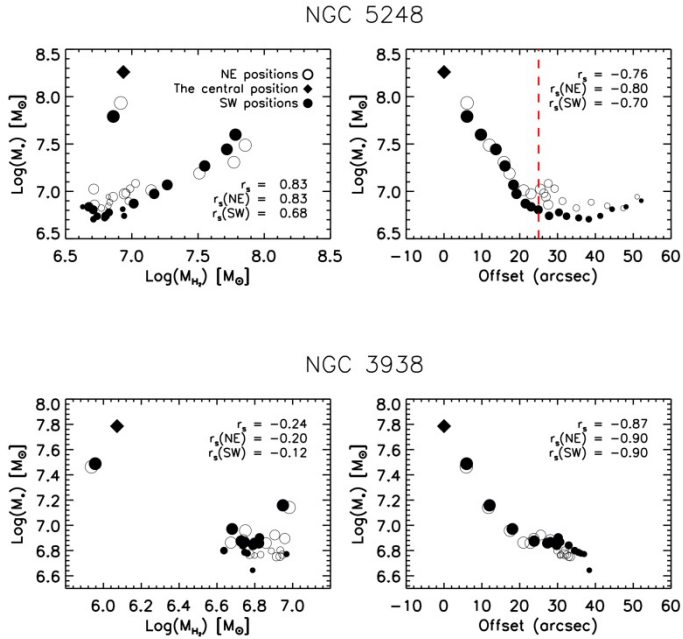


Figure 5: The stellar mass (M_*) as a function of M_{H_2} and the galactocentric distance is shown for NGC 5248 (top panels) and NGC 3938 (bottom panels). The vertical dashed red line in the top-right panel represents the angular distance of 25 arcsec from the center of NGC 5248. The size of the symbols was defined as stated in the caption of Figure 2. The Spearman correlation coefficient for all positions (i.e. r_s)

and the positions in the NE (i.e. $r_s(NE)$) and SW (i.e. $r_s(SW)$) is also shown in each panel. The correlations involving M_{H_2} does not include the data for the central three positions (i.e. the positions 18, 19 and 20 for NGC 5248, and the positions 16,17 and 18 for NGC 3938, see Figure 1), because of the assumed depression in X_{CO} causing the substantial decrease in M_{H_2} .

CONCLUSION

Multiple positions across the spiral arms of NGC 5248 and NGC 3938 were studied using multi-wavelength data including $^{12}\text{CO}(1-0)$ transition and $3.6\mu\text{m}$ and $4.5\mu\text{m}$ NIR emissions. Molecular gas mass (M_{H_2}), gas surface density (ΣH_2), $[3.6] - [4.5]$ color and stellar mass (M_*) were obtained for each position studied, including the central region. Our main conclusions are as follows.

- 1- The integrated CO intensity shows a radial gradient with a strong correlation with the galactocentric distance in NGC 5248, i.e. the intensity decreases sharply up to about 25 arcsec from the center and then it flattens. The same behavior is seen for the M_{H_2} and ΣH_2 , after excluding the central three positions where there is an assumed depression in X_{CO} . On the contrary, there is no strong (or even mild) correlation between the CO intensity and the galactocentric distance across the disk of NGC 3938 (and this is also true for M_{H_2} and ΣH_2). The spiral arms of NGC 3938 seem to have an ISM with a different level of star formation processes compared to NGC 5248.
- 2- Each galaxy shows a color gradient, i.e. the galaxies get redder from the center to the outskirts. The central region of NGC 3938 has negative (the bluest) colors indicating the old stellar

populations dominating the ISM there. However, the [3.6] – [4.5] color is always positive across the disk of NGC 5248.

- 3- The galaxies also show different behavior in their outskirts. In the outskirts of NGC 5248 (after 25 arcsec from the center in the SW arm), the [3.6] – [4.5] > 0.2. However the [3.6] – [4.5] is always lower than 0.2 across the disk of NGC 3938. This indicates that the diffuse dust could be dominating the outskirts of NGC 5248 compared to the rest of its disk and the disk of NGC 3938. As NGC 5248 is a member of the galaxy group, this could explain the diffuse dust at the outskirts of the galaxy where any interactions with nearby galaxies could be more effective.

Overall, in NGC 5248, the integrated CO intensity, M_{H_2} and $\sum H_2$ decrease while the stellar mass and the value of the [3.6] – [4.5] color increase up to about 25 arcsec from the center. However, after 25 arcsec from the center in NGC 5248, the distribution of all parameters as a function of the galactocentric distance flattens. In NGC 3938, there is no statistically significant correlation between the CO intensity (also M_{H_2} and $\sum H_2$) and the galactocentric distance. However, the correlations between the M_* and distance ($r_s = -0.87$) and between the [3.6] – [4.5] color and distance ($r_s = 0.82$) are strong in NGC 3938. Additionally, there is a strong positive correlation between the M_{H_2} and M_* in NGC 5248 ($r_s = 0.83$, excluding the central three positions), whereas there is no such correlation seen in NGC 3938 ($r_s = -0.24$). The correlation between

the $[3.6] - [4.5]$ color and M_* is negative and strong in both galaxies, i.e. the M_* increases as the $[3.6] - [4.5]$ color gets bluer from the outskirts to the center. However, the strength of the correlation between the M_* and $[3.6] - [4.5]$ color in the NE and SW arms of each galaxy is different.

ACKNOWLEDGEMENTS

This work is based [in part] on archival data obtained with the Spitzer Space Telescope, which was operated by the Jet Propulsion Laboratory, California Institute of Technology under a contract with NASA. We acknowledge the usage of the HyperLEDA database (<http://leda.univ-lyon1.fr>). This research has made use of the NASA/IPAC Extragalactic Database (NED), which is operated by the Jet Propulsion Laboratory, California Institute of Technology, under contract with the National Aeronautics and Space Administration.

REFERENCES

- Abdo, A. A., Ackermann, M., Ajello, M., Baldini, L., Ballet, J., Barbiellini, G., Bastieri, D., Baughman, B. M., Bechtol, K., Bellazzini, R. ve ark., (2010), Fermi Observations of Cassiopeia and Cepheus: Diffuse Gamma-ray Emission in the Outer Galaxy, *The Astrophysical Journal*, Vol. 710 (1), pp 133-149.
- Baldry I. K., Glazebrook K., Brinkmann J., Ivezić Z., Lupton R. H., Nichol R. C., Szalay A. S., (2004), Quantifying the Bimodal Color-Magnitude Distribution of Galaxies, *The Astrophysical Journal*, Vol. 600 (2), pp 681-694.
- Bolatto A. D., Leroy A. K., Rosolowsky E., Walter F., Blitz L., (2008), The Resolved Properties of Extragalactic Giant Molecular Clouds, *The Astrophysical Journal*, Vol. 686 (2), pp 948-965.
- Bolatto A. D., Wolfire M., Leroy A. K., (2013), The CO-to-H₂ Conversion Factor, *Annual Review of Astronomy and Astrophysics*, Vol. 51 (1), pp 207-268.
- Cazaux, S. and A. Tielens, (2002), Molecular hydrogen formation in the interstellar medium. *The Astrophysical Journal*, Vol. 575 (1), pp L29-L32.
- de Vaucouleurs G., de Vaucouleurs A., Corwin, Jr. H. G., Buta R. J., Paturel G., Fouqu_e P., (1991), Third Reference Catalogue of Bright Galaxies. Volume I: Explanations and references. Volume II: Data for galaxies between 0h and 12h. Volume III: Data for galaxies between 12h and 24h.
- Donovan M., J., Koda, J., Momose, R., Fukuhara, M., Mooney, T., Towers, S., Egusa, F., Kennicutt, R., Kuno, N., Carty, M., ve ark., (2012), Resolved Measurements of X_CO in NGC 6946, *The Astrophysical Journal*, Vol. 744 (1), pp 42-52.
- Ellis R. S., Smail I., Dressler A., Couch W. J., Oemler A., Jr, Butcher H., Sharples R. M., (1997), The Homogeneity of Spheroidal Populations in Distant Clusters, *The Astrophysical Journal*, Vol. 483 (2), pp 582-590.
- Eskew M., Zaritsky D., Meidt S., (2012), Converting from 3.6 and 4.5 μ m Fluxes to Stellar Mass, *The Astronomical Journal*, Vol. 143 (6), pp 139-145.

- Fazio, G. G. ; Hora, J. L., Allen, L. E., Ashby, M. L. N., Barmby, P., Deutsch, L. K., Huang, J. -S., Kleiner, S., Marengo, M., Megeath, S. T. et al. (2004), The Infrared Array Camera (IRAC) for the Spitzer Space Telescope, *The Astrophysical Journal Supplement Series*, Vol. 154, pp 10-17.
- Helfer, T. T., Thornley, M. D., Regan, M. W., Wong, T., Sheth, K., Vogel, S. N., Blitz, L., Bock, D. C. J., (2003), The BIMA Survey of Nearby Galaxies (BIMA SONG). II. The CO Data, *The Astrophysical Journal Supplement Series*, Vol. 145 (2), pp 259-327.
- Huang, K-H., Bradač, M., Lemaux, B. C., Ryan, R. E. Jr., Hoag, A., Castellano, M., Amorín, R., Fontana, A., Brammer, G. B., Cain, B., Lubin, L. M., Merlin, E., Schmidt, K. B., Schrabback, T., Treu, T., Gonzalez, A. H., von der Linden, A., Knight, R. I. (2016), Spitzer Ultra Faint Survey Program (SURFS UP). II. IRAC-detected Lyman-Break Galaxies at $6 \lesssim z \lesssim 10$ behind Strong-lensing Clusters, *The Astrophysical Journal*, Vol. 817 (1), pp 11-32.
- Hubble, E.P., (1936), *Realm of the Nebulae*, by E.P. Hubble. New Haven: Yale University Press, 1936. ISBN 9780300025002
- Kormendy J., Bender R., (2012), A Revised Parallel-sequence Morphological Classification of Galaxies: Structure and Formation of S0 and Spheroidal Galaxies, *The Astrophysical Journal Supplement Series*, Vol. 198 (1), pp 2-41.
- Markwardt C. B., (2009), Non-linear Least-squares Fitting in IDL with MPFIT”, *Astronomical Society of the Pacific Conference Series*, *Astronomical Data Analysis Software and Systems XVIII.*, Quebec City, QC, Canada, 411, 251-254.
- Meidt, Sharon E.; Schinnerer, Eva; van de Ven, Glenn; Zaritsky, Dennis; Peletier, Reynier; Knapen, Johan H.; Sheth, Kartik; Regan, Michael; Querejeta, Miguel; Muñoz-Mateos, Juan-Carlos, (2014), Reconstructing the Stellar Mass Distributions of Galaxies Using S4G IRAC 3.6 and 4.5 μm Images. II. The Conversion from Light to Mass, *The Astrophysical Journal*, Vol. 788 (2), pp 144-155.

- Narayanan, D., Krumholz, M., Ostriker, E. C., Hernquist, L., (2012), A general model for the CO–H₂ conversion factor in galaxies with applications to the star formation law, *Monthly Notices of the Royal Astronomical Society*, Vol. 421, pp 3127–3146.
- Pahre, Michael A., Ashby, M. L. N., Fazio, G. G., Willner, S. P., (2004), Mid-Infrared Galaxy Morphology along the Hubble Sequence, *Astrophysical Journal Supplement Series*, Vol. 154, pp 235-241.
- Pelletier, R. F., Kutdemir, E., van der Wolk, G., Falcón-Barroso, J., Bacon, R., Bureau, M., Cappellari, M., Davies, R. L, de Zeeuw, P. T., Emsellem, E., (2012), The SAURON project - XX. The Spitzer [3.6] - [4.5] colour in early-type galaxies: colours, colour gradients and inverted scaling relations, *Monthly Notices of the Royal Astronomical Society*. Vol. 419 (3), pp 2031-2053.
- Perets, H. B., Ofer, B., (2006), Molecular hydrogen formation on porous dust grains, *Monthly Notices of the Royal Astronomical Society*, Vol. 365 (3), pp 801-806.
- Querejeta, M., Meidt, S. E., Schinnerer, E., Cisternas, M., Muñoz-Mateos, J. C., Sheth, K., Knapen, J., van de Ven, G., Norris, M. A., Reynier, P., (2015), The Spitzer Survey of Stellar Structure in Galaxies (S4G): Precise Stellar Mass Distributions from Automated Dust Correction at 3.6 μm, *Astrophysical Journal Supplement Series*, Vol. 219, pp 5-23.
- Reach, William T., Megeath, S. T., Cohen, M., Hora, J., Carey, S., Surace, J., Willner, S. P., Barmby, P., Wilson, G., Glaccum, W., et al., (2005), Absolute Calibration of the Infrared Array Camera on the Spitzer Space Telescope, *The Publications of the Astronomical Society of the Pacific*, Vol. 117 (835), pp 978-990.
- Rosolowsky E., Engargiola G., Plambeck R., Blitz L., (2003), Giant Molecular Clouds in M33. II. High-Resolution Observations, *The Astrophysical Journal*, Vol. 599 (1), pp 258-274.
- Sánchez-Blázquez, P., Jablonka, P., Noll, S., Poggianti, B. M., Moustakas, J., Milvang-Jensen, B., Halliday, C., Aragón-Salamanca, A., Saglia, R. P.,

- Desai, V., (2009), Evolution of red-sequence cluster galaxies from redshift 0.8 to 0.4: ages, metallicities, and morphologies, *Astronomy and Astrophysics*, Vol. 499 (1), pp 47-68.
- Sault R. J., Teuben P. J., Wright M. C. H., (1995), A Retrospective View of MIRIAD, *Astronomical Society of the Pacific Conference Series, Astronomical Data Analysis Software and Systems IV.*, Baltimore, Maryland, USA, 77, 433-436,
- Sandstrom, K. M., Leroy, A. K., Walter, F., Bolatto, A. D., Croxall, K. V., Draine, B. T., Wilson, C. D., Wolfire, M., Calzetti, D., Kennicutt, R. C. ve ark., (2013), The CO-to-H₂ Conversion Factor and Dust-to-gas Ratio on Kiloparsec Scales in Nearby Galaxies, *The Astrophysical Journal*, Vol. 777 (1), pp 5-37.
- Smit, R., Bouwens, R. J., Labbé, I., Zheng, W., Bradley, L., Donahue, M. ; Lemze, D., Moustakas, J., Umetsu, K., Zitrin, A. et al. (2014), Evidence for Ubiquitous High-equivalent-width Nebular Emission in $z \sim 7$ Galaxies: Toward a Clean Measurement of the Specific Star-formation Rate Using a Sample of Bright, Magnified Galaxies, *The Astrophysical Journal*, Vol. 784, pp 58-65.
- Werner, M. W., Roellig, T. L., Low, F. J., Rieke, G. H., Rieke, M., Hoffmann, W. F., Young, E., Houck, J. R., Brandl, B., Fazio, G. G. et al. (2004), The Spitzer Space Telescope Mission, *The Astrophysical Journal Supplement Series*, Vol. 154, pp 1-9.
- Willner, S. P., Ashby, M. L. N., Barmby, P., Fazio, G. G., Pahre, M., Smith, H. A., Kennicutt, R. C. Jr., Calzetti, D., Dale, D. A., Draine, B. T., (2004), Infrared Array Camera (IRAC) Observations of M81, *Astrophysical Journal Supplement Series*, Vol. 154 (1), pp 222-228.
- Young, Lisa M., Bureau, M., Davis, Timothy A., Combes, F., McDermid, R. M., Alatalo, K., Blitz, L., Bois, M., Bournaud, F., Cappellari, M., Davies, R. L., de Zeeuw, P. T., Emsellem, E., Khochfar, S., Krajnović, D., Kuntschner, H., Lablanche, P., Morganti, R., Naab, T., Oosterloo, T., Sarzi M., Scott, N., Serra, P., Weijmans, A., (2011), The ATLAS3D project - IV. The

molecular gas content of early-type galaxies, *Monthly Notices of the Royal Astronomical Society*, Vol. 414, pp 940-967.

CHAPTER 3

ON THE COPPER-BASED MATERIALS CORROSION

Dr. Cristian Ștefan DUMITRIU¹

¹ SC Utilnavorep SA, Technical Office of Design, Technologies, Research, Constanta, Romania; E-mail: cris.dum.stef@gmail.com

INTRODUCTION

Corrosion is a complex process of destroying metals and alloys under chemical, electrochemical or microbial action. Thousands of tons of materials are annually lost due to this process. So, knowing the mechanism of this process and finding solution to diminish the effects are important from industrial and financial viewpoints. Given that, this chapter discusses the different types of corrosion, with emphasize on copper-based alloys materials.

1.CONSIDERATIONS ON THE CORROSION OF METALLIC MATERIALS

Corrosion is a complex process affecting most of the metallic material used in industry. Taking into account the producing mechanism, it can be classified as chemical, electrochemical or microbiological.

Chemical corrosion brings together the destruction processes that occur through the direct chemical interaction of the metal with the environment, without an exchange of electrical charges (in the absence of moisture).

Electrochemical corrosion occurs at the contact of a metal with an electrolyte, by charge transfer through the interface; for example, corrosion of metallic materials in aqueous solutions of acids, bases and salts, or corrosion of metals in the atmosphere.

Microbiological corrosion appears in the presence of microorganisms that corrode the metal by producing metabolites with corrosive action, cell agglomeration or by cathode depolarization by retaining hydrogen and electrons under the enzymatic action.

Since the aim of this paper is to analyse the copper-base alloys destruction by corrosion, on what follows, the corrosions types encountered in these alloys are discussed. Corrosion forms that affect the copper-based alloys are affecting most metals, with few exceptions. In the case of copper pipes the following types of corrosion have been identified [Oliphant, 2003]:

- type I pitting - in the presence of water with a temperature lower than 40°C (Fig. 1- left);
- type II pitting - in the presence of fresh water, with low pH;
- rosace corrosion - in copper cylinders for hot water, with Al bumper (Fig.1 - right);

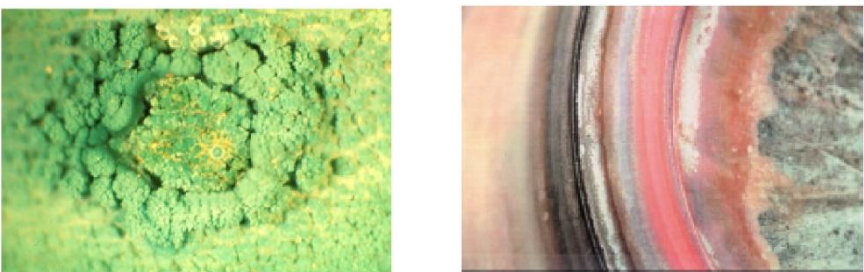


Figure 1. Type I pitting and rosacea pitting [Oliphant 2003]

- induced microbiological corrosion (Fig.2);
- erosion-corrosion, due to the flow rate of a liquid;
- corrosion induced by welding flux.



Figure 2. Microbiological corrosion [Oliphant 2003]

Copper and its alloys are subject to the following corrosion:

a. *Generalized corrosion* is uniform over the entire surface of the alloy. It usually occurs in less aggressive environments, after a prolonged contact with it (in drinking water, in neutral salts solutions, organic acids, soil).

b. *Pitting corrosion* is caused by the existence of an incomplete protective film on the metal surface, which allows the pronounced location of the two electrode processes (Fig. 3)

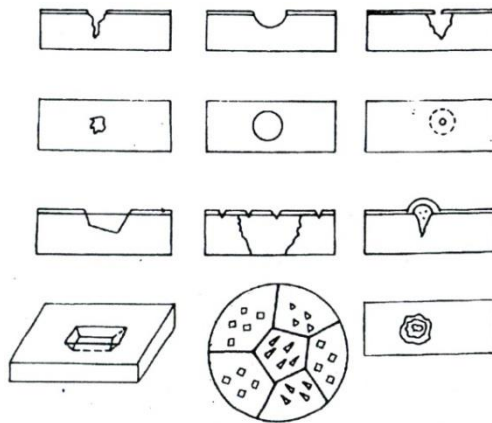


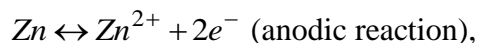
Figure 3. Pitting corrosion [Zamfir et al., 1994]

c. *Dezincification* is specific to Cu - Zn alloys with a Zn content over 15% and occurs in neutral and weakly acidic solutions. The phenomenon consists in the oxidation of zinc (anodic process) and its passage in solution, while copper reduces the oxygen in the solution (cathodic process), depositing in the form of a porous film. This film forms a micropile with brass, accentuating the corrosion process. Once initialized, the dezincification continues under the initial copper deposit, obtaining a soft material, permeable to gases and liquids. This is the theory of zinc dissolution, with the copper redeposition (Fig. 4).



Figure 4. Corrosion of a brass CuZn30 [Zamfir et al., 1994]

The second theory, of zinc dissolution, cannot explain the continuation of the process, because zinc ions accumulate in the point imperfections of copper. In both theories, the main reactions that take place are:



There is a local elimination of Zn the seawater that can penetrate the entire material thickness. The main product of reaction, which accompanies this process is $ZnCl_2$ that adheres to the material [Zamfir et al., 1994].

Dezincification is more pronounced in strongly alkaline or acidic environments, in the presence of sulfur gases, chlorides and amines and is accentuated by impurities in the material (Fe, Pb, Sb, Mn). The biphasic brasses are dezincificated in two stages, firstly the β phase, richer in zinc, then the α phase.

Dezincification can be prevented by reducing the Zn content below 15% or by adding small amounts of As (1.4%) or Sb (0.04%), resulting in inhibited brasses. It can also be reduced by alloying with tin and aluminum.

d. *Tensile corrosion* of copper alloys most often occurs in the form of intercrystalline cracks - *corrosion by cracking* - or in the form of *transcrystalline cracks*. It is the result of the simultaneous action of the corrosive environment and direct or residual mechanical stresses present in the affected part. Its particularity is that neither the environment nor the stresses could cause the crack if they act independently. The effect appears unexpected and rapid after a normal work period of, leading to the sometimes catastrophic destruction of structures and installations [npl.co.uk].

This form of corrosion occurs in dilute solutions and especially in ammonia vapors (in the brass case) or ammonium compounds.

Oxygen, carbon dioxide and moisture increase the ammonia action. Mercury salts produce the crack of the tensioned copper alloys. Cracking occurs in the both cases of applied and residual stress. The possibility alloys intercrystalline cracking increases with the size of the applied stress and can also be initiated by corrosion points. The alloy components also influence the cracking. Thus, brass with zinc content higher than 40% cracks very easily. Phosphorus, magnesium, tellurium, beryllium reduce the tendency to crack. of Cracking prevention is achieved either by using copper alloys with a low Zn content, or by reducing the residual stresses of the alloy by annealing it at 200 - 400 °C, for several hours, using various protective metal layers or varnishes and paints, or improving the corrosive environment.

To avoid this type of corrosion, the conditions in which the material is susceptible to stress cracking must be known and should be avoided from the design phase.

For example, a heat exchanger [Bărbulescu and Barbes, 2021] has the inner pipes and inner body made of stainless steel or copper alloy (because it must have a small thickness to ensure the heat transfer and has to be corrosion resistant), whereas the outer pipes and outer coating are of steel carbon (because they can be thicker to compensate the corrosion effect). This construction has this structure because the carbon steel adopts an electrode potential that is below the potential corresponding to the stainless steel corrosion by cracking or pitting, having the effect of protecting the steel. If the exchanger were built

only of stainless steel, the electrochemical process would no longer be unidirectional (stainless steel - carbon steel), losing the protection of small thickness pipes and thus the destruction of the heat exchanger [npl.co.uk; Dumitriu and Bărbulescu, 2007].

- e. *Fatigue corrosion*. The combined action of corrosion (usually pointlike) and alternating alloys tension can lead to fatigue corrosion cracks. In this situation, the alloy surface is covered by pinches at whose base, the crack (mainly transcrystalline) is observed. Cu - Be, Cu - Ni alloys, phosphor bronze, and aluminum bronze are well resistant to this type of corrosion.
- f. *Intercrystalline* corrosion is characteristic of solid solution structures, the alloy destruction occurring around the grains edges even in the absence of mechanical stresses inside them. The penetration depth is of a few grains from the alloy surface, which takes on a rough appearance.

The preferential destruction of the grain boundaries is due either to their more active character or to the separation of some phases, usually intermetallic compounds, with different electrode potential than the alloy matrix.

The corrosion of CuZn₃₀ brass in iron chloride shows that at the beginning of the process, the chemical potentials at the boundary and inside the grain are different, and then they equalize. As a result, the grain boundary dissolution begins, but the corrosion penetration into the grain is not observed. In ammoniacal solutions, in the oxygen presence, the grain boundaries are anodic, whereas in the absence of

oxygen, the boundaries act as cathodes. This could also explain the different behavior of brass, depending on whether the ammonia medium is gaseous or liquid [Zamfir et al., 1994].

This type of corrosion occurs in steam installations under high pressure, in Muntz metal, Admiralty brass, Si and Al bronze.

g. Corrosion - erosion occurs when gases, vapours, and liquids pass rapidly on the metal surface. Their action results in destroying the protective film, which allows the metal surface to be attacked in the exposed places. This type of corrosion occurs especially in condenser systems that use seawater, which draws air at high flow rates and propellers. It can be attenuated using Cu - Ni alloys.

According to some authors, corrosion-erosion is a particular type of pitting corrosion [Zamfir et al., 1994], while others consider it a special or a complex corrosion type [Dumitriu and Bărbulescu, 2007; Florea and Panaitescu, 1979; Necleba, 1955].

Corrosion - erosion can be an effect of cavitation, which is a dynamic process of formation, development and collapse of bubbles or cavities filled with vapours and gases in the mass of liquid Bărbulescu, 2006; Bărbulescu and Mârza, 2006; Bărbulescu et al., 2010; Bărbulescu and Dumitriu, 2006, 2007; Dumitriu and Dragomir, 2021].

Cavitation can be explained by 4 hypotheses [Florea, V. Panaitescu, 1979]:

- mechanical, in which the appearance of large local voltages and strong noises is observed. This does not explain why materials with lower mechanical strength are stronger than those with higher mechanical strength (for example, bronze is superior to steel);
- chemical, which states that the metals destruction is done by chemical effect and shows that the water vapours and gases release atomic oxygen, very aggressive chemically, that corrode the metal;
- thermodynamic, which associates to the cavitation the existence of thousands degrees temperatures, appeared by the vapours recondensation, which weaken the metal resistance;
- electrical, which explains the apparition of the cavitation process by the potential difference between the gas and liquid bubbles.

Regardless the way of explaining the corrosion-erosion produced by cavitation, its effects are determined by a series of factors classified into:

- characteristics of the sample: mechanical and metallurgical, surface roughness, stress and strain state;
- environmental characteristics: the existence of cavitation germs, pressure and temperature, speed of liquid flow [Simionov, 1997].

In the literature it is specified that the finely processed surfaces are more resistant than those with high roughness. The resistance to

cavitation of the chromed surfaces increases by approximately 15%. [Corrosion control, 1984; Plimosenko, 1983].

2. CONSIDERATIONS ON THE CORROSION OF THE COPPER-BASED ALLOYS

2.1. Copper-based alloys

In the non-alloy state, copper has good use qualities, but only in certain areas and only over a fairly short period. Alloying Cu, as a basic element, with various metals or non-metals (C, Si, P) that have different or similar physical, chemical and mechanical properties leads to increased mechanical strength, extended flow limit or increased hardness and corrosion resistance in specific environments.

Copper-based alloys fall into two broad categories:

- brass, which are solid solutions of zinc in copper, that may contain Mn, Fe, Al, Ni, Pb, Sn;
- bronzes, that are copper alloys in which the main alloying elements are Sn, Al, Pb, Si, Mn, not Zn and Ni.

Brass, characterized by good tensile strength and ductility, is used in both construction and industry. It can be simple (binary) and special. *Binary brasses* have no alloying elements and are resistant to atmospheric air (even humid). The presence in the moist air of SO₂, H₂S, CO₂ leads to their rapid corrosion. Their technological use is due to properties such as: corrosion resistance, bonding capacities with Sn - Pb alloys, cold and hot forming capacities, machinability by cutting, good chroming and nickel plating capacities.

Special brasses are brasses whose compositions include alloying elements such as: Mn, Fe, Sn, Pb, Al. Among the most common are those with Si, Al, Sn. They are more resistant than the binary ones, but still easy to process, being suitable for foundry purposes.

Brass with Si. Introduced into the melt, Si becomes a powerful deoxidizer, improving casting properties, fluidity and weldability. Silicon has good anticorrosive properties in fresh and salt water up to flow rates of 5m/s, and the formed alloy retains its mechanical properties up to temperatures of -183°C . In general, Si replaces Sn, to reduce the manufacturing costs.

Tin brass is used in areas more affected by corrosion, the role of Sn being to prevent the appearance of dezincification.

Aluminum brass stands out for the rather large contribution they have in the range of construction materials. Al forms a thin film of compact and adherent oxide on the surface of the alloy, which leads to a good corrosion resistance at high temperature conditions. In quantities greater than 3.5%, it increases the breaking strength, without decreasing the tenacity. In the shipbuilding industry, aluminum brass is mainly used to make grilles for the ventilation system. These alloys can be subject to certain heat hardening treatments. The addition of nickel leads to the formation of a fine granulation, increasing the corrosion resistance, tenacity and considerably improving the mechanical properties.

Currently, the term *bronze* refers to a wide range of copper-based alloys that contain various metals, including Sn, in small amounts or

not at all. The most common bronzes are those with tin (Cu - Sn), phosphorus (Cu - Sn-P), lead (Cu - Pb), aluminum (Cu - Al), zinc (Cu - Sn - Zn), silicon and manganese (Cu - Si - Mn), and with beryllium (BzBe, BzBeCo).

Tin bronzes are the most diversified, their compositions containing only Cu and Sn (binary bronzes), or complex compositions, which include various alloying elements (special bronzes) [Plimosenko, 1983].

Cu-Sn binary bronze contains 6-14% Sn, and the rest Cu. By the interaction of the two components, eight intermetallic phases are formed in the solid state, depending on the Sn concentration, of which the first and the last are solid substitution solutions. The α phase represents the solid solution of tin substitution in copper and has a cubic network with centered faces. The maximum solubility of Sn is 15.8% at 520°C. Depending on the temperature, the β, γ, δ phases can also appear or σ - formed by the eutectoid decomposition of the γ phase at 420°C. The most important transformation in the solid phase of bronzes remains, however, the eutectoid decomposition of the γ phase into a crystalline aggregate of $\alpha + \delta$ at 520°C.

Under very slow cooling conditions, the structure of 14% Sn is composed of solid solution grains. Under normal cooling conditions, this alloy contains two constituents: solid solution grains and $\alpha + \delta$ eutectoid, with pointlike aspect.

The tensile strength is directly proportional and the elongation is inversely proportional to the amount of Sn in the alloy [Gâdea and Protopopescu, 1975]. 6% Sn bronzes are cold and hot deformable.

The harmful impurities of these bronzes are: O₂, Al and Fe. O₂ forms SnO₂, which represents hard and brittle inclusions in the alloy. Al causes the formation of large grains and micropores. Fe, Si, Sb, As, Bi reduce the hot and cold plasticity of rolled bronzes.

In terms of use, Sn alloys are divided into six groups. Group I contains alloys with 7-8% Sn, used for cold processed springs or turbine wings. Group 2 includes alloys that make the transition to special bronzes (universal bronze 5-5-5, in percentages of Sn - Zn - Pb and lead bronze containing 5% Zn and 20% Pb). They are used for laminated products. Group 3 contains alloys with 8-10% Sn, plus Zn in small quantities. They are used to make machine details. Group 4 contains phosphorous bronzes (6-14% Zn, 0.1 ÷ 0.6% P, plus Ni and Pb). They are used for bearings and gears, shaft sleeves, pump rotors, due to their good mechanical qualities and corrosion resistance. Group 5 contains bronzes for bearings with 10 ÷ 14% Sn and 8 ÷ 20% Pb. Group 6 includes bell bronzes with Sn up to 30%, zinc and lead in small quantities.

Among the technological properties of Cu-Sn alloys one may notice: good corrosion resistance in air and sea water, wear resistance, strong hardening by strain hardness, very good weldability, cold malleability of α bronzes.

The disadvantages of this type of bronze are: the tendency of segregation and formation of porosity on the surface of castings, low fluidity and increased fragility (in the case of bronzes with high tin content).

Phosphorous bronzes are obtained from the deoxidation of bronzes with tin, with a phosphorous copper pre-alloy added in small quantities before the tin addition. The addition of up to 0.5% phosphorus helps to deoxidize copper and increase the alloy fluidity. With less than 0.3% phosphorus, the alloy is elastic, non-magnetic and easily weldable. If the phosphorus content is higher, the alloy becomes much harder because the copper phosphide (Cu₃P) compound appears in its structure.

Lead bronzes are widely used due to the special structure of the alloy, explained by the fact that the solubility of lead in copper is practically zero, so that when the alloy solidifies, the lead separates in the metallic form at the grain boundary. The size and distribution of lead particles in the metal mass determine the alloys antifriction qualities. The lead existence in alloys increases the machinability, compactness of castings and stability to acid corrosion. The addition of Zn increases the fluidity and reduces the tendency of sulphides apparition. The addition of Ni reduces the grains and improves the mechanical properties of the alloys, giving them hardness at normal and high temperatures.

Pb-P bronze, obtained by adding 3.5% Pb in phosphorous bronze, is more suitable for manufacturing high speed and pressure resistant

bearings. Alloys with a Pb content below 0.5% are used to produce gaskets for steam and water pipes and for ornamental works. Alloys for high performance bearings are obtained by alloying bronzes with Sn with an amount of up to 20% Pb.

Bronze with Zn (red bronze) is obtained by combining amounts of about 88% Cu with Sn and Zn. Nickel red bronze contains up to 5% Ni. Zinc bronzes are used to produce components for machine building, including bearings.

Aluminum bronzes contain, apart of Cu and Al, small quantities of other metals, such as Ni, Fe, Mn. Complementary alloying with Fe (3-5%) leads to finishing the alloys structure, giving them strength and hardness. Mn, in the presence of Fe, acts in the same direction with it. Basically, the bronze alloyed such a way is as strong as mild steel and has a good resistance to corrosion, including the action of dilute acids.

Harmful impurities of bronzes with Al are: Sn (worsens mechanical properties, produces microcracks and gives fragility to cast parts), P (reduces the mechanical characteristics and compactness), Si (reduces compactness), Sb, As.

From a structural point of view, aluminum bronzes have three phases of practical interest - α, β, γ . The α phase is a solid solution of Al with Cu, which crystallizes in the cubic system with centered faces. The maximum solubility of Al in Cu is 9.4% at 565°C. The phase is an intermediate solution based on the compound Cu_3Al and crystallizes

in a cubic lattice with centred volume. The β phase is also an intermediate solution based on a new $\text{Cu}_{32}\text{Al}_{19}$ compound.

Due to the mentioned technological properties, aluminium bronzes are the most used in the manufacture of discs for ballast plant valves, fire extinguishing, deck washing with sea water, compressed air installation, winch bushes, stops, roller nostrils, in the manufacture of naval propellers, parts for hydraulic equipment, such as tanks and acid - resistant pumps.

Silicon bronzes can replace Cu - Sn binary alloys for some purposes. The role of silicon is to reduce the tendency of gas saturation and copper oxidation, increasing the fluidity and shrinkage on solidification. The important phases are α - stable at low temperatures and γ .

Industrial silicon bronzes contain 1.5 - 4% Si and are single-phase alloys (α). Their alloying with Mn leads to the formation of a new alloy with a content between 4 - 5% Si and 1 - 1.5% Mn, stronger than bronzes with Sn, approaching weakly alloyed steels.

Silicon bronzes may also contain Zn and Pb. Their use is recommended up to 30 daN/cm² and 120°C. They are employed in chemical and oil equipment, sanitary installations, draft measuring installations. They do not give sparks and, therefore, are appropriate to make tools and devices that work in explosive environments.

Manganese bronzes are bronzes for foundry use, generally having up to 8% Mn. Their structure contains a solid solution, which is suitable

for plastic deformation, in hot and cold conditions. They does not show solid state transformations. Complex alloys with Zn, Al, Fe and Ni are used in casting naval propellers.

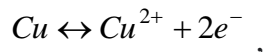
Beryllium bronzes are very important due to their exceptional properties of strength and hardness, elasticity and resistance to fatigue and wear. Their utilization is more limited, as special materials.

2.2. Corrosion resistance of copper and its alloys in different environments

Corrosion is a complex phenomenon, which depends on the composition and structure of the metal phase, the nature and composition of the corrosive medium, the conditions under which the component reactions take place.

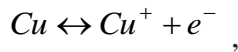
Copper is a moderately noble element that can form two types of compounds: monovalent ions and bivalent ions (compounds in which copper is trivalent are unstable). Their solubility significantly differs greatly, exerting an important influence on the corrosion resistance, due to the resulting standard electrochemical potential.

In the presence of copper (Cu^+) and cupric (Cu^{2+}) ions in solution, the equilibrium can be established on an electrode:



with the standard voltage (V)

$$\varphi_{\text{Cu}/\text{Cu}^{2+}}^0 = 0.34$$



with the standard voltage (V)

$$\varphi_{\text{Cu}/\text{Cu}^+}^0 = 0.52 .$$

With a more positive standard potential than the hydrogen electrode, Cu cannot replace H₂ from non-oxidizing acids. Under normal conditions, Cu cannot substitute H₂ in acidic solutions. Fe, Pb, Zn substitutes it in solutions in which Cu is dissolved in the form of salts.

Copper and its alloys have excellent corrosion performances. Since its reaction power is not high, it corrodes a little, even when it is not protected by anti-corrosion films. In copper that has undergone a heat treatment and in its alloys, in contact with some more noble materials and in aqueous solutions of some of its salts, pronounced corrosive processes appear. It is recommended to avoid the contact of copper parts, especially in corrosive environments, with a number of other metallic materials (Fe, Al, Mg, Zn, galvanized steel, etc.).

➤ *Corrosive effects of acid solutions*

Copper does not replace H₂ in non-oxidizing acid solutions and therefore should not corrode it. During their handling, the solution dissolves air, which causes depolarization of local cathodes, favouring the onset and evolution of corrosion. The appearance of ions (ferric, tin, cupric, mercuric or chromic) and the presence of strong acids (favored by the increase of temperature) in the operating environment, leads to increased corrosion sensitivity of Cu and its alloys with Zn.

➤ *Corrosive effects of neutral and alkaline solutions*

Aerated alkaline solutions attack Cu-based alloys. The use of Cu should be avoided in ammonium solutions, which are particularly aggressive towards Cu in the state of tension.

Copper is also not permitted in solutions with complex compounds containing oxidizing agents (ferric or tin compounds).

Neutral salt solutions, if not excessively aerated, do not attack copper and some of its alloys. Basic solutions attack brass. Ammonium hydroxide is notable for its high aggressiveness, leading to corrosive processes under stress.

➤ *Corrosive effects of seawater*

The layer formed on the surface of the copper parts, in the sea water, includes oxychloride, hydroxide and basic copper carbonate, as well as calcium sulfate and copper oxide. Copper alloys have a good resistance to general corrosion and pitting in stagnant seawater, their corrosion rate being less than 0.025 mm/year.

The corrosion rate of Cu and, to a lesser extent of brass and Cu-Ni alloys, increases with the speed of seawater circulation, which is visible in Fig.5.

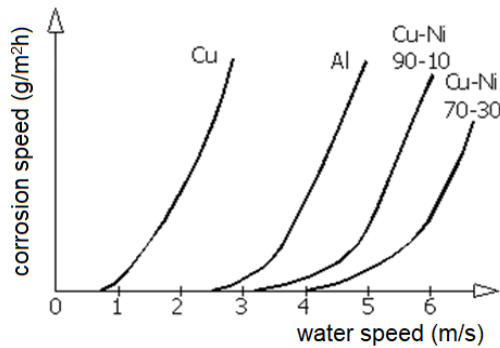


Figure.5. Variation of the corrosion rate of some alloy pipes as a function of the speed of seawater circulation

The corrosion resistance of copper alloys is explained by the fact that the toxicity of its salts prevents the fixation on the surface of microorganisms and vegetation, thus allowing the formation of a protective layer. Alloys with 16% and 30% Ni and 0.24% Cr are very resistant to erosion and turbulent corrosion, due to a very good adhesion of the passivation layer. In estuaries, harbours, and coastal areas, pollution causes water deoxidation, which leads to the formation of sulphur compounds and hydrogen sulphides. As a result, the protective oxide film can no longer form on the surface of the immersed metal. It is replaced with a film containing sulphide compounds, which accelerates the intergranular corrosion.

Cu-Ni alloys are resistant to corrosion by pitting even in seawater polluted or contaminated with NH_3 .

➤ *Corrosive effects of fresh water*

Freshwater causes the same type of corrosion as saltwater, but with a lower intensity. In non-aerated waters, the oxidation process is very

slow. Corrosive processes do not occur in the condensates (without CO₂) obtained in the installations.

In unpolluted atmospheres and in strongly aerated surface waters, copper is covered with a continuous and protective layer of oxides (resistant to increased oxidation, at high temperatures).

In atmospheres with saline mists or sulphur gases, oxychloride also appears in the composition of the respective layer. In wet ones, the protective layer also contains basic copper sulphate.

In surface waters, copper establishes a potential that varies very little over time and with the pH. Therefore, copper was used in manufacturing the pipes for transporting water and tanks, pipes for heat exchangers, having the advantage of very good heat transmission.

Dezincification is specific to warm or hot water, not too hard, with slow or stagnant movement, which contains chlorides.

Unpolluted water used to supply heat exchangers does not have a marked corrosive action if there are no calcium carbonate deposits, at working temperatures, deposits that lead to a pronounced disturbance of heat transfer.

In low hardness waters, which contain some dissolved gases (O₂, CO₂), the corrosion rates appreciably increase. However, if the copper parts are brought into contact with nickel, lead and tin alloys, the speeds become negligible. If the water pH is below 5, the corrosive attack of copper increases.

➤ *Corrosion in the atmosphere and soil*

Copper is very resistant to the atmosphere. Corrosion results in the appearance of sulphides and oxides on its surface. In a humid atmosphere (55%), CuSO_4 results through the subsequent action of sulfuric acid and the sulfides oxidation. By hydrating, an adherent and continuous film of basic copper sulfate, $\text{CuSO}_4 \cdot \text{Cu}(\text{OH})_2$ appears. Over time, the basicity increases and the brochantite, $\text{CuSO}_4 \cdot 3\text{Cu}(\text{OH})_2$ results. At the seashore, the main component of the copper rust is the basic copper chloride, whereas in mountainous areas, basic copper nitrate resulted after the atmospheric electrical discharges.

➤ *Corrosive effects of other substances*

In reducing gaseous media (H_2 , CO , hydrocarbons), at high temperatures and if Cu was not well deoxidized, it is affected by the hydrogen disease. The humidity, associated with hydrogen sulphide, NO_2 or NH_3 , causes intense corrosion, even at normal temperatures (25°C). O_2 , CO_2 , H_2S (dissolved in condensate or accidental splashing) have an aggressive action on brass. Brasses with a high zinc content better resists to the H_2S action.

The halogens vapours, in dry environment, at normal temperature, have a slow corrosive action, but become aggressive in humid environments, with the temperature increase.

Solutions of hypochlorite, hydrogen peroxide, molten sulphur are corrosive, while gasoline, benzene and glycerine do not attack copper.

Alkaline hypochlorite solutions, although oxidizing, have less aggressiveness on brass.

Chlorinated hydrocarbons (in the presence of accelerators such as humidity, acids, chlorine and photo-decomposition products) corrode more or less the copper and its alloys. If the operating media is dry, however, parts made of copper can be used.

Copper has a mediocre resistance and is not recommended for use in ammonia media, ammonium salts, sulphides, halogens, oxidizing acids, concentrated hydrochloric and sulphuric acids, molten metals, alkaline melts, etc. It is sensitive to the action of alkaline soils and those with a high content of carbonates, sulphates or other sulphur compounds. It should be mentioned that the metallic constructions should be electrical insulated at the contact points between two different metals, because in these places, corrosive phenomena occur on the other metal, copper being always the cathode.

➤ *Brass corrosion*

-In chloride solutions, the speed of corrosive processes increases appreciably as the operating temperature increases [Gonzales and Mârza Roşca,1999]. Therefore, although copper and its alloys offer known advantages in terms of heat transfer, they are not recommended at temperatures above 90°C and in the presence of aggressive waters (dissolved halides).

Acidic, non-oxidizing salts, dissolved in water, also lead to corrosive processes due to the hydrolyze. In the case of ammonium chloride, its aggressiveness increases with the degree of aeration and agitation of the solution. Cyanides, silicates, phosphates and alkaline carbonates have a certain aggressiveness, the appearance of carbon dioxide increasing the value of the latter. Chromic acid and bichromates are much more aggressive, as well as the salts of some metals (Fe^+ , Hg^{2+}).

Single-phase brasses are susceptible to stress cracking corrosion in the presence of wet ammonium vapours or certain ammonium compounds (Fig.6) [Zamfir et al., 1994].

Thus, the alloy with zinc content over 15% can be destroyed by stress cracking corrosion, a sensitivity that increases with increasing zinc content. In the case of single-phase alloys, there is a direct proportional dependence between the susceptibility to cracking corrosion and the grain size.

The concentration of ammonia influences the crack susceptibility of brass as shown in Fig.7 [Zamfir et al., 1994].

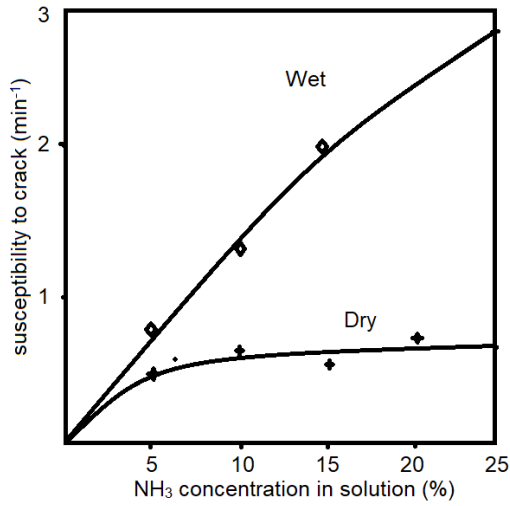


Figure 6. Susceptibility to cracking of brass samples tested in ammonia [Zamfir et al., 1994]

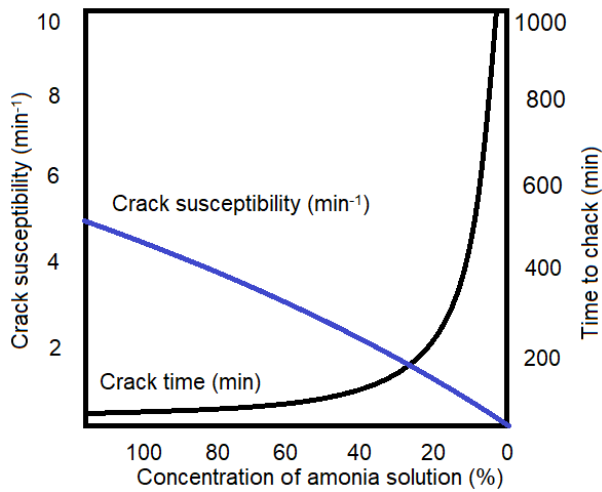


Figure 8. The influence of ammonia solution concentration on the susceptibility and duration of brass cracking [Zamfir et al., 1994]

➤ *Bronze corrosion*

Bronzes are used to some extent in chemical industries, with a number of advantages, such as higher corrosion resistance than brass,

pours well, withstands chloride solutions, seawater, natural and steam. Among the bronzes with Sn, more resistant to corrosion are those with 4% Sn and 3% Zn, as well as the one with 3% Sn, 2% Zn and 5% Pb. For high pressure steam, the one with 3% Sn, 11% Zn and 4% Pb is recommended.

Bronzes with Al (5 - 10% Al, 2 - 5% Fe, 0 - 5% Ni, 10 - 13% Mn) have a good resistance to oxidizing media, dilute inorganic acids, water, halide solutions, steam (a protective film of Al_2O_3), NH_3 , and anhydrous CO_2 , sulfuric, phosphoric, citric, lactic and acetic acid, fatty acids, formaldehyde, sea water, hot gases (400 – 600°C), dilute solutions of dilute inorganic acids, etc. Their use in alkaline solutions is not recommended.

Bronzes with 8% Al dissolve selectively. Cu-Al-Mn bronzes do not present porosity from corrosion. They have good mechanical properties and high corrosion resistance.

Silicon bronzes have high corrosion stability in freshwater, seawater, crude oil, petroleum products and are resistant to polluted atmospheres, seawater and wastewater, HCl, sulfates, chlorides, bases and basic salts, and alcohols.

3. METHODS FOR DETERMINING THE RESISTANCE OF MATERIALS TO CORROSION

To solve practical problems related to the choice of corrosion-resistant alloys, the replacement of expensive or deficient metals with accessible ones, the control of protective coatings, etc. it is necessary

to know the corrosion resistance of different materials.

Methods for determining corrosion resistance are classified in according to different criteria, as follows [Hagymaş et al, 1993].

- According to the place and test conditions: in nature, in natural conditions [Antropov, 1979], in the laboratory.

Among the tests in laboratory conditions we mention: tests of corrosion resistance in uncovered vessels (it is the simplest method for determining the corrosion indices, weight variation, mechanical properties and pitting), tests of resistance to corrosion in gases at high temperature, volumetric methods (which allow the determination of hydrogen released by corrosion of metals in acid solutions), the method of radioactive isotopes, electrochemical methods, the polarized light method (for measuring the layer thickness of corrosion films in polarized light), the colour interference method, etc.

- The methods types [Bacinschi, 2001]:

- 1) Qualitative: examination of the external appearance and photography of the sample, visual observation of the changes produced in the solution, microscopic and macroscopic examination;
- 2) Quantitative, which in turn are divided into:
 - a. *Methods that depend on the nature of corrosive destruction:* determination of the time of the first corrosion center occurrence (Kc), the number of corrosion centers (Kn), the thickness of the sample and the depth of the pinch (Kd) and the weight loss

(when the products corrosion can be easily removed from the surface). The following indexes are utilized:

- *The gravimetric index*, which represents the variation of the mass of the test piece or machine by the action of corrosion, divided by the surface (s) and the time unit (t) [g /m²h or mg/dm².day].
- *Volumetric index*, which represents the variation of the volume of the test piece or machine by the action of corrosion, divided by the surface (s) and the time unit (t). It is expressed in cm³/ cm² day, cm³/ m²h, cm³/dm²day.
- *The penetration index* represents the average decrease of the metal layer thickness in time (mm /year).

The assessment of the metal resistance to pointlike corrosion can be done by the number of points on a limited material surface:

$$Frequency (\%) = n / N \cdot 100,$$

where N is the number of squares into which the surface of the material has been divided, and n - the number of squares containing one or more points of attack.

Literature present studies on the interdependence between the cavitation damage and mechanical properties (resilience limit, hardness, tensile strength) for six materials (aluminium, copper, phosphor bronze, brass, stainless steel, stainless steel) [Rao Symala et al., 1971]. The choice of cavitation-resistant materials can be made using the relation [Oniciu, 1986]:

$$V_r M_r^m = C,$$

where: C is a coefficient.

- $V_r = \left[\frac{V}{t} \right]_x / \left[\frac{V}{t} \right]_0$ is the ratio between the volume loss over time of a certain material and that of a reference material;
- $M_r = M_x / M_0$ is the ratio between the mechanical characteristic of a certain material and that of a standard material;
- m is an exponent that depends on the material nature;

Leight and Thompson [1974] also performed experiments to correlate the metal resistance to cavitation with its mechanical properties (tensile strength, hardness).

b. Methods that depend on the nature of the destruction:

- determination of weight gain, which is used when the corrosion products are insoluble in the respective aggressive environment and very adherent to the surface of the samples;
- determination of the amounts of hydrogen released;
- determination of the amount of oxygen absorbed.

To assess the duration of metals resistance over time to the corrosive action of different media, different tables may be utilized. They contain the corrosion rates defined by the gravimetric or penetration indexes and establish different resistance groups. These conventional tables or scales can be employed if the determinations under natural

conditions have indicated that the corrosion process uniformly manifests on the metal surface. However, if the corrosion manifests in a localized form, the table can only be used as a guide.

Sometimes an assessment is made depending on the penetration in the metal wall, expressed as a percentage. For example, it is considered that a machine must be replaced when the pitting has penetrated the metal wall to a depth of 10% of its thickness.

CONCLUSION

In this chapter we gave an overview of the corrosion types, with emphasize on the copper-based alloys. Experimental results will be presented in a future work.

REFERENCES

- Antropov, L. (1979) *Electrochimie théorique*, MIR, Moscou.
- Bacinschi, Z. (2001) *Materials with the form memory*, Macarie, Târgoviște.
- Bărbulescu, A. (2006) Models of the voltage induced by cavitation in hydrocarbons, *Acta Physica Polonica B*, vol. 37 no. 10 (2006), pp. 2919 – 2931.
- Bărbulescu, A. Barbes, L. Modeling the outlet temperature in heat exchangers. Case study, *Thermal Science*, vol. 25, No.1B (2021), pp. 591-602.
- Bărbulescu, A. Dumitriu, C.S. Mathematical aspects of the study of the cavitation in liquids, Proceedings of the 4th Workshop on Mathematical Modeling of Environmental and Life Sciences Problems, Constanța, 7 - 11.09.2005, Romanian Academy Publishing House, Bucharest, 2006, pp. 7-14
- Bărbulescu, A. Dumitriu, C.S. Models of the mass loss of some copper alloys, *Stiintific Bulletin of Politehnica University (Timișoara)*, vol. 52, no 66, 1-2 (2007), pp. 120-123.
- Bărbulescu, A. Mârza, V. Electrical effect induced at the boundary of an acoustic cavitation zone, *Acta Physica Polonica B*, vol. 37, no. 2 (2006), pp. 507 – 518.
- Bărbulescu, A. Mârza, V. Dumitriu, C.S. Patent no RO 123086-B1 (30.09.2010), Installation and method for measuring and determining the effects produced by cavitation in ultrasound field in stationary and circulating media.
- Dumitriu, C. S., Bărbulescu, A. (2007) *Studies on the copper base alloys used in naval constructions – modeling the loss mass in different media*, Sitech, Craiova.
- Dumitriu, C. S., Dragomir, F. L., Modeling the signals collected in cavitation field by stochastic and Artificial intelligence methods, 13th International Conference on Electronics, Computers and Artificial Intelligence (ECAI), 01 July - 03 July 2021, Pitești, Romania, 2021, pp. 1-4
- Florea, J.. Panaitescu, V. (1979) *Fluids mechanics*, Editura Didactică și Pedagogică, București.

- Oliphant, R. J. (2003) *Causes of copper corrosion in plumbing systems*, Foundation for Water Research, The Listons.
- Gâdea, S., Protopopescu, M. (1975) *Non-ferrous alloys*, Editura Tehnică, București
- Gonzales, I. E., Mârza Roșca, I. Atmospheric corrosion of copper in a tropical climate, *Revista de chimie*, vol. **12** (1999), pp. 875-879.
- Hagymaș, G., Firoiu, C., Radovici, O. (1963) *Corrosion and metals protection*, Editura Tehnică, Bucuresti.
- Leith, W.C., Thompson, A. L. Some Corrosion Effects in Accelerated Cavitation Damage, *Journal of Basic Engineering*, vol. 82, no.4, (Dec. 1960), pp. 795 – 802.
- Lupu, A., Constantinescu, M., Drimuș, I. (1982) *Corrosion inhibitors for metals protection*, Editura Tehnică, București.
- Necleba, M. *Das problem der Kavitation*, *Maschinenbautechnik*, vol. 4, no 2 (Feb. 1955), pp. 81 – 88
- L. Oniciu (1986) *Materials corrosion. Fundamental aspects and anti-corrosive protection*, Editura Științifică și Enciclopedică, București.
- Plimosenko, A. P. (1983) *Zasita sudovih dizeloi ot kavitationih rezrusenii*, Sudostroenie, Leningrad, 1983.
- Rao Symala, B. C., Rao Lakshmana, N. S., Seetharamiah, K. (1971) *Selected metals and Alloys to Resist Cavitation Damage*, Water Power.
- Simionov, M. (1997) *Studies and researches on the destruction by cavitation of the sleeves of Diesel engines*, Ph. D. Thesis, "Dunărea de Jos" University, Galați.
- Zamfir, S., Vidu, R., Brînzoi, V. (1994). *Corrosion of the metallic materials*, Editura Didactică și Pedagogică, Bucharest.
- ***, Corrosion control in boiler installations. Collection of documentary material, Bucharest, Romania, 1964.
- ***, Guides to Good practice in Corrosion Control. Stress Corrosion Cracking, www.npl.co.uk.

CHAPTER 4

PRINCIPLES AND ENVIRONMENTAL APPLICATIONS OF THE SONOCHEMISTRY AND SONOCHEMICALLY ASSISTED ADVANCED OXIDATION PROCESSES

Assist. Prof. Dr. Murat KIRANŞAN^{1*}

¹ University of Gumushane, Vocational School of Gumushane, Department of Chemistry and Chemical Processing Technologies, 29100-Gümüşhane, TURKEY. ORCID ID <http://orcid.org/0000-0002-8520-6563>

*murat.kiransan@gumushane.edu.tr (*Corresponding Author)

INTRODUCTION

Population and industry in our world are increasing day by day very quickly. While the number of the people is increasing quickly, natural resources are decreasing too much to be renewed. In this case it brings environmental problems. One of these problems is water pollution. Water pollution constitutes an important part of the environmental problems (Uğurlu, 2002). It is reported that nearly 4 billion people around the world do not have access to clean water and millions of the people die every year due to the inaccessibility of the clean and sterile water (Chong et al., 2010). It is reported that the water pollution will increase in the near future due to the inability to prevent the pollution leaking into the natural water cycle from the human induced activities (Viessman et al., 1998). Today, an increase is the observed in the number of the materials synthesized by using multifunctional derived industrial products and high tech industries (Carlsen et al., 2013). As a result of the increasing number of the harmful substances in the industrial wastewater today, researchers have directed this issue and studies on the environmental pollution have to gained importance (Clarke et al., 1995). Additives organic dyes and pharmaceutical wastes used in food production, which pollute nature and adversely affect health in textile applications are considered as the causes of environmental pollution (Sanghi et al., 2002). Biological and chemical treatment, electrochemical methods, coagulation, filtration, flocculation, adsorption and chemical oxidation methods can be used to prevent from the harmful of the chemical wastes in the aquatic

environment. The most preferred among these processes is the adsorption due to its high efficiency (Walker et al., 2003). As an alternative to these processes are preferred advanced oxidation processes (AOPs), which provide higher efficiency and support lower energy consumption. Advanced oxidation processes (AOPs) is an oxidation method based on the reaction of the highly reactive species such as the hydroxyl radicals ($\bullet\text{OH}$) and organic pollutants (Akdağ Anıt, 2016). Although many techniques are available in the scope of the advanced oxidation processes (AOPs), the basic group of AOPs is four. These; fenton and photo-fenton are processes of the ozonation, photolysis and photocatalysis, sonolysis and sonocatalysis. These oxidation processes can generate many types of the reactive free radicals, mainly hydroxyl radicals ($\bullet\text{OH}$) in situ in the chemical reactions. The hydroxyl radical ($\bullet\text{OH}$) is a selective oxidizer capable of oxidizing a wide variety of the organic molecules (Gogate and Pandit, 2004).

1. SONOCHEMISTRY

The use of ultrasound to create chemical processes with cavitation bubbles is named sonochemistry (Mahvi, 2009). As it is known, although light progress to a certain depth in the liquids, sound or ultrasound can take much longer distances. Ultrasound used in the sonolytic applications is defined as a sound higher than 16 kHz (16000 cycles/s), which is outside the upper limits that the human ear can hear. During the cycle of the ultrasound wave, the water molecules separate and combine (Gogate et al., 2004). Ultrasound,

which has a wide frequency range, can be divided into two groups depending on its use, as the low amplitude (high frequency) sound and high amplitude (low frequency) sound (Halliday and Resnick, 1992). On the physical changes in the environment of wave in the low amplitude sound it is effective. These waves are in the range of 2-10 MHz. Mixing in the chemical applications due to the movement of the fluid it is used in the processes and is known as an acoustic mixer. High amplitude sound is known as “power ultrasound” and is in the range of 20-100 kHz. High amplitude waves are used in the removal of industrial wastewater and in the sonochemistry applications (Mamadiev and Yılmaz, 2011). Ultrasound process is the process of the to be activated liquids, especially water very well at high frequency, with a very high sound to produce strong chemical reactions and physical processes (Ince et al., 2001). Ultrasound cavitation is the phenomenon in which microbubbles growth and break in a very small time interval such as milliseconds, releasing a large amount of the energy (Gogate and Pandit, 2004). Acoustic bubbles reach critical sizes after a few cycles. The critical size of the bubbles is the inversely proportional to the frequency. The stable lifetime of the bubbles formed is less than 2 microseconds. They have degradation times of less than 100 nanoseconds (Thompson and Doraiswamy, 1999). Both the permanent and temporary bubbles are the formed during ultrasound cavitation. Both bubbles formed contribute to the chemical effects of the ultrasound cavitation. Permanent bubbles can be stay in the equilibrium continuously. Maintain their shape and structure during the ultrasonic effect. The

temporary bubbles formed break up after a few cycles and disperse in the solution (Thompson and Doraiswamy, 1999; Deveci, 2015). Under the influence of the positive pressure, the cavitation bubbles grow slowly. When they finally reach their critical size, the cavitation bubbles collapse and break up (Pang et al., 2011). Water pollutants can be oxidized by the energy and radicals revealed during ultrasonic cavitation of the bubbles. The sonolytic reactions that occur during cavitation are inside the bubble, at the bubble-liquid interface and in the liquid it takes (Papadaki, 2004). The temperature in the bubble and the interface between the bubble and the liquid temperature can be reach high temperatures such as the 4500-5000 K (Ince et al., 2001). Ultrasonic irradiation can also be considered as a clean and safety process. However, the main disadvantage in the commercializing the ultrasonic irradiation process, as it requires high operating costs may be the high energy consumption (Chu et al., 2017). The degradation of the organic pollutants as a result of the sonochemical reactions takes happen in three reaction region (Figure 1). Decomposition reactions takes happen inside the cavitation bubble (Region 1), in the interface region between the cavitation bubble and the bulk solution (Region 2) and in the bulk solution (Region 3) (Eren, 2012; Yap et al., 2019). Localized temperature points (Region 1) are created inside the cavitation bubble. The temperature and pressure in this region too high. It can be reach 5000 K and 1000 atm (Chu et al., 2017).

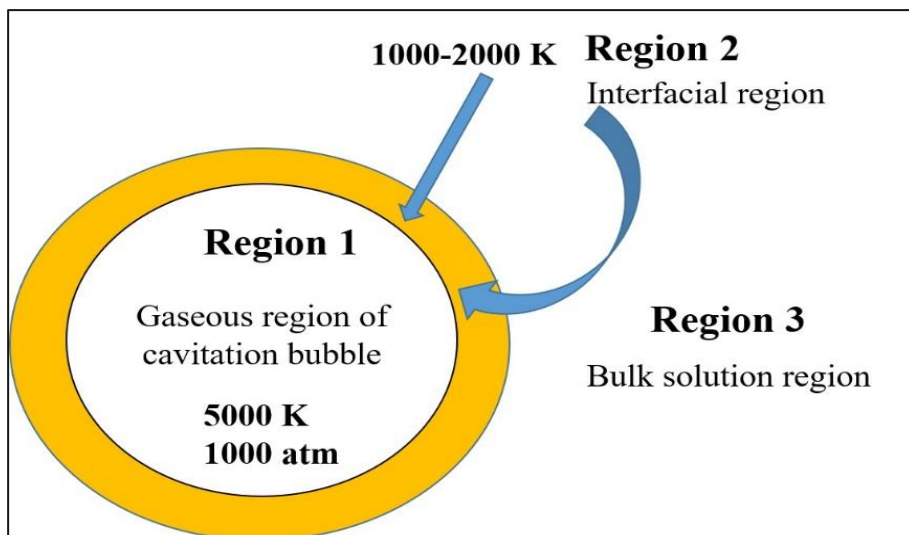
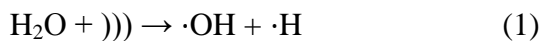
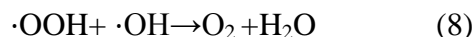


Figure 1. Three Reaction Region in the Liquid Solution as a Result of Ultrasonic Irradiation (Yap et al., 2019)

This much the high temperature and pressure, thermal decomposition transforms water molecules and oxygen into highly reactive radical species such as $\bullet\text{H}$ and $\bullet\text{OH}$ (Region 1) (Eren, 2012). It is increases sonochemical degradation by pyrolysis or radical attack upon explosions formed by acoustic cavitation (Mahvi, 2009). The second region is the interface region between the gaseous or vapor phase in the cavitation bubble and the liquid phase bulk solution (Region 2). The temperature in region 2 is usually in the range of 1000–2000 K, is lower than region 1 (Gielen et al., 2016; Yap et al., 2019). This temperature difference to direct the diffusion of the radical species between region 1 and region 2 from region 1 to region 2. As a result, the following sonochemical reactions takes happen in the region 2 (Equation. (1-5)) (Mahvi, 2009).



The third zone is the ambient temperature of the bulk solution (Region 3). Under ambient temperature (Zone 3) pyrolysis does not occur, but only radical attack can occur. It has been reported that only about 10% of the radicals generated from the interface region (Region 2) will diffuse or escape into region 3 (Yap et al., 2019). Other than that, unreacted radicals can recombine and release in the region 2 as presented in the equations below (Equation. (6-9)) (Pang et al., 2011; Yap et al., 2019).



The effect of the ultrasound waves on chemical reactions is very high. Ultrasound waves increase the speed of the chemical reaction. It provides free radical formation and acts as a catalyst. As a result of the mechanical effect of the ultrasound waves, it increases the surface area of the catalyst, accelerates mass transfer and prevents the formation of by products (Suslick, 1990). Ultrasound waves can change the conditions of the reaction, which takes place at the high

temperature and pressure and enable it to take place under suitable conditions (Okitsu et al., 2005).

2. PRINCIPLES OF THE SONOCHEMICALLY ASSISTED ADVANCED OXIDATION PROCESSES

2.1. Sonolytic (US) and Sonocatalytic Processes (US/Catalyst)

Since ultrasound is used for the formation of reactive oxygen derivatives in the removal of organic pollutants in water in the sonolytic oxidation, the high and low concentration of the solution does not create any barrier (Guo et al., 2011). Ultrasonic wave is defined as a sound wave that has a frequency above normal hearing (Khanal et al., 2007). When ultrasound waves radiate in the medium of sludge and organic pollutants, a mechanism of compression and spacing of water molecules in the medium happens to provide energy to the liquid phase (Dewil et al., 2006). The first phase of the sonolytic oxidation process is where cavitation nuclei are produced from microbubbles trapped in the microslits of the particles suspended in the liquid. In the second phase, the bubbles grow and expand in a controlled way with the frequency of the sound wave applied to the cavitation nuclei (Ince and Tezcanlı 2001). When sound waves are given to water molecules, the molecules separate and approach. When the separation and approach limits of water molecules are high enough to separate them from each other, micro sized bubbles are created. These bubbles are named to acoustic cavitation (Gogate and Pandit, 2004). Acoustic bubbles reach critical sizes after a few cycles. The critical size of the bubbles is inversely proportional to the frequency.

The stable lifetime of the bubbles formed is less than 2 microseconds. They have lifetimes of less than 100 ns (Thompson and Doraiswamy, 1999).

The sonocatalytic oxidation process is the sonolytic oxidation using different catalysts. It is known that the removal efficiency is increased by adding different catalysts to sonolytic oxidation (Wang et al., 2007). By adding suitable amounts of catalyst the production of weak points in the liquid is provided to nucleate the cavitation bubbles. These points increase the rate of the production of bubbles and thus increase the amount of the radicals production (Ninomiya et al., 2014). However, in case of the excess solid particles in the solution it causes scattering of ultrasonic sound waves and negatively affects the efficiency of the sonochemical degradation reactions (Rokhina et al., 2009). In the sonocatalytic oxidation process, most of the reactions happen at the interface between the cavitation bubble and the solution (Pang et al., 2011).

In addition, near the solid surface in the sonocatalytic oxidation the bubbles formed at the points create shock waves and cause erosion on the solid surface. This erosion causes an increase in the reactive centers on the solid surface (Chen et al., 2007). However, the particle size of the large particles decreases with erosion and the surface properties change so it is not possible to use them repeatedly (Hartmann et al., 2008). Smaller size than bubbles formed as a result of the cavitation nanoparticles are more resistant to erosion and high amount of the reactive radicals are formed at their interfaces with

cavitation bubbles (Meng and Oh, 2011). However, another problem in the use of nano sized structures as a catalysis reveals the problem of the separation of nano sized catalysts from solution (Asakura et al., 2008). The suitable size of catalysis depends on the frequency of the ultrasound used. Therefore, studies in the literature mostly concentrates on the optimization of the suitable size, reactivity and reaction conditions (suitable amount of catalysis, temperature) (Li et al., 2008). As can be seen, developing suitable catalysts for the sonocatalytic oxidation process is a more difficult and relatively lesser studied subject than other wastewater removal methods (Zhang, 2012). The schematic mechanism of the sonocatalytic oxidation process is seen in Figure 2.

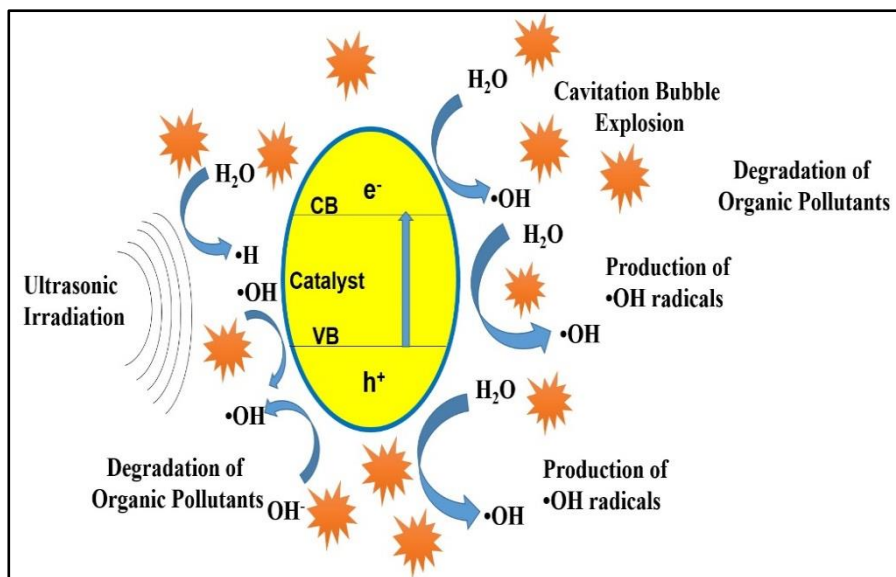
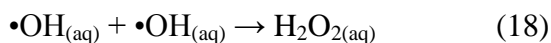
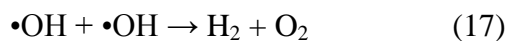
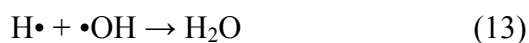
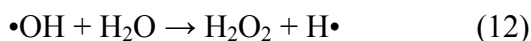
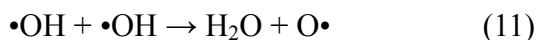
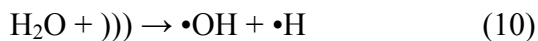


Figure 2. Diagrammatic mechanism of sonocatalytic oxidation process (Yap et al., 2019).

As can be seen from the equations as a result of the ultrasonic cavitation, oxygen atom, hydrogen atom, hydroxide, hydroperoxyl radicals and hydrogen peroxide are the formed (Equation. (10-21)).



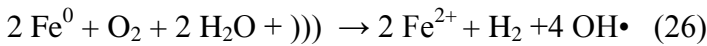
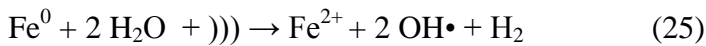
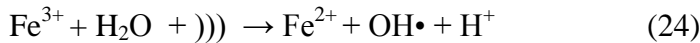
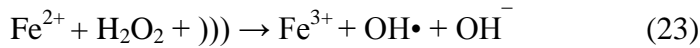
These radicals have low stability and high propensity to reaction. Radicals oxidize molecules by reaction with the organic molecules in the environment. The radicals formed can reaction on the surface of the bubble in the bubble and in the bulk liquid (Adewuyi, 2005).

2.2. Sono-Fenton Processes (US/H₂O₂/Fe²⁺/Fe³⁺)

When the sono-fenton (US/H₂O₂/Fe²⁺/Fe³⁺) process is applied for the degradation of the organic pollutants, a synergistic effect to appear between the fenton reagent and ultrasound and spontaneously degradation Fe-OOH²⁺ into Fe²⁺ and OOH• [Eqs. (22)] (Hou et al., 2016).



The Fe²⁺ ion can be reaction with H₂O₂ to form active radicals, thus establishing a cyclical mechanism (Li et al., 2012). The synergistic effect of Fenton's reagent with ultrasound not only increases the rate of Fe-OOH²⁺ to Fe²⁺ reaction, but also increases radical production by reactions between FeO/H₂O, Fe²⁺/H₂O₂ or Fe³⁺/H₂O [Eq. (23)-(26)] (Dindarsafa et al., 2017).



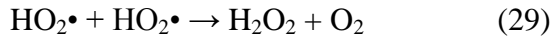
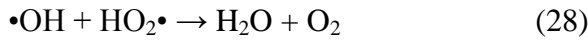
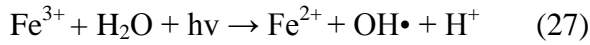
When the sono-fenton (US/H₂O₂/Fe²⁺/Fe³⁺) process is applied for the degradation of organic pollutants two events occur (Lau et al., 2002). More hydroxyl (OH•) radicals are formed, which reaction with organic pollutants and are oxidized than when ultrasound and fenton processes are applied alone. It can be said that the degradation

efficiency increases as a result of thermal division oxidation reactions in the ultrasonic cavitation bubbles (Khataee et al., 2017).

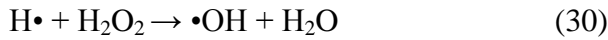
2.3. Sono-Photo-Fenton Processes (US/UV/H₂O₂/Fe²⁺/Fe³⁺)

The hybrid method combination ultrasound and ultraviolet radiation with the fenton process is known as the sono-photo-fenton process. In this hybrid process, the degradation of organic pollutants together with Fe (II) ions results in increased hydroxyl radical production in the aqueous solution (Inoue et al., 2006). Therefore, the use of the UV increases the amount of hydroxyl produced by converting the H₂O₂ produced by the recombination of hydroxyl radicals (Wu et al., 2001). Biggest problems with the use of the ultrasonic radiation is that it has low degradation in removing organic pollutants due to the recombination of the produced radicals (Adewuyi et al., 2001).

In the fenton process, the complex H₂O₂ formed by the reaction of Fe³⁺ ion can be reduced to Fe²⁺ ion as a result of sonolysis and photolysis reactions. Also, direct photolysis of H₂O₂ produces the hydroxyl radical (Ting et al., 2008). Radical production and reduction of Fe²⁺ ions are repeated periodically (Vaishnave et al., 2014). According to fenton, the sono-photo-fenton process requires a low amount of the iron salt. Therefore, it is of industrial importance as the amount of iron ions available for the sono-photo-fenton process is low in the purified water (Jorfi et al., 2018). The chemical reactions in the sono-photo-fenton hybrid process are as the follows [Eq. (27)-(31)].

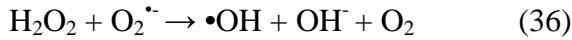
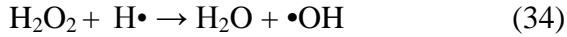
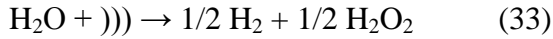


By using ultrasonic irradiation;



2.4. Sono-Photocatalytic Processes (US/UV/Catalyst)

Sonophotocatalytic is a hybrid sonolytic and photolytic process applied in the presence of a catalyst to increase the removal efficiency of the organic pollutants (Na et al., 2012). The sonophotocatalytic process includes advanced oxidation processes such as photolysis, photocatalysis, sonolysis, sonocatalysis and sonophotolysis. The main purpose of advanced oxidation processes is to reduce the removal cost of the industrial wastes and to transform organic wastes into harmless (Yap et al., 2019). To make the sonophotocatalytic process more efficient, there are three factors that effect mass transfer of the organic pollutants in the liquid phase. These factors are the catalyst surface, increased hydroxyl radical ($\cdot\text{OH}$) production, and the formation of cavitation bubbles in the presence of catalyst particles. (Khokhawala and Gogate, 2010). The chemical reactions occurring in the sonophotocatalytic processes are as given in the equations [Eq. (32)-(37)].

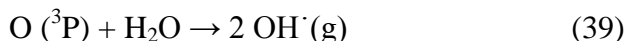
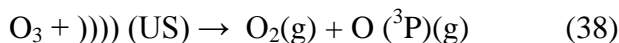


The sonolytic and photolytic process generates effective reactive radicals and then initiates reactions between free radicals and organic pollutants. Therefore, the hybrid combination of sonolytic and photocatalytic treatment is believed to provide a high degradation efficiency in the removal organic wastes (Jelic et al., 2013). The reason for this is that hydroxyl radical ($\bullet\text{OH}$) can be produced by the synergistic effect of the sonolytic and photolytic processes and more radicals are formed with the increase of the removal in the solution environment (Xu et al., 2013). The parameters by using the photolytic, sonolytic and sonophotolytic degradation process are the significantly affected are ultrasonic vibration power, ultrasonic frequency, ultraviolet light, wavelength, solution pH, addition of oxidizing agents, catalyst dosage (Yap et al., 2019).

2.5. Sonocatalytic-Ozonation Processes (US/Catalyst/O₃)

The sonocatalytic-ozonation process is an advanced oxidation process that occurs with the joint combination of ultrasonic radiation and hydroxyl radicals (Gogate and Pandit, 2004). Chemical reactions

occurring in the solution with the sonocatalytic-ozonation process [Eqs. (38-39)] (Hou et al., 2013).



Free radicals generated as a result of the sonocatalytic-ozonation process reactions can be diffuse throughout the solution to oxidize organic and inorganic pollutants. In the sonocatalytic-ozonation process, in the presence of ultrasound an energy region will be created in the direction of diffusion of the acoustic wave (Zhang et al., 2006). In addition, a larger surface area is the formed between the gaseous and liquid phases as a result of the formation of gas bubbles caused by ultrasonic radiation (Olson et al., 1994).

3. ENVIRONMENTAL APPLICATIONS OF THE SONOCHEMICALLY ASSISTED ADVANCED OXIDATION PROCESSES

Wastewater from the textile industry, which is given to the receiving environment without being treatment generally affects the appearance of the water and creates a bad image. In addition, wastewater has a toxic effect as well as negatively affecting the living life in lake and river waters (Ertugay and Acar, 2017). Due to the organic pollutants they contain, these wastewaters cause environmental problems by adversely affecting the light penetration and the amount of oxygen in the aquatic environment (Juang and Nguyen, 2013). Due to the complex chemical structures of the synthetic organic pigments in the

organic waste materials, they degradation slow against bacteriological decomposition (Midik, 2011). Wastewater with excessive pollution and toxicity, if it is not treatment with suitable methods it causes serious environmental problems. Accumulation of the organic wastes in the some aquatic organisms causes the formation of toxic and carcinogenic products (Socha, 1991).

Biological treatment of wastewater containing organic matter is the widely used to removal organic pollutants in the wastewater. However, these methods are used to removal industrial wastewaters containing toxic and non-biodegradable organic substances may not be sufficient for purification (Xu et al., 2004). Because of it is low efficiency, it is not preferred too much. Therefore, according to biological processes, physical and chemical methods are preferred (Zhang et al., 2005). Flocculation and activated carbon adsorption are used in the treatment of the wastewater containing organic matter. Excess sludge formation and regeneration of adsorbent have a negative effect on the use of these methods (Slokar and Marechal, 1998). Sonochemically assisted advanced oxidation processes have been preferred recently as they are effective in the oxidizing complex organic compounds that are difficult to biologically degradation into simple end products.

CONCLUSION

The presence of organic pollutants in the aquatic environment, even at low concentrations can cause hazardous water problems and environmental problems. Continuous disposal of the industrial wastes into the environment causes potentially harmful and negative effects on the environment and people. Sonochemically assisted advanced oxidation processes consist of the different hybrid processes. These hybrid processes are effective methods for the removal of the industrial wastewater and organic pollutants. Ultrasonic radiation create the basic of the sonochemistry. Ultrasonic radiation is convert into more effective processes with different hybrid techniques. These hybrid techniques; sonocatalytic, sono-photocatalytic, sono-fenton, sono-photo-fenton, sonocatalytic ozonation processes.

Ultrasonic radiation assisted hybrid processes are an oxidation method based on the production of the highly reactive species such as hydroxyl radicals ($\text{OH}\cdot$) and the reaction of organic pollutants. Hydroxyl radicals ($\text{OH}\cdot$) are molecules that return organic pollutants into harmless ones. Ultrasonic radiation assisted processes have many advantages according to other advanced oxidation processes. Ultrasonic radiation assisted processes are of the economic importance.

ACKNOWLEDGEMENTS

The authors would like to express special thanks to the University of Gumushane for supports.

REFERENCES

- Adewuyi, Y. G. (2005). Sonochemistry in environmental remediation. 1. Combinative and hybrid sono-photochemical oxidation processes for the treatment of pollutants in water. *Environmental Science Technology*, Vol. 39, pp 3409-3420.
- Adewuyi, Y. G. (2001). Sonochemistry: environmental science and engineering applications. *Industrial & Engineering Chemistry Research*, Vol. 40, pp 4681-4715.
- Akdağ Anıt, C. (2016). TiO₂ bazlı gözenekli mikrokürelerin yeni fotokatalitik proses uygulamaları. Yüksek Lisans Tezi, Hacettepe Üniversitesi, Fen Bilimleri Enstitüsü, Nanoteknoloji ve Nanotıp Ana bilimdalı, Ankara.
- Asakura, Y., Nishida, T., Matsuoka, T., Koda, S. (2008). Effects of ultrasonic frequency and liquid height on sonochemical efficiency of large-scale sonochemical reactors. *Ultrasonics Sonochemistry*, Vol. 15, No. 3, pp 244-250.
- Carlsen, L., Bruggemann, R., Sailaukhanuly, Y. (2013). Application of selected partial order tools to analyze fate and toxicity indicators of environmentally hazardous chemicals. *Ecological Indicators*, Vol. 29, pp 191-202.
- Chen, H., Liu, S., Wang, J., Chen, D. (2007). Study on effect of microparticle's size on cavitation erosion in solid-liquid system. *Journal of Applied Physics*, Vol. 101, No. 10, pp 103510-103515.
- Chong, M. N., Jin, B., Chow, C. W., Saint, C. (2010). Recent developments in photocatalytic water treatment technology: A review. *Water Research*, Vol. 44, No. 10, pp 2997-3027.
- Chu, K. H., Al-Hamadani, Y. A. J., Park, C. M., Lee, G., Jang, M., Jang, A., Her, N., Son, A., Yoon, Y. (2017). Ultrasonic treatment of endocrine disrupting compounds, pharmaceuticals and personal care products in water: A review. *Chemical Engineering Journal*, Vol. 327, pp 629-647.

- Clarke, E., Steinle, D. (1995). Health and environmental safety aspects of organic colorants. *Review of Progress in Coloration and Related Topics*, Vol. 25, No. 1, pp 1-5.
- Deveci, İ. (2015). Tekstil atık sularında bulunan boyar maddelerin sonokatalitik giderimi için SiO₂ nanopartikül temelli kataliz sistemlerinin geliştirilmesi. Doktora tezi, Fen Bilimleri Enstitüsü, Kimya Anabilim Dalı, Muğla Sıtkı Koçman Üniversitesi, Muğla.
- Dewil, R., Baeyens, J., Goutvrind, R. (2006). Ultrasonic treatment of waste activated sludge. *Environmental Progress*, Vol. 25, No. 2, pp 121-128.
- Dindarsafa, M., Khataee, A., Kaymak, B., Vahid, B., Karimi, A., Rahmani, A. (2017). Heterogeneous sono-fenton-like process using martite nanocatalyst prepared by high energy planetary ball milling for treatment of a textile dye. *Ultrasonics sonochemistry*, Vol. 34, pp 389-399.
- Eren, Z. (2012). Ultrasound as a basic and auxiliary process for dye remediation: a review. *Journal of Environmental Management*, Vol. 104, pp127-141.
- Ertugay, N., Acar, F. N., (2017). Removal of COD and color from Direct Blue 71 azo dye wastewater by Fenton's oxidation: Kinetic study. *Arabian Journal of Chemistry*, Vol. 10, pp 1158-1163.
- Gielen, B., Marchal, S., Jordens, J., Thomassen, L. C. J., Braeken, L., Van Gerven, T. (2016). Influence of dissolved gases on sonochemistry and sonoluminescence in a flow reactor. *Ultrasonics sonochemistry*, Vol. 31, pp 463-472.
- Gogate, P. R., Mujumdar, S., Thampi, J., Wilhelm, A. M., Pandit, A. B. (2004). Destruction of phenol using sonochemical reactors: scale up aspects and comparison of novel configuration with conventional reactors. *Separation and Purification Technology*, Vol. 34, No. 1-3, pp 25-34.
- Gogate, P. R., Pandit, A. B., (2004). A Review of Imperative Technologies for Wastewater Treatment II: Hybrid Methods. *Advances in Environmental Research*, Vol. 8, No. 3-4, pp 553-597.
- Guo, Y., Cheng, C., Wang, J., Wang, Z., Jin, X., Li, K., Gao, J. (2011). Detection of reactive oxygen species (ROS) generated by TiO₂(R), TiO₂(R/A) and

- TiO₂(A) under ultrasonic and solar light irradiation and application in degradation of organic dyes. *Journal of Hazardous Materials*, Vol. 192, No. 2, pp 786-793.
- Halliday, D., Resnick, Ri. (1992). *Fiziğin Temelleri-1*, (Çeviren: Prof. Dr. Cengiz Yalçın). Arkadaş Kitabevi, 3. Baskı.
- Hartmann, J., Bartels, P., Mau, U., Witter, M., Tümpling, W. V., Hofmann, J., Nietzsche, E. (2008). Degradation of the drug diclofenac in water by sonolysis in presence of catalysts. *Chemosphere*, Vol. 70, No. 3, pp 453-461.
- Hou, L., Wang, L., Royer, S., Zhang, H. (2016). Ultrasound-assisted heterogeneous fenton-like degradation of tetracycline over a magnetite catalyst. *Journal of Hazardous Materials*, Vol. 302, pp 458-467.
- Hou, L., Zhang, H., Wang, L., Chen, L., Xiong, Y., Xue, X. (2013). Removal of sulfamethoxazole from aqueous solution by sono-ozonation in the presence of a magnetic catalyst. *Separation and Purification Technology*, Vol. 117, pp 46-52.
- Ince, N., Tezcanlı, G., Belen, R., Apikyan, I. (2001). Ultrasound as a catalyzer of aqueous reaction systems: the state of the art and environmental applications. *Applied Catalysis B: Environmental*, Vol. 29, No. 3, pp 167-176.
- Ince, N. H., Tezcanlı, G. (2001). Reactive dyestuff degradation by combined sonolysis and ozonation. *Dyes and Pigments*, Vol. 49, pp 145-153.
- Inoue, M., Okada, F., Sakurai, A., Sakakibara, M. (2006). A new development of dyestuffs degradation system using ultrasound. *Ultrasonics Sonochemistry*, Vol. 13, pp 313-320.
- Jelic, A., Michael, I., Achilleos, A., Hapeshi, E., Lambropoulou, D., Perez, S., Petrovic, M., Fatta-Kassinos, D., Barcelo, D. (2013). Transformation products and reaction pathways of carbamazepine during photocatalytic and sonophotocatalytic treatment. *Journal of Hazardous Materials*, Vol. 263, pp 177-186.

- Jorfi, S., Pourfadakari, S., Kakavandi, B. (2018). A new approach in sonophotocatalytic degradation of recalcitrant textile wastewater using MgO@Zeolite nanostructure under UVA irradiation. *Chemical Engineering Journal*, Vol. 343, pp 95-107.
- Juang, R. S., Nguyen, T. A., (2013). Treatment of waters and wastewaters containing sulfur dyes: A review. *Chemical Engineering Journal*, Vol. 219, pp 109-117.
- Karaca, M., Kırınşan, M., Karaca, S., Khataee, A., Karimi, A. (2016). Sonocatalytic removal of naproxen by synthesized zinc oxide nanoparticles on montmorillonite. *Ultrasonics Sonochemistry*, Vol. 31, pp 250-256.
- Khataee, A., Kayan, B., Gholami, P., Kalderis, D., Akay, S. (2017). Sonocatalytic degradation of an anthraquinone dye using TiO₂-biochar nanocomposite. *Ultrasonics Sonochemistry*, Vol. 39, pp 120-128.
- Khanal, S. K., Grewell, D., Sung, S., Leeuwen, J. (2007). Ultrasound applications in wastewater sludge pretreatment: A Review. *Environmental Science and Technology*, Vol. 37, No. 4, pp 277-313.
- Khokhawala, I. M., Gogate, P. R. (2010). Degradation of phenol using a combination of ultrasonic and UV irradiations at pilot scale operation. *Ultrasonics Sonochemistry*, Vol. 17, pp 833-838.
- Lau, I. W., Wang, P., Chiu, S. S., Fang, H. H. (2002). Photoassisted fenton oxidation of refractory organics in UASB-pretreated leachate. *Journal of Environmental Sciences*, Vol. 14, No. 3, pp 388-392.
- Li, W., Nanaboina, V., Zhou, Q., Korshin, G.V. (2012). Effects of fenton treatment on the properties of effluent organic matter and their relationships with the degradation of pharmaceuticals and personal care products. *Water Research*, Vol. 46, pp 403-412.
- Li, M., Li, J. T., Sun, H. W. (2008). Decolorizing of azo dye reactive red 24 aqueous solution using exfoliated graphite and H₂O₂ under ultrasound irradiation. *Ultrasonics Sonochemistry*, Vol. 15, No. 5, pp 717-723.
- Mahvi, A.H. (2009). Application of ultrasonic technology for water and wastewater treatment. *Iranian Journal of Public Health*, Vol. 38, No. 2, pp 1-17.

- Mamadiev, M., Yılmaz, G. (2011). Treatment and recycling facilities of highly polluted water-based paint wastewater. *Desalination and Water Treatment*, Vol. 26, pp 66-71.
- Meng, Z. D., Oh, W. C. (2011). Sonocatalytic degradation and catalytic activities for MB solution of Fe treated fullerene/TiO₂ composite with different ultrasonic intensity. *Ultrasonics Sonochemistry*, Vol. 18, No. 3, pp 757-764.
- Mıdık, F. (2011). Reaktif Sarı 145 Azo Boyar Maddesinin ve 2,4-Diklorofenoksiasetik Asit Pestisitinin Yüksüz Nano Demir, Fenton ve Foto-Fenton Prosesleri ile Karşılaştırılmalı Giderilmesi. Yüksek Lisans Tezi, Çukurova Üniversitesi, Fen Bilimleri Enstitüsü, Adana.
- Na, S., Jinhua, C., Cui, M., Khim, J. (2012). Sonophotolytic diethyl phthalate (DEP) degradation with UVC or VUV irradiation. *Ultrasonics Sonochemistry*, Vol. 19, pp 1094-1098.
- Ninomiya, K., Noda, K., Ogino, C., Kuroda, S., Shimizu, N. (2014). Enhanced OH radical generation by dual-frequency ultrasound with TiO₂ nanoparticles: Its application to targeted sonodynamic therapy. *Ultrasonics Sonochemistry*, Vol. 21, pp 289-294.
- Okitsu, K., Iwasaki, K., Yobiko, Y., Bandow, H., Nishimura, R., Maeda, Y. (2005). Sonochemical degradation of azo dyes in aqueous solution: a new heterogeneous kinetics model taking into account the local concentration of OH radicals and azo dyes. *Ultrasonics Sonochemistry*, Vol. 12, pp 255-262.
- Olson, T. M., Barbier, P. F. (1994). Oxidation kinetics of natural organic matter by sonolysis and ozone, *Water Research*, Vol. 28, pp 1383-1391.
- Pang, Y. L., Bhatia, S., Abdullah, A. Z. (2011). Process behavior of TiO₂ nanotube-enhanced sonocatalytic degradation of Rhodamine B in aqueous solution. *Separation and Purification Technology*, Vol. 77, pp 331-338,
- Papadaki, M. (2004). Sonocatalytic oxidation processes for the removal of contaminants containing aromatic rings from aqueous effluents, *Separation and Purification Technology*, Vol. 34, No. 1-3, pp 35-42.

- Rokhina, E. V., Lahtinen, M., Nolte, M. C. M., Virkutyte, J. (2009). The influence of ultrasound on the RuI₃-catalyzed oxidation of phenol: Catalyst study and experimental design. *Applied Catalysis B: Environmental*, Vol. 87, No. 3-4, 162-170.
- Sanghi, R., Bhattacharya, B., Singh, V., (2002). Cassia angustifolia seed gum as an effective natural coagulant for decolourisation of dye solutions. *Green Chemistry*, Vol. 4, No. 3, pp 252-254.
- Slokar, Y. M., Marechal, A. M. (1998). Methods Of Decoloration Of Textile Wastewaters. *Dyes and Pigments*, Vol. 37, No. 4, pp 335-356.
- Socha, K. (1991). Treatment of Textile Effluents. *Textile Month*, Vol. 12, pp 52-56.
- Suslick, K. S. (1990). Sonochemistry. *American Association for the Advancement of Science*, Vol. 247, No. 49, pp 1439-1445.
- Thompson, L. H., Doraiswamy, L. K. (1999). Sonochemistry: science and engineering. *Ind. Eng. Chem. Res.*, Vol. 38, pp 1215-1249.
- Ting, W. P., Lu, M. C., Huang, Y. H. (2008). The reactor design and comparison of Fenton, electro-Fenton and photoelectro-Fenton processes for mineralization of benzene sulfonic acid (BSA). *Journal of Hazardous Materials*, Vol. 156, pp 421-427.
- Uğurlu, M. (2002). Uçucu kül kullanılarak kâğıt fabrikası atık sularında fenol ve lignin giderimi. *Sakarya Üniversitesi Fen Bilimleri Enstitüsü Dergisi*, Vol. 6, No. 3, pp 84-87.
- Vaishnave, P., Kumar, A., Ameta, R., Punjabi, P., Ameta, S.C. (2014). Photo oxidative degradation of azure-B by sono-photo-Fenton and photo-Fenton reagents. *Arabian Journal of Chemistry*, Vol. 7, pp 981-985.
- Walker, G., Hansen, L., Hanna, J. A., Allen, S. (2003). Kinetics of a reactive dye adsorption onto dolomitic sorbents. *Water Research*, Vol. 37, No. 9, pp 2081-2089.
- Wang, J., Jiang, Y., Zhang, Z., Zhang, X., Ma, T., Zhang, G., Li, Y. (2007). Investigation on the sonocatalytic degradation of acid red B in the presence of nanometer TiO₂ catalysts and comparison of catalytic activities of

- anatase and rutile TiO₂ powders. *Ultrasonics Sonochemistry*, Vol. 14, No. 5, pp 545-551.
- Wu, C., Liu, X., Wei, D., Fan, J., Wang, L. (2001). Photosonochemical degradation of phenol in water. *Water Research*, Vol. 35, pp 3927-3933.
- Xu, L. J., Chu, W., Graham, N. (2013). Sonophotolytic degradation of dimethyl phthalate without catalyst: Analysis of the synergistic effect and modeling. *Water Research*, Vol. 47, pp 1996-2004.
- Xu, X. R., Li, H. B., Wang, W. H., Gu, J. D. (2004). Degradation of dyes in aqueous solutions by the Fenton process. *Chemosphere*, Vol. 57, pp 595-600.
- Yap, H. C., Pang, Y. L., Lim, S., Abdullah, A. Z., Ong, H. C., Wu, C.H. (2019). A comprehensive review on state-of-the-art photo-, sono-, and sonophotocatalytic treatments to degrade emerging contaminants. *International Journal of Environmental Science and Technology*, Vol. 16, pp 601-628.
- Zhang, H., Duan, L. J., Zhang, D. B. (2006). Decolorization of methyl orange by ozonation in combination with ultrasonic irradiation. *Journal of Hazardous Materials*, Vol. 138, pp 53-59.
- Zhang, S. (2012). Synergistic effects of C-Cr codoping in TiO₂ and enhanced sonocatalytic activity under ultrasonic irradiation. *Ultrasonics Sonochemistry*, Vol. 19, No. 4, pp 767-771.
- Zhang, H., Duan, L., Zhang, Y., Wu, F. (2005). The use of ultrasound to enhance the decolorization of the C.I. Acid Orange 7 by zero-valent iron. *Dyes and Pigments*, Vol. 65 pp 39-43.

CHAPTER 5

FUNDAMENTALS OF OPHTHALMIC LENS DECENTRATION

Assoc. Prof. Dr. Tuba ÖZDEMİR ÖGE¹
Asst. Prof. Dr. Firdevs Banu ÖZDEMİR²
Res. Asst. Dr. Mecit ÖGE³
Inst. Okan ÇİÇEK⁴

¹Bartın University, Vocational School of Health Services, Department of Medical Services and Techniques, Opticianry Program, Bartın, Turkey. E-mail: tozdemir@bartin.edu.tr, ORCID ID, <https://orcid.org/0000-0001-6690-7199>.

²Beykent University Vocational School, Department of Medical Services and Techniques, Radiotherapy Program, Istanbul, Turkey; E-mail: firdevsbanuozdemir@beykent.edu.tr, ORCID ID, <https://orcid.org/0000-0002-7935-2062>.

³Bartın University, Faculty of Engineering, Architecture and Design, Department of Mechanical Engineering, Bartın, Turkey; E-mail: mecitoge@bartin.edu.tr, ORCID ID, <https://orcid.org/0000-0001-5243-0828>.

⁴Altınbaş University, Vocational School of Health Services, Department of Medical Services and Techniques, Opticianry Program, Istanbul. E-mail: okancicek91@gmail.com, ORCID ID, <https://orcid.org/0000-0002-4335-8286>.

INTRODUCTION

Ophthalmic optical lenses used in the field of health and in the correction of eye disorders are "eyeglasses", "contact lenses", "intraocular lenses", "filters" and "low vision devices". Spectacle lens is one of the ophthalmic optic lenses used in the correction of myopia, hypermetropia, astigmatism and presbyopia refractive errors. Decentration is horizontal and/or vertical displacement of the point of centration of a spectacle lens from its standard optical center. The amount of lens decentration corresponds to the difference between the patient's PD (pupillary distance) and the frame's PD. For a lens to induce no prismatic effect, its optical center should coincide with the pupil, otherwise prismatic effect will arise. The power of the prism varies with the amount of lens decentration, and the refractive power of the lens as explained in Prentice Rule. Husna and Yulianti explained the lens decentration of spectacle wearers (Husna and Yulianti. 2019). In their study, Arshad et al. investigated the percentage of decentered spectacles among other samples, the effect of decentration on lenses' stereoacuity, the difference between optical centration distance (OCD) and interpupillary distance (PD) (Arshad et al. 2017). El-Nimri and Walline studied the centration and decentration of contact lenses during peripheral gaze (El-Nimri and Walline. 2017). Churk-yan Tang investigated the spherical lens decentration errors by Prentice's rule (Tang. 1989).

The Boxing System

The boxing system was initially adopted by the Optical Manufacturers Association in 1962 to establish a frame and lens measurement standard which is an improved version of the previously adopted systems (Laramy-K Optical. 2021). It is based on the imaginary wrapping of the frame with horizontal and vertical lines. This eyeglass measurement system involves the datum line of the frame, the center of the right lens, the center of the left lens, the length of the lens, the datum center length, the distance between the lenses, the distance between the rims, and the minimum distance between the lenses as shown in Figure 1 (Aksak and Küçüker. 2005).

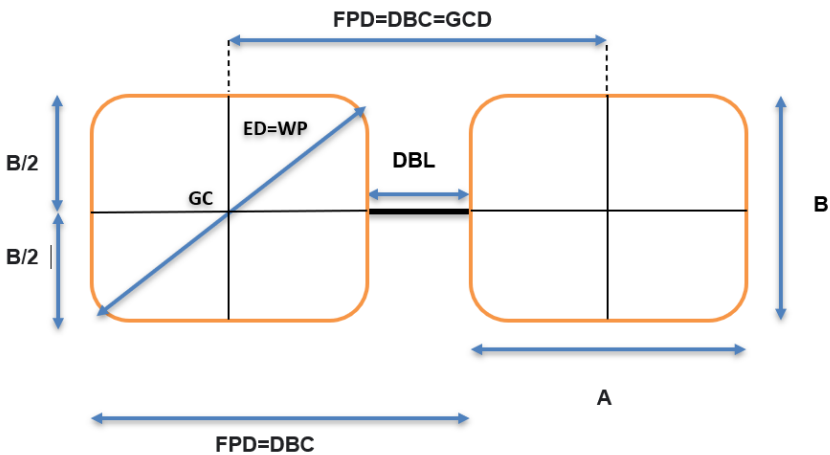


Figure 1. Boxing System

In Figure 1, “A” (eye size) is the horizontal width of the rectangle between the vertical lines. “B” is the vertical distance from the highest point to the lowest point of the eye ring. The distance between lenses (DBL) is the horizontal width between the right lens and the left lens

at the narrowest point of the bridge. Geometric center (GC) is the intersection of the datum line and horizontal centers of each lens. Effective diameter (ED) equals to twice the distance between the geometric center and the farthest edge of the lens. It is used to find the required uncut lens size (Aksak and Küçüker. 2005).

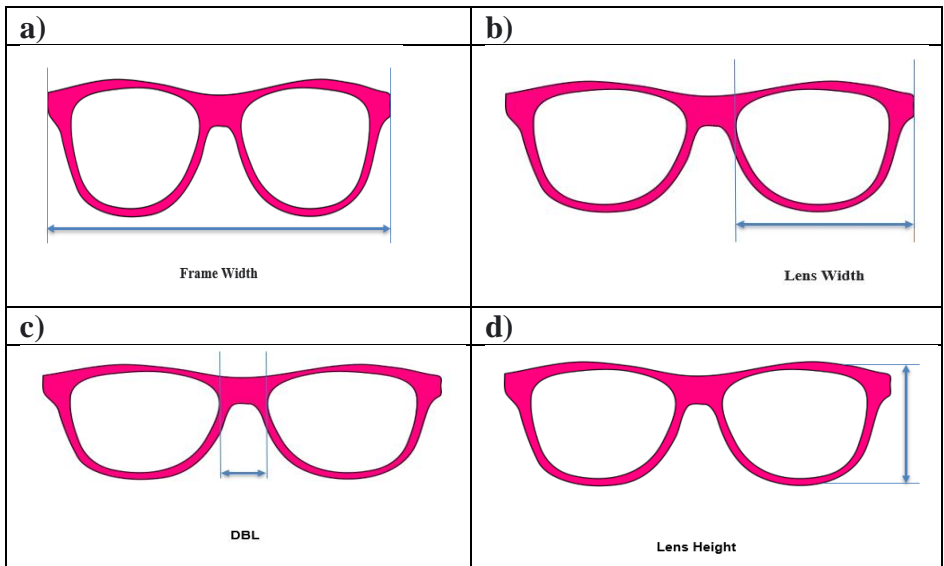


Figure 2. Frame measurements

The frame model used in Figures 2, 4, 6 and 7 was acquired from Ref (Eye Frame. 2021). Frame size measurements (Figure 3) are always given in millimeters. Lens width (eye size) is the horizontal width of one of your frame's lenses. Frame width (Figure 2a) is the total horizontal length of the frame. The lens width (eye size) is the distance between the nasal edge point of the lens and the farthest point of the frame for the same lens (Figure 2b). The lens width for most

frames usually ranges from 40 mm to 62 mm. Bridge Size (DBL) is the distance between the nasal edge points of the two lenses and it typically ranges between 14 mm and 24 mm (Figure 2c). Lens height (Figure 2d) is the vertical distance between the two edge points of a lens excluding the frame. Temple (arm size) is measured along the length of the temple (Figure 3). The frame sizes are generally stamped on the inside of the one of the temples of the frame as shown in Figure 3. As shown in Figure 3, the numbers indicate the arm length, that is the length of the temple; the bridge width (DBL), that is the distance between the lenses; and the lens diameter, respectively.

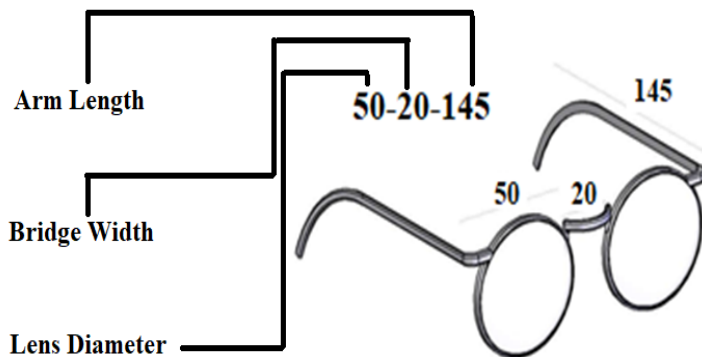


Figure 3. Frame size chart

Frame Pupillary Distance (FPD)

“Frame PD” is an important parameter used in frame selection. Frame PD should always be lower than the patient’s actual PD due to aesthetical and optometric considerations, such that, the patient’s

temporal field of view can be reduced when the patient's PD exceeds the frame PD. The geometric center distance (GCD), referred to as the frame pupillary distance (FPD) and distance between centers (DBC), is the distance between the two geometric centers of the lenses. The geometric center distance or the frame PD can be calculated by simply adding the eye size (A) to the distance between lenses" (DBL). An illustration of frame pupillary distance (FPD) is shown in Figure 4. Frame pupillometer is used to measure the pupil of the frame as given in Figure 5.

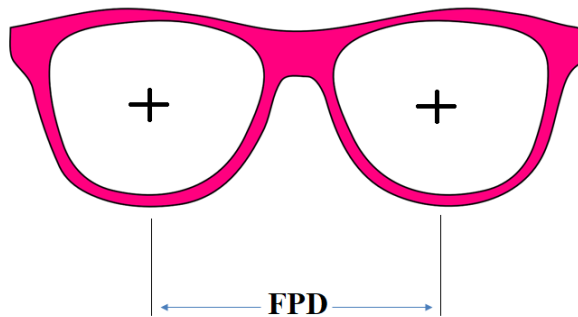


Figure 4. Frame pupillary distance (FPD)



Figure 5. Frame pupillometer

Patient's Pupillary Distance

Patient's pupillary distance (PD) is the distance between the centers of the pupils of the two eyes. There are two types of pupillary distance measurements called as monocular PD and binocular PD. This measurement differs from person to person and depends on whether they are looking at close objects or far away. In general, the distance between the two pupils varies between 48 mm and 73 mm. Pupillary distance can be measured with the ophthalmic ruler, which is the simplest pupillometer, as well as with an automatic digital pupillometer. The pupillary distance is an essential measurement while dispensing a new pair of eyeglasses. A patient's PD number is written by the doctor in the PD section on her/his eyeglass prescription. The optical center of each lens should be aligned in front of the center of the patient's pupil for correct and clear vision (Figure 6) (Özdemir Öge. 2020).

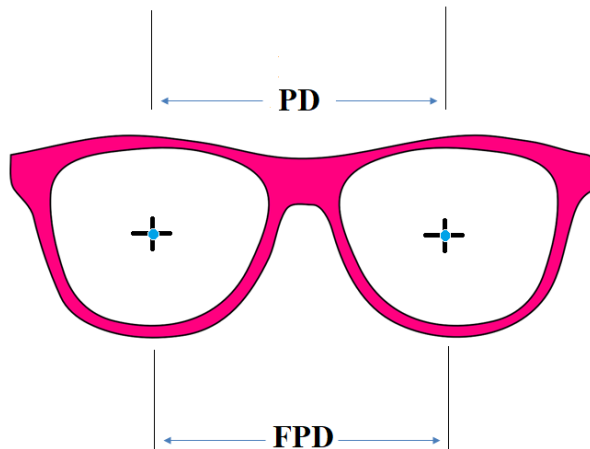


Figure 6. Frame pupillary distance (FPD) and pupillary distance of patient (PD)

Minimum Blank Size

Minimum blank size (MBS) can be defined as the lens blank with the smallest dimension that can be used for a given lens prescription and frame combination. The minimum blank size for each lens is determined using Equation 1. The last term in the MBS equation is “+ 2 mm.” which is considered as a slightly excess amount of lens dimension intended for compensation of possible manufacturing defects that may arise on the lens edge. Here is an example of how to figure out the MBS for finished single vision lenses (Brooks and Borish. 2007).

$$MBS = ED + 2 \times (\text{amount of decentration}) + 2 \text{ mm} \quad (1)$$

where MBS is the minimum blank size, ED is the effective diameter of the frame with a given shape that is the distance between the geometrical center of the lens and the farthest edge of the same lens. The illustration of minimum blank size on an imaginary frame is shown in Figure 7. In the figure “d” is the decentration amount, and ED is the effective distance. An example of insufficient blank size is shown in Figure 7.

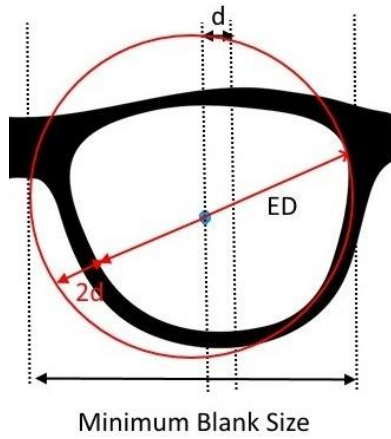


Figure 7. Illustration of minimum blank size (MBS).

A diameter control echelle (as illustrated in Figure 8) is used to determine a standard lens size after the MBS is determined.

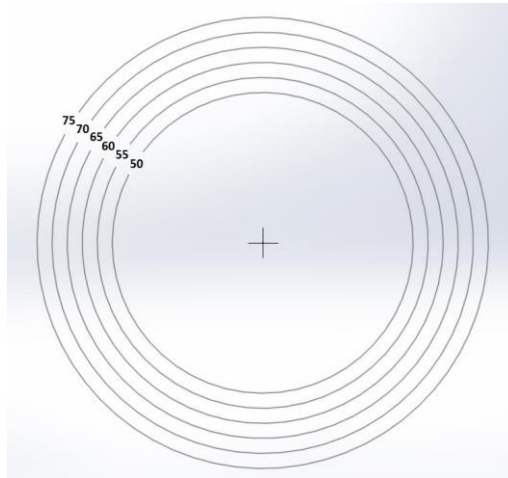


Figure 8. Diameter control echelle

Decentration

Decentration is the process of displacement of the optical center of lenses from the geometric center according to the frame dimensions and the PD distance of the patient. After the measurements by use of a lensometer, the optical lens is marked as shown in Figure 9.



Figure 9. Marking of optical lenses after determination of dioptric powers in a lensometer

During the decentration process, if a cylindrical value is included in the prescription, it should be ensured that the dots are aligned in horizontal direction as shown in Figure 10.

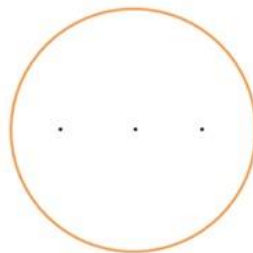


Figure 10. Horizontally aligned markings on a lens

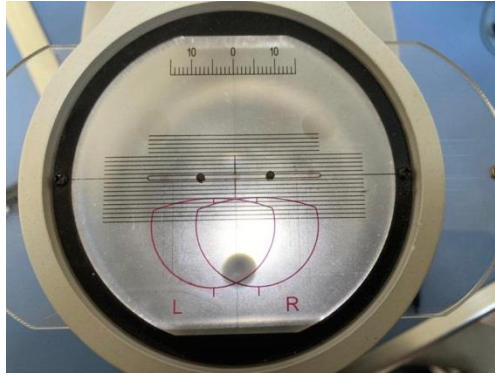


Figure 11. The condition of the eyeglasses before it is decentered in the optical lens centering device

After the decentration process shown in Figure 11, a suction cup attached to the optical centering device is used to fix the lens for the edging operation.

For the case of symmetrical right and left PD, where the monocular right eye PD equals to the monocular left eye PD, the decentration amount for each lens is the difference between the frame PD and the patient's PD, divided by 2, as shown in Equation 2, and the total decentration is the difference between the frame PD and the patient's PD, as shown in Equation 3.

$$\text{Decentration per lens} = \frac{(A+DBL)-PD}{2} \quad (2)$$

$$\text{Total Decentration} = (A + DBL) - PD \quad (3)$$

The GCD is also referred to as distance between centers (DBC), frame center distance and frame PD (Brooks and Borish. 2007).

In most cases where the patient's monocular right and left PDs are different, the amount of decentration is calculated separately for left and right eyes. In this case the amount of decentration is calculated by the following Equation 4.

$$\text{Decentration per lens} = \frac{(A+DBL)}{2} - \text{MonocularPD} \quad (4)$$

Improper lens placement results in induced prismatic effect the extent of which depends on the dioptric power of the lens (F) and the amount of displacement of the optical center (OC) in cm, which is stated by the following Prentice's Rule (Equation 5):

$$\Delta = cF \quad (5)$$

where Δ is the prismatic effect induced by incorrect displacement, c is the distance from the optical center (OC), and F is the dioptric power of the lens (Brooks and Borish. 2007).

When vertical decentration is required during the dispensing process of any given lens, Equation 6 is applied.

$$\text{Vertical decentration} = \text{OC height} - \frac{B}{2} \quad (6)$$

where B is the lens height as shown in Figure 2d.

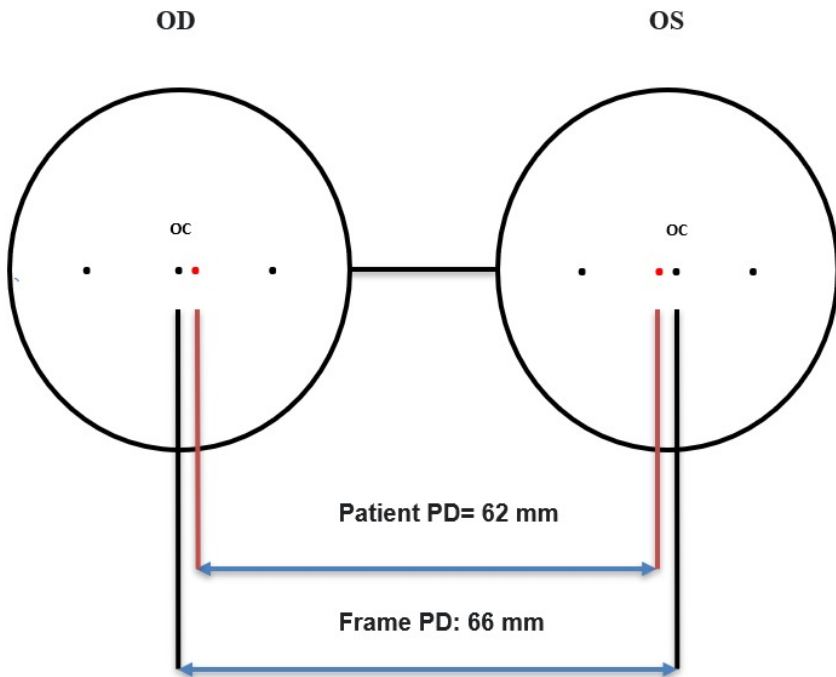


Figure 12. Horizontal decentration

In an exemplary prescription, A is given as 50 mm, DBL is given as 16 mm and Patient PD is given as 62 mm as shown in Figure 12.

In this example, frame PD equals to $A + DBL = 66$ mm.

Frame PD - Patient PD = 66 mm - 62 mm = 4 mm / 2 = 2 mm.

The decentration per each lens is 2 mm.

As the patients PD (62 mm) is less than the frame PD (66 mm), inward decentration should be applied (towards nasal direction).

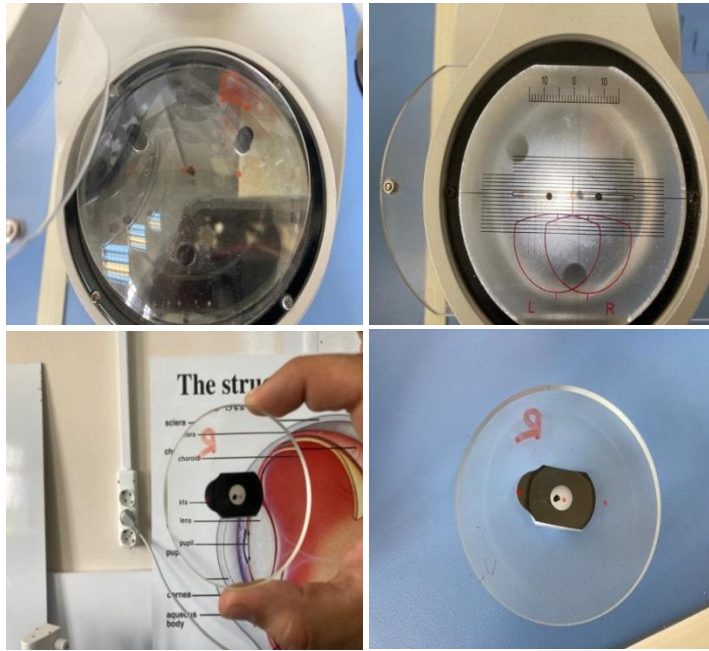


Figure 13. 2 mm nasal (inward) decentralized right lens

After the amount of decentration is determined using the formula for horizontal decentration, the lens is placed on the optical lens centering device, the required decentration is applied using the ruler that is mount onto the device with 1 mm intervals, and afterwards the lens is blocked in the decentered position. Figure 13 shows the horizontal decentration steps for the right lens, Figure 14 shows the horizontal decentration steps for the left lens, and Figure 15 shows 2 mm decentered right and left lenses.

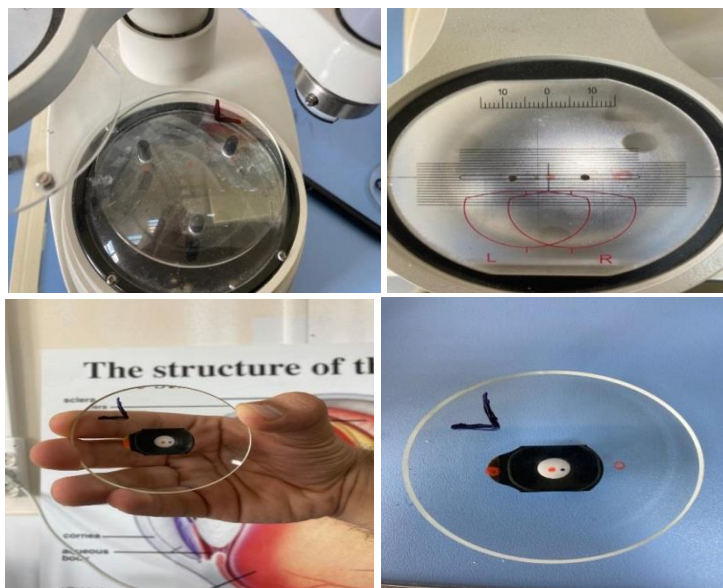


Figure 14. 2 mm nasal (inward) decentralized left lens

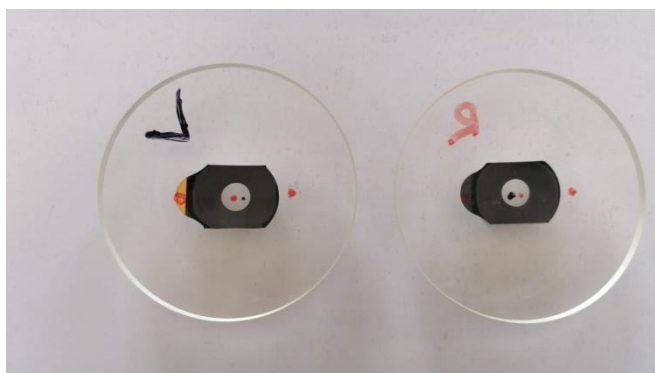


Figure 15. 2 mm horizontal decentralization of right and left lenses

As shown in Figure 15, the optical centers of both lenses were displaced 2 mm towards nasal direction due to the difference in the pupillary distance of patient with that of the frame.

Vertical Decentration and Blocking

In another exemplary prescription, in addition to the information required for horizontal decentration, B is measured as 42 mm (as shown in Figure 16), and OC height is given as 23 mm.



Figure 16. Measurement of lens height with a ruler (B).

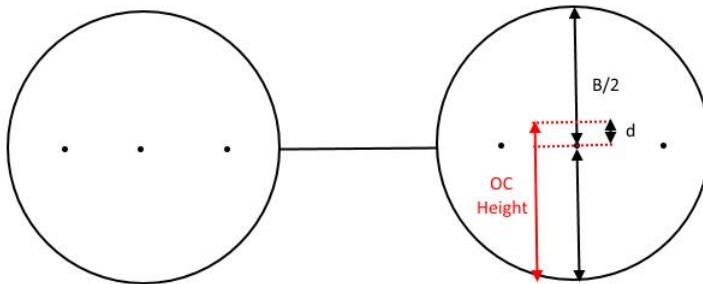


Figure 17. Illustration of vertical decentration

In this example the amount of vertical decentration to be applied can be calculated as:

$$\text{OC Height} - B/2 = d \text{ (vertical decentration).}$$

where B is the lens height and d is the amount of vertical decentration (Figure 17).

Thus, the result would be $23 - (42/2) = 23 - 21 = 2$ mm.

After the amount of vertical decentration is calculated, the lens is placed on the optical lens centering device, positioned in accordance with the calculated decentration (Figure 18) and blocked accordingly before being edged in the lens edging machine. The vertically decentered lens is shown in Figure 19.

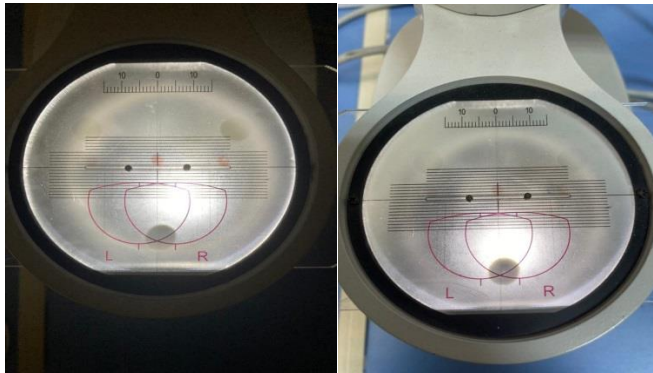


Figure 18. 2 mm vertical (upward) decentration of the lens in the optical lens centering device.

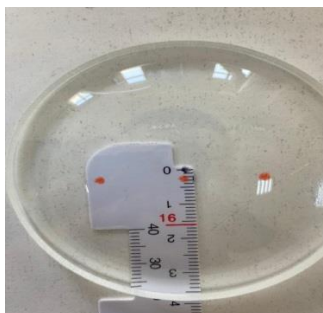


Figure 19. 2 mm vertically decentered lens

CONCLUSION

Proper fitting and dispensing of ophthalmic optical lenses play an important role in the ophthalmological practice and studies. During the fitting and dispensing of ophthalmic optical lenses, accurate determination of minimum blank size, pupillary distance, and the amount of decentration to be applied hold great importance since centering errors cause undesired prismatic effects and impair the image quality. Decentration is performed to protect the eye from unwanted prismatic effects caused by centering errors, or to provide the desired prismatic effect. In this article, concepts, and processes such as pupillary distance, minimum blank size, boxing method, Prentice Rule, decentration and the related calculations are explained to provide fundamental information about lens decentration which can be considered as an important step of dispensing of optical lenses.

REFERENCES

- Aksak, E., Küçüker, T. (2005), Gözlükçülük. Tüm Optik ve Optometrik Meslekler Birliği Derneği. İstanbul: Esen Ofset Matbaacılık San. ve Tic. A.Ş.
- Arshad, A., Choudhry, A.A., Hussain, S.J., Latif, I., Kalasra, A. (2017). Effect of Spectacle Centration on Stereoacuity., Journal of Rawalpindi Medical College (JRMC); 21(2): 117-121.
- Boxing system, Laramy-K Optical,
<https://www.laramyk.com/resources/education/dispensing/boxing-system/>.
Accessed 20.07.2021.
- Brooks, C.W., Borish, I. M. (2007) System for Ophthalmic Dispensing, Third Edition, Oxford: Butterworth-Heinemann.
- El-Nimri, N. W., Walline, J.J. (2017). Centration and Decentration of Contact Lenses during Peripheral Gaze., Optom Vis Sci. Nov; 94(11):1029-1035. doi: 10.1097/OPX.0000000000001127.
- Eye Frame, https://cdn.pixabay.com/photo/2014/04/02/11/17/glasses-305825_1280.png. Accessed 20.07.2021.
- Husna H. H., Yuliant, A. M.,(2019). Lens Decentration of Spectacle Wearers., AIP Conference Proceedings 2202, 020019.
- Özdemir Öge, T. (2020). Ophthalmic Optics Lenses, Fitting Applications And Dispensing Optical Prescription: A Review of Opticianry, Theory and Research in Health Sciences II, Volume 1, Birinci Basım / First Edition, Aralık.
- Tang, Chur-yan. (1989). Spherical lens decentration errors by Prentice's rule., Ophthal. Physiol. Opt., Vol. 9, January.

CHAPTER 6

ELECTRONIC STRUCTURE PROPERTIES OF BSb/Ga₂SSe HETEROSTRUCTURE UNDER ELECTRIC FIELD EFFECT

H. Eslem GULER¹ & Rabia CAGLAYAN² &

Prof. Dr. Mehmet KABAK³ & Assoc. Prof. Dr. Yesim MOGULKOC⁴

¹ Ankara University, Faculty of Science Department of Physics, Ankara, Turkey, h.eslemguler@gmail.com. ORCID: 0000-0003-4166-3217

² Ankara University, Faculty of Engineering, Department of Physics Engineering, Ankara, Turkey, rcaglayan@ankara.edu.tr. ORCID: 0000-0002-4373-064X

³ Ankara University, Faculty of Engineering, Department of Physics Engineering, Ankara, Turkey, mkabak@ankara.edu.tr. ORCID: 0000-0001-6097-9394

⁴ Ankara University, Faculty of Engineering, Department of Physics Engineering, Ankara, Turkey, mogulkoc@eng.ankara.edu.tr. ORCID: 0000-0002-7502-1522

INTRODUCTION

With the isolation of graphene, two-dimensional (2D) materials became an important research area (Novoselov, 2004; Geim et al., 2007; Castro et al., 2009). 2D materials have been accepted as a new generation of advanced functional materials, with many materials similar to graphene being studied extensively (Miró et al., 2014; Butler et al., 2013; Koski et al., 2013).

With improved techniques, these two-dimensional materials have been used in different application areas. Therefore, many approaches such as adsorption (Zhu et al., 2017), strain engineering (Hu et al., 2015), doping (Guo et al., 2020), and heterostructures (Long et al., 2016) have been tried by researchers to enhance the physical properties of materials. Among these approaches, heterostructures allow changing some of their physical properties while maintaining some properties of the component materials. Shang et al. (Shang et al., 2018) have shown that the InSe/InTe heterostructure is very suitable since optoelectronic applications owing to its tunable electronic properties.

In recent years, Janus structures, created by distinct elemental functionalization of the lower and upper sides of the material, have attracted attention with their geometric structures and unique features (Lu et al., 2017; Palsgaard et al., 2018; Riis-Jensen et al., 2019). The most outstanding feature in Janus structures is broken out-of-plane symmetry, which leads to out-of-plane electrical polarizations concerning central metal atoms. Among these materials, two-

dimensional (2D) Janus transition metal dichalcogenides (TMD) have attracted increasing attention due to their interesting physical and chemical properties as well as electronic properties such as indirect or direct bandgap transition (Radisavljevic et al., 2011).

Recently phosphorene, arsenene, and antimonene have been intensively investigated due to their interesting properties (Liu et al., 2014; Zhu et al., 2014; Hu et al., 2017; Zhang et al., 2015a; Zhang et al., 2015b; Ji et al., 2016; Wang et al., 2017; Zhang et al., 2018; Zhou et al., 2018; Xie et al., 2017). In particular, 2D BX (X = P, As, Sb) single layers composed of Group-VA derivatives have direct bandgaps (E_g) and high carrier mobilities (Xie et al., 2016).

In this study, we have explored BSb/Ga₂SSe the structural stability and electronic structure properties under the electric field. Although 2D Janus Ga₂SSe has not been experimentally synthesized and their applications in various fields have not been determined, calculations to examine their structural, electronic, and optical properties will facilitate their application areas. The energy band is one of the important properties of electronic materials related to two-dimensional electronic applications. Therefore, replacing electronic structures is valuable. Therefore, new two-dimensional (2D) configurations should be explored to enrich the various properties of materials. In this work, we expect it to stimulate theoretical and experimental efforts for the Janus heterobilayer BSb/Ga₂SSe synthesis and introduce new chemical and physical properties in the design of novel 2D materials.

1. COMPUTATIONAL METHOD

All density functional theory (DFT) calculations based on pseudo-atomic localized basis function had been performed using OpenMX3.9 package (Lee et al., 2019). The Perdew-Burke-Ernzerhof approach from the generalized gradient approximation (PBE-GGA) (Perdew, 1996) was applied to define the exchange-correlation functional and the norm-conserving pseudopotentials (Ozaki et al. 2003, 2004, 2005). The Brillouin zone integration was performed with $17 \times 17 \times 1$ k-point mesh using the Monkhorst-Pack method (Monkhorst et al., 1976). The energy cutoff was set to be 300 Ry. A vacuum space of 25 Å was used in the direction perpendicular to the sheet to avoid the interaction between imaginary images. Geometry optimization was applied until the maximum force on each atom was less than 0.002 Hartree/Bohr.

2. RESULTS

2.1. Structural and Dynamical Stability

Before investigating the structural parameters of BSb/Ga₂SSe heterostructures, we have first studied the structural parameters of pristine BSb and Janus Ga₂SSe. The lattice parameters of pristine BSb and Ga₂SSe which are also given in Table 1 are 3.756 Å and 3.752 Å, respectively. The results are compatible with previous reports (Xie et al., 2016; Bui et al., 2019). The lattice mismatch between BSb and Ga₂SSe layers is found to be 0.106%. As presented in Figure 1, six convenient stacking configurations denoted AA1, AA2, AB1, AB2,

AB3, and AB4 are regarded while constituting the BSb/Ga₂SSe heterostructure.

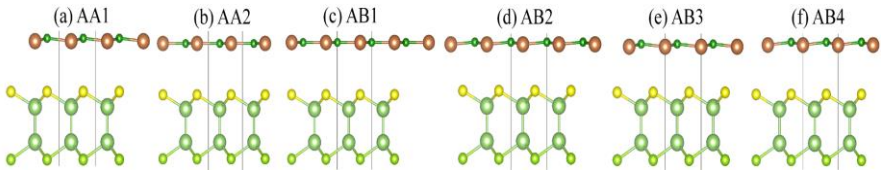


Figure 1. Stacking Patterns Considered for the BSb/Ga₂SSe Heterostructures

The most stable stacking pattern is obtained with the binding energy defined by $E_b = E_{\text{BSb/Ga}_2\text{SSe}} - E_{\text{BSb}} - E_{\text{Ga}_2\text{SSe}}$ where $E_{\text{BSb/Ga}_2\text{SSe}}$, E_{BSb} , and $E_{\text{Ga}_2\text{SSe}}$ represent the total energy of the heterobilayers. As given in Table 1, the most stable stacking model is found to be AB3. The AB3 configuration is presented in Figure 2 (a).

Table 1. The Binding Energies of BSb/Ga₂SSe Heterobilayers for AA1, AA2, AB1, AB2, AB3, and AB4 Stacking Patterns.

Structures	AA1	AA2	AB1	AB2	AB3	AB4
Binding energy (eV)	-0.140	-0.126	-0.122	-0.203	-0.211	-0.135

As can be given in Table 1, the lattice parameter of BSb/Ga₂SSe heterobilayer is found as 3.753 Å. Further, the dynamical stability of the BSb/Ga₂SSe has been examined with the phonon spectrum. As presented in Figure 2 (b), the phonon branches of the AB3 configuration are positive which it can be said the BSb/Ga₂SSe heterostructure is dynamically stable.

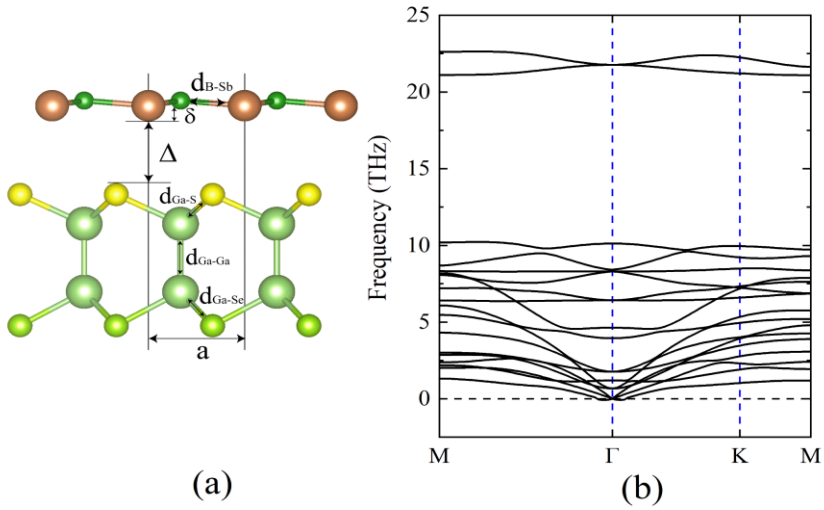


Figure 2. (a) Side View, and (b) Phonon Spectrum of AB3 Stacking Configuration of BSb/Ga₂SSe Heterostructure

Table 2. Structural Parameters of Optimized System.

Material	Lattice constant (Å)	Bond length B-Sb (Å)	Bond length Ga-S (Å)	Bond length Ga-Se (Å)	Interlayer distance (Δ) (Å)	Buckling height (δ) (Å)	Binding energy (eV)
Ga ₂ SSe	3.752	-	2.425	2.506	-	-	-
BSb	3.756	2.171	-	-	-	-	-
BSb/Ga ₂ SSe	3.753	2.175	2.418	2.505	3.870	0.183	-0.211

As shown in Figure 3, the electronic band structure of the BSb/Ga₂SSe heterostructure has a direct semiconducting behavior with a 0.498 eV bandgap value for both PBE and SOC methods. In addition, the

conduction band minimum (CBM) and valence band maximum (VBM) are located at the K point.

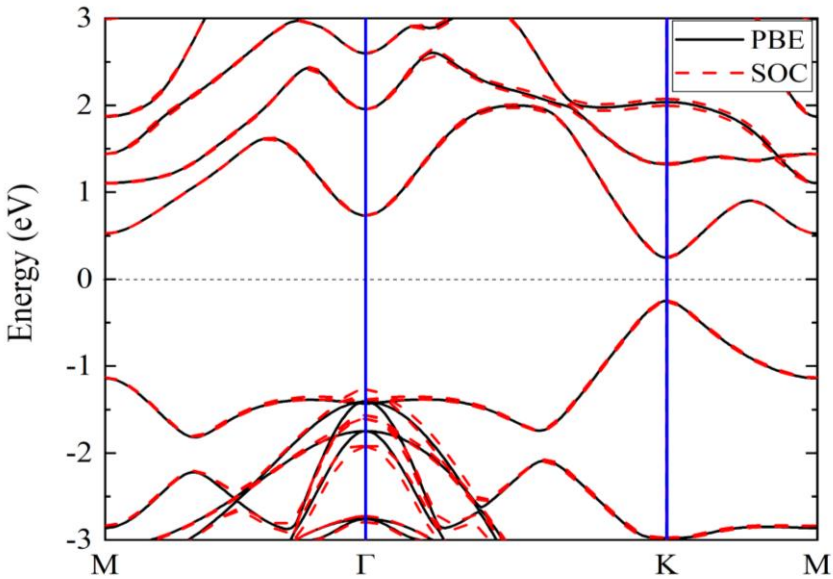


Figure 3. Band Structure of Pristine BSb/Ga₂SSe Heterostructure

2.2. Electric Field Effects on Electronic Structure

Generally, applying an external electric field to vdW heterobilayers has a significant role in modulating electronic properties. Thus, we have investigated the external perpendicular electric field effects on BSb/Ga₂SSe heterostructure. The electronic band diagrams and variations of bandgap under the effect of the external electric field are elucidated in Figure 4 and Table 3, respectively. As given in Table 3, BSb/Ga₂SSe heterostructure bandgap decreases between -3 V/nm (0.521 eV) and 3 V/nm (0.477 eV) with conserving the direct bandgap

peculiarity. Thus, it can be said that the charge transfer is from the Ga₂SSe layer to the BSb layer. Nonetheless, the applied electric field in the positive direction enhances the intrinsic electric field between two layers and increases the charge transfer between Ga₂SSe and BSb layers. Therefore, the bandgap is diminished with increasing charge transfer. Conversely, for the case of the applied negative electric field, the intrinsic electric field and external perpendicular electric field are in different directions. Thus, the charge transfer decreases and the bandgap enhances with decreasing charge transfer.

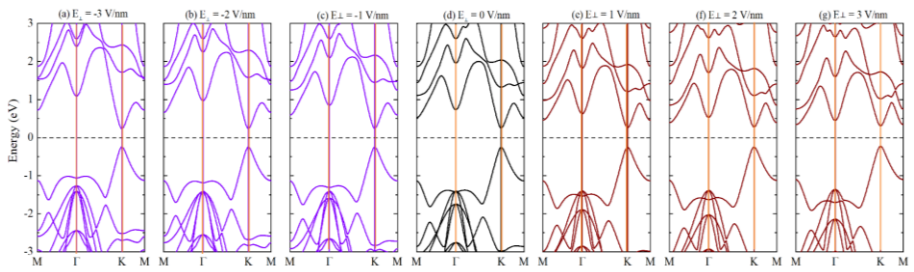


Figure 4. Band Structures of BSb/Ga₂SSe Heterostructure Under Electric Field Effects

Table 3. Variation of Bandgap of BSb/Ga₂SSe Heterostructure With Respect to the Electric Field.

Electric Field (V/nm)	3	2	1	0	-1	-2	-3
Band Gap (eV)	0.521	0.515	0.508	0.498	0.491	0.483	0.477

CONCLUSION

In summary, BSb is investigated with Janus Ga₂SSe heterostructures when there is an external electric field. Six considered stacking patterns of heterostructure have been taken into account. The stable stacking pattern is found to be AB3.

The lattice mismatch between BSb and Ga₂SSe is determined as 0.11%. The BSb/Ga₂SSe heterostructure exhibits direct semiconducting behavior at K point with a bandgap of ~0.50 eV. The electronic bandgap of the BSb/Ga₂SSe heterostructure decreases directly from the negative electric field to the positive electric field, without impairing the bandgap characteristic.

As a result, it is concluded that the BSb/Ga₂SSe heterostructure is a novel material for electro-optical applications owing to its direct bandgap characteristic.

ACKNOWLEDGEMENT

We acknowledge the Ankara University for high performance computing facility through the AYP under Grant No. 17A0443001. This work is supported by the Ankara University BAP under Project No. 21B0443001.

REFERENCES

- Bui, H. D., Jappor, H. R., & Hieu, N. N. (2019). Tunable optical and electronic properties of Janus monolayers Ga₂SSe, Ga₂STe, and Ga₂SeTe as promising candidates for ultraviolet photodetectors applications. *Superlattices and Microstructures*, *125*, 1-7.
- Butler, S. Z., Hollen, S. M., Cao, L., Cui, Y., Gupta, J. A., Gutiérrez, H. R., ... & Goldberger, J. E. (2013). Progress, challenges, and opportunities in two-dimensional materials beyond graphene. *ACS nano*, *7*(4), 2898-2926.
- Castro Neto, A. H., Guinea, F., Peres, N. M. R., Novoselov, K. S., & Geim, A. K. (2009). The electronic properties of graphene. *Reviews of modern physics*, *81*(1), 109-162.
- Geim, A. K., & Novoselov, K. S. (2010). The rise of graphene. In *Nanoscience and technology: a collection of reviews from nature journals* (pp. 11-19).
- Guo, G., Shi, Y., Zhang, Y., Deng, Y., Du, F., Xie, Z., ... & Mao, Y. (2020). First-principles study on the electronic and magnetic properties of P edge-doped armchair germanium selenide nanoribbon. *Computational Materials Science*, *172*, 109348.
- Hu, Y., Zhang, S., Sun, S., Xie, M., Cai, B., & Zeng, H. (2015). GeSe monolayer semiconductor with tunable direct band gap and small carrier effective mass. *Applied Physics Letters*, *107*(12), 122107.
- Hu, Z., Li, Q., Lei, B., Zhou, Q., Xiang, D., Lyu, Z., ... & Chen, W. (2017). Water-catalyzed oxidation of few-layer black phosphorous in a dark environment. *Angewandte Chemie International Edition*, *56*(31), 9131-9135.
- Ji, J., Song, X., Liu, J., Yan, Z., Huo, C., Zhang, S., ... & Zeng, H. (2016). Two-dimensional antimonene single crystals grown by van der Waals epitaxy. *Nature communications*, *7*(1), 1-9.
- Koski, K. J., & Cui, Y. (2013). The new skinny in two-dimensional nanomaterials. *ACS nano*, *7*(5), 3739-3743.

- Lee, Y. T., & Ozaki, T. (2019). OpenMX Viewer: A web-based crystalline and molecular graphical user interface program. *Journal of Molecular Graphics and Modelling*, 89, 192-198.
- Liu, H., Neal, A. T., Zhu, Z., Luo, Z., Xu, X., Tománek, D., & Ye, P. D. (2014). Phosphorene: an unexplored 2D semiconductor with a high hole mobility. *ACS nano*, 8(4), 4033-4041.
- Long, R., & Prezhdo, O. V. (2016). Quantum coherence facilitates efficient charge separation at a MoS₂/MoSe₂ van der Waals junction. *Nano letters*, 16(3), 1996-2003.
- Lu, A. Y., Zhu, H., Xiao, J., Chuu, C. P., Han, Y., Chiu, M. H., ... & Li, L. J. (2017). Janus monolayers of transition metal dichalcogenides. *Nature nanotechnology*, 12(8), 744-749.
- Miró, P., Audiffred, M., & Heine, T. (2014). An atlas of two-dimensional materials. *Chemical Society Reviews*, 43(18), 6537-6554.
- Monkhorst, H. J., & Pack, J. D. (1976). Special points for Brillouin-zone integrations. *Physical review B*, 13(12), 5188.
- Novoselov, K. S., Geim, A. K., Morozov, S. V., Jiang, D. E., Zhang, Y., Dubonos, S. V., ... & Firsov, A. A. (2004). Electric field effect in atomically thin carbon films. *science*, 306(5696), 666-669.
- Ozaki, T. (2003). Variationally optimized atomic orbitals for large-scale electronic structures. *Physical Review B*, 67(15), 155108.
- Ozaki, T., & Kino, H. (2004). Numerical atomic basis orbitals from H to Kr. *Physical Review B*, 69(19), 195113.
- Ozaki, T., & Kino, H. (2005). Efficient projector expansion for the ab initio LCAO method. *Physical Review B*, 72(4), 045121.
- Palsgaard, M., Gunst, T., Markussen, T., Thygesen, K. S., & Brandbyge, M. (2018). Stacked janus device concepts: abrupt pn-junctions and cross-plane channels. *Nano letters*, 18(11), 7275-7281.
- Perdew, J. P., Burke, K., & Ernzerhof, M. (1996). Generalized gradient approximation made simple. *Physical review letters*, 77(18), 3865.

- Radisavljevic, B., Radenovic, A., Brivio, J., Giacometti, V., & Kis, A. (2011). Single-layer MoS₂ transistors. *Nature nanotechnology*, 6(3), 147-150.
- Riis-Jensen, A. C., Deilmann, T., Olsen, T., & Thygesen, K. S. (2019). Classifying the electronic and optical properties of Janus monolayers. *ACS nano*, 13(11), 13354-13364.
- Shang, J., Pan, L., Wang, X., Li, J., Deng, H. X., & Wei, Z. (2018). Tunable electronic and optical properties of InSe/InTe van der Waals heterostructures toward optoelectronic applications. *Journal of Materials Chemistry C*, 6(27), 7201-7206.
- Wang, Y., Huang, P., Ye, M., Quhe, R., Pan, Y., Zhang, H., ... & Lu, J. (2017). Many-body effect, carrier mobility, and device performance of hexagonal arsenene and antimonene. *Chemistry of Materials*, 29(5), 2191-2201.
- Xie, M., Zhang, S., Cai, B., Gu, Y., Liu, X., Kan, E., & Zeng, H. (2017). Van der Waals bilayer antimonene: a promising thermophotovoltaic cell material with 31% energy conversion efficiency. *Nano Energy*, 38, 561-568.
- Xie, M., Zhang, S., Cai, B., Zhu, Z., Zou, Y., & Zeng, H. (2016). Two-dimensional BX (X= P, As, Sb) semiconductors with mobilities approaching graphene. *Nanoscale*, 8(27), 13407-13413.
- Zhang, S., Guo, S., Chen, Z., Wang, Y., Gao, H., Gómez-Herrero, J., ... & Zeng, H. (2018). Recent progress in 2D group-VA semiconductors: from theory to experiment. *Chemical Society Reviews*, 47(3), 982-1021.
- Zhang, S., Xie, M., Li, F., Yan, Z., Li, Y., Kan, E., ... & Zeng, H. (2016). Semiconducting group 15 monolayers: a broad range of band gaps and high carrier mobilities. *Angewandte Chemie*, 128(5), 1698-1701.
- Zhang, S., Yan, Z., Li, Y., Chen, Z., & Zeng, H. (2015). Atomically thin arsenene and antimonene: semimetal–semiconductor and indirect–direct band-gap transitions. *Angewandte Chemie*, 127(10), 3155-3158.
- Zhou, W., Guo, S., Liu, X., Cai, B., Song, X., Zhu, Z., & Zhang, S. (2018). Stability enhancement and electronic tunability of two-dimensional SbIV compounds via surface functionalization. *Applied Surface Science*, 427, 363-368.

- Zhu, J., Ha, E., Zhao, G., Zhou, Y., Huang, D., Yue, G., ... & Zhao, P. (2017). Recent advance in MXenes: a promising 2D material for catalysis, sensor and chemical adsorption. *Coordination Chemistry Reviews*, 352, 306-327.
- Zhu, Z., & Tománek, D. (2014). Semiconducting layered blue phosphorus: a computational study. *Physical Review Letters*, 112(17), 176802.
- Note:** IZDAS 2021, 1st International Conference of Physics, August 17, 2021, Ankara, Turkey. (The results are presented at the symposium)

CHAPTER 7

INVESTIGATION OF THE EFFECT OF LAMBDA CYHALOTHRIN ON SOME EGGSHELLS AS WASTE MATERIAL USING AFM IMAGING AND UV-VIS SPECTROSCOPY¹

Assist. Prof. Dr. Neslihan KAYA KINAYTÜRK² & Prof. Dr. Belgin
TUNALI³ & Assist. Prof. Dr. Deniz TÜRKÖZ ALTUĞ⁴

¹ This work was presented as a summary paper at the 3rd International 23 April Scientific Studies Congress.

² Burdur Mehmet Akif Ersoy University, Faculty of Arts and Sciences, Department of Nanoscience and Nanotechnology, Burdur Mehmet Akif Ersoy University, Burdur, Turkey. nkinayturk@mehmetakif.edu.tr, ORCID ID: 0000-0002-2170-1223

³ Burdur Mehmet Akif Ersoy University, Faculty of Arts and Sciences, Department of Nanoscience and Nanotechnology, Burdur Mehmet Akif Ersoy University, Burdur, Turkey. btunali@mehmetakif.edu.tr, ORCID ID: 0000-0003-0768-679X

⁴ Isparta Vocational School of Health Services, Süleyman Demirel University, East Campus, Isparta 32260, Turkey. denizturkoz@sdu.edu.tr, ORCID ID: 0000-0002-1861-6263

INTRODUCTION

Lambda Cyhalothrin (LC) is a synthetic pyrethroid (Bownik et al., 2019; Bille et al., 2017). Also, LC is an agricultural pesticide used against insect infestations in the cultivation of many basic food products such as corn, cotton, potatoes, olives, pistachios, wheat. This insecticide can be applied to the product to be grown 2 to 5 times, with an interval of approximately 15 days, depending on the type of product (Ministry of Agriculture and Forestry). Firstly, by spraying, the quality of the grown product can be increased by eliminating various larvae and eggs on the plant. During spraying, the chemical can reach not only the plant but also unwanted areas, especially in windy weather. Residues of this chemical have been detected in water sources in various regions (Bownik et al., 2019; Bille et al., 2017). After spraying precipitation and irrigation, these chemicals can be carried from the soil to groundwater and from there to lakes and seas, causing adverse effects on aquatic organisms and invertebrates. (Bille et al., 2017; Khalil et al., 2020; Saylar, 2016; Brogan and Relye, 2017). With this negatively affect, the ecosystem balance may deteriorate over time.

Eggshells are porous materials (Chousalkar and Roberts, 2012). In recent years, they were used in many studies to remove harmful substances from the environment by pure form or activated form of eggshell in terms of having this porous structure feature (Dayanidhi et al., 2020; Ravi and Sundararaman, 2020; Sankaran et al., 2020; Almeida et al., 2020; Pérez et al., 2021; Lin et al., 2021). Eggshells used in this way have attracted a lot of attention in recent years in

terms of both being an inexpensive method and not harming to the environment.

In our study, LC which was used to prevent insect infestation of a wide variety of basic agricultural products in our country and all around the world, experimental studies carried out to partially prevent it from reaching undesirable areas by using eggshells (Denizli Hen (DH), Light Brahma Chicken (LBC), ISA Tinted -White (ITW), Alectoris Chukar (AC) and Coturnix Coturnix Japonica (CCJ) eggshells). Thus, it will be possible to protect the environment from this chemical as much as possible.

1. MATERIALS and METHODS

1.1. Materials and Chemical

Eggshell samples (DH, LBC, ITW, AC and CCJ) were taken from incubation wastes of hatched chicks produced and researched by Isparta University of Applied Sciences, Education Research and Application Farm.

Insecticide LC: it was produced by Syngenta Crop Protection AG and was purchased from Turkey. No purification was done for LC in this study. The molecular structure of it presented in Figure 1. The molecular formula of LC is $C_{23}H_{19}ClF_3NO_3$. Chemical name of LC is (R + S)- α -cyano-3-(phenoxyphenyl) methyl-(1S + 1R)-cis-3-(2-chloro-3,3,3-trifluoroprop-1-enyl)-2,2-dimethyl-cyclopropane-carboxylate (Çelik et al., 2003).

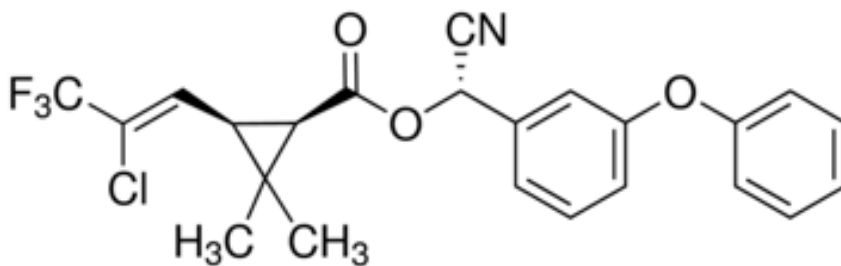


Figure 1: Molecular Structure of LC

1.2. Sample Preparation

Four-stage cleaning was applied to remove impurities from the eggshells. In the first stage, eggshells were boiled at 200°C for 2 hours and the inner membrane was peeled off the shell. In the second stage, eggshell was boiled with distilled water for 1 hour. In the third stage, after waiting for 30 minutes in an ultrasonic bath, in fourth and the last stage, it was washed with acetone and dried at room temperature on filter paper to remove the residues.

Before the adsorption process for the characterization of the dried eggshells; approximately 0.5 cm² pieces of the pure forms were separated to take AFM images, AFM images were recorded at 250x250 pixel resolution in non-contact mode on the XE-Series Park Systems device.

1.3. Adsorption Study

15 mL-250 ppm LC was added to the eggshells weighing 0.15 g each. UV-Vis analysis were performed in Shimadzu -1280 device by applying 5 ppm dilution in 10 different time periods (15th Minutes, 2nd, 4th, 6th, 8th, 12th, 24th, 28th, 32nd and 48th hours) had done.

After, the adsorption study, process was applied to approximately 0.5 cm² eggshell, AFM analyzes were performed to find out any changes in surface morphology if it were occurred.

1.4. Desorption Study

After 48 hours of adsorption study, the samples were dried. 10 mL of distilled water was added by weighing 0.01 g of each sample. Then, the samples were performed by UV-Vis spectra at 6 different times in a 24-hour period.

2. RESULTS and DISCUSSION

2.1. AFM Analysis

AFM images of the eggshells before and after the adsorption process were compared. They were shown to Figure 2.

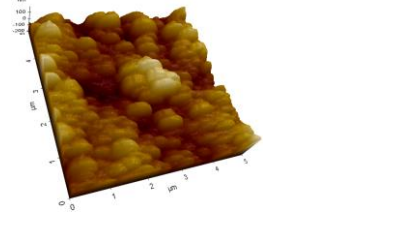
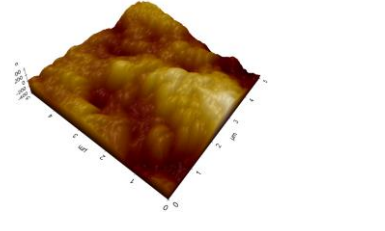
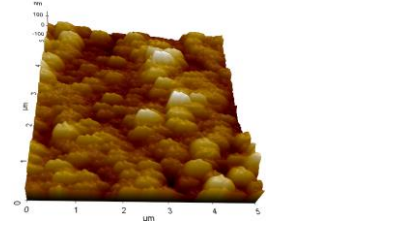
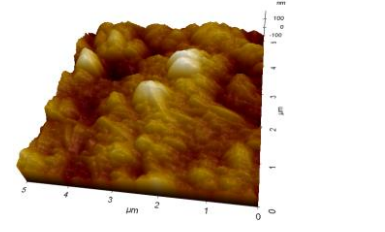
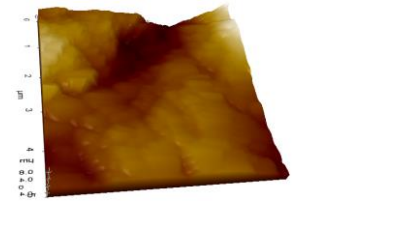
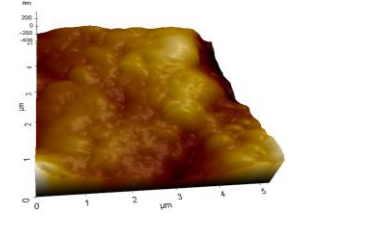
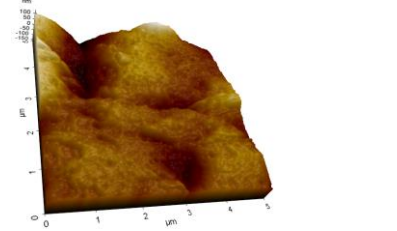
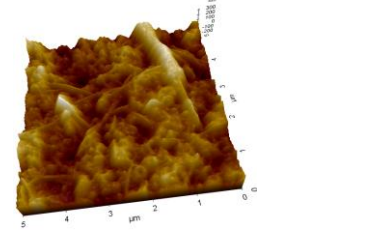
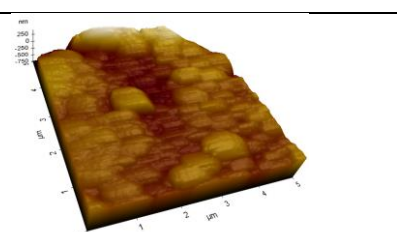
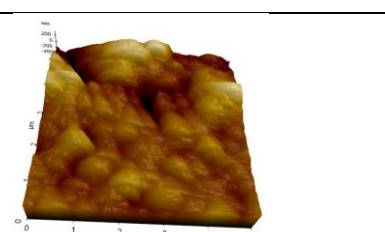
	Before adsorption	After adsorption
DH		
LBC		
ITW		
AC		
CCJ		

Figure 2: AFM Images of Eggshell Samples Before and After Adsorption

When Figure 2 was examined, it was observed that the pure forms of DH and LBC have a bubble structure, while ITW, AC and CCJ have a flatter appearance compared to the others. It is observed that LC accumulates in the pores of DH, LBC, ITW and CCJ samples after the adsorption process, and even the pores disappear and display a flatter appearance. On the other hand, On the AC eggshell, it is seen that LC accumulates in a crystalline form.

2.2. UV-Vis Spectroscopic Analysis Results

UV-Vis spectroscopic analysis technique was used to determine the amount of insecticides adhere to eggshells. In this technique, measurements were taken at 10 different time intervals and quantification was made with the help of a calibration chart.

The adsorption (%) of the amount of insecticide in the solution was calculated using Equation 1 and the amount of LC adsorbed per unit weight at equilibrium (q_e) Equation 2 using the formulas. In this study, the amount of desorption (%) was calculated using Equation 3.

$$\text{Adsorption}(\%) = \left(\frac{(C_i - C_e)}{C_i} \right) \times 100 \quad (1)$$

$$q_e = \left(\frac{(C_i - C_e)V}{m} \right) \quad (2)$$

$$\text{Desorption}(\%) = (C_d/C_a) \times 100 \quad (3)$$

In the equations, C_i and C_e are the LC concentration of initial and final status of adsorption, respectively (mgL^{-1}), V ; total volume (mL), m ; the amount of adsorbent used, C_d , is the LC concentration after desorption, and C_a is the adsorbed LC concentration.

Time-dependent changes of adsorption capacities, q_e value and desorption capacities, for LC on eggshell samples are given in Figure 3, Figure 4, and Figure 5, respectively. While the adsorption of the insecticide on the eggshells increased rapidly in the first 12 hours, the adsorption process was completed by transitioning to the steady state after the 24th hour. The LC, percentage of adsorption of ITW, DH, LBC, AC, and CCJ eggshells were calculated as 26.2, 24.8, 28.6, 29.9 and 30.3 %, respectively. When the quantity of insecticides adsorbed by different eggshells were compared, it was seen that the highest amount adsorption capacity belongs to CCJ eggshell with 7.6 mg. The desorption study was performed at 6 different time intervals, and it was observed that the desorption process reached equilibrium in 12 hours. In the literature search, it was seen that the percentage of desorption varied between 5% and 70%. (Chattoraj et al., 2018; Mittal et al., 2016; Sabah et al., 2018). When the data on the percentage of desorption were examined in this study, it was determined that the percentages of desorption in all eggshells varied between 1.8% and 3.3%. The low desorption data indicate that the LC adsorbed by the eggshells is not released back into nature and completely adheres to the pores of the eggshells. Low desorption capacity can be considered as an advantage.

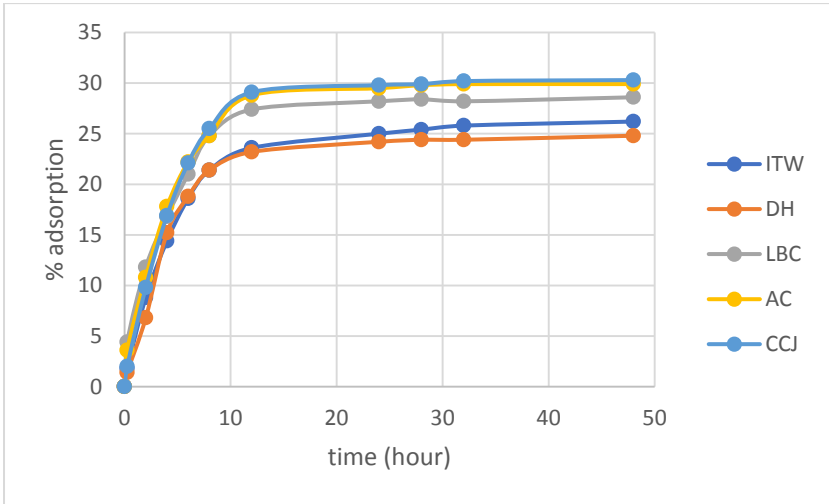


Figure 3: Time Dependent % Adsorption Graph

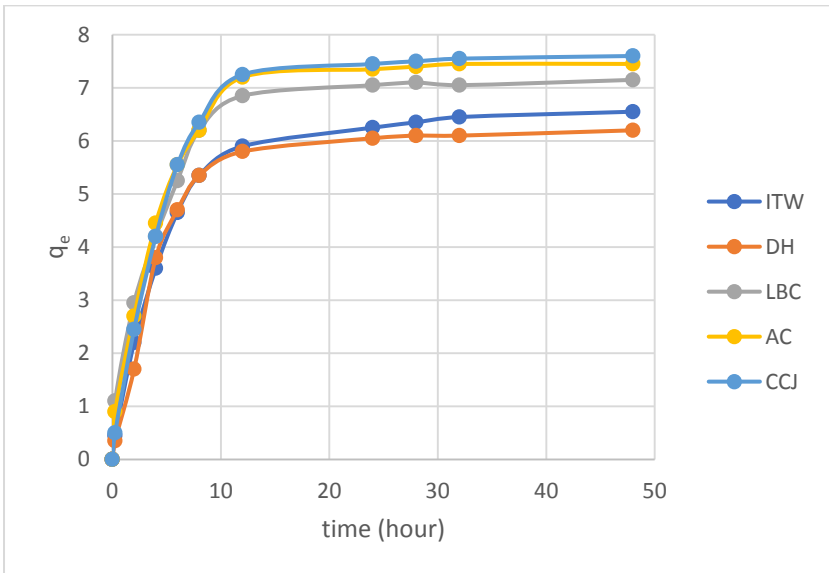


Figure 4: Time Dependent q_e Values Graph

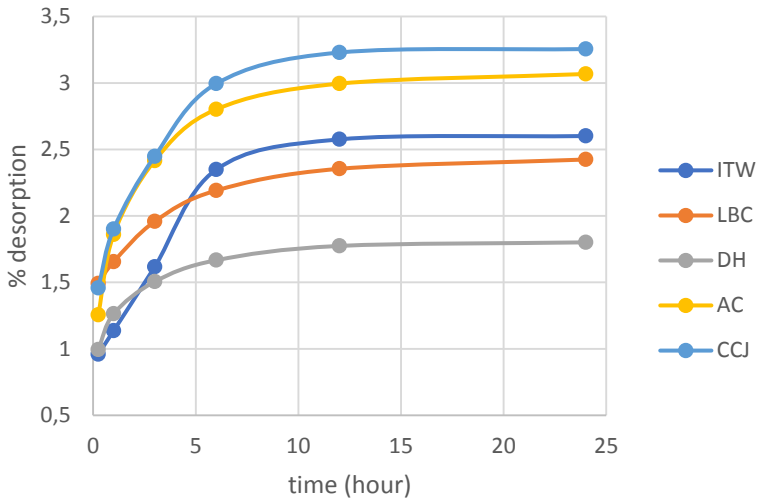


Figure 5: Time Dependent % Desorption Amount Graph

CONCLUSION

In this study, various eggshells were exposed to Lambda Cyhalothrin (LC) and the changes on the samples were analyzed by AFM imaging and UV-Vis spectra. Before the adsorption, the surface morphology of the eggshells had a porous structure, but after the adsorption process, these pores were closed and even agglomeration was observed. By the way evaluating the UV-Vis spectroscopic data, it was concluded that the average adsorption capacity of the eggshells was 28%. The adsorption and desorption process were investigated with the UV-Vis spectroscopic technique, and it was seen that they desorption process was completed after 12 hours. The desorption amount was calculated as 2.6, 2.4, 1.8, 3.1 and 3.3 for ITW, LBC, DH, AC and CCJ, respectively. According to the adsorption and desorption data, it was observed that LC mostly adhered and released on the CCJ. Thus, the

low amount of desorption is an indication that harmful pesticides cannot be easily released into the nature. For this reason, eggshells are a good adsorbent choice as they do not easily release LC pesticide into the nature, as well as organic and harmless to the environment.

REFERENCES

- Almeida, P. V., Santos, A. F., Lopes, D. V., Gando-Ferreira, L. M., Quina, M. J. (2020). Novel adsorbents based on eggshell functionalized with iron oxyhydroxide for phosphorus removal from liquid effluents. *Journal of Water Process Engineering*, Vol.36, No.101248, pp 1-9
- Bille, L., Binato, G., Gabrieli, C., Manfrin, A., Pascoli, F., Pretto, T., . . . Arcangeli, G. (2017). First report of a fish kill episode caused by pyrethroids in Italian freshwater. *Forensic Sci. Int.*, Vol.281, pp 176-182
- Bownik, A., Kowalczyk, M., Bańcerowski, J. (2019). Lambda-cyhalothrin affects swimming activity and physiological responses of *Daphnia magna*. *Chemosphere*, Vol.216, pp 805-811
- Brogan, W. R., Relye, R. A. (2017). Multiple mitigation mechanisms: effects of submerged plants on the toxicity of nine insecticides to aquatic animals. *Environmental Pollution*, Vol.200, pp 688-695
- Chattoraj, S., Mondal, N.K., Sen, K. (2018). Removal of carbaryl insecticide from aqueous solution using eggshell powder: a modeling study. Vol.8, No.163, 1-9
- Chousalkar, K., Roberts, J. (2012). Recovery of *Salmonella* from eggshell wash, eggshell crush, and egg internal contents of unwashed commercial shell eggs in Australia. *Poultry Science*, Vol.91, No.7, pp 1739-1741
- Çelik, A., Mazmanci, B., Çamlıca, Y., Aşkin, A., Çömelekoğlu, Ü. (2003). Cytogenetic effects of lambda-cyhalothrin on Wistar rat bone marrow. *Mutation Research/Genetic Toxicology and Environmental Mutagenesis*, Vol.539, No.1-2, pp 91-97
- Dayanidhi, K., Vadivel, P., Jothi, S., Eusuff, N. S. (2020). Facile synthesis of Silver@Eggshell nanocomposite: A heterogeneous catalyst for the removal of heavy metal ions, toxic dyes and microbial contaminants from water. *Journal of Environmental Management*, Vol. 271, No.110962, pp 1-10
- Sabah, H., Thouraya, T., Melek, H., Nadia, M. (2018). Application of response surface methodology for optimization of cadmium ion removal from an

- aqueous solution by eggshell powder. *Chemical research in Chinese universities*, Vol. 34, No.2, pp 302-310
- <https://bku.tarimorman.gov.tr/AktifMadde/Details/313>. (02.04.2021).
- Khalil, S. R., Elhakim, Y. A., El-fattah, A. H., Farag, M. R., El-Hameed, N. E., EL-Murr, A. E. (2020). Dual immunological and oxidative responses in *Oreochromis niloticus* fish exposed to lambda cyhalothrin and concurrently fed with Thyme powder (*Thymus vulgaris* L.): Stress and immune encoding gene expression. *Fish & Shellfish Immunology*, Vol.100, pp 208-218
- Lin, T.-Y., Chai, W. S., Chen, S.-J., Shih, J.-Y., Koyande, A. K., Liu, B.-L., Chang, Y.-K. (2021). Removal of soluble microbial products and dyes using heavy metal wastes decorated on eggshell. *Chemosphere*, Vol.270, No.128615, pp 1-12
- Mittal, A., Teotia, M., Soni, R.K., Mittal, J. (2016). Applications of Egg Shell and Egg Shell Membrane as Adsorbents. A Review, *Journal of Molecular Liquids*, Vol.223, pp 376-387
- Pérez, S., Muñoz-Saldaña, J., Acelas, N., Flórez, E. (2021). Phosphate removal from aqueous solutions by heat treatment of eggshell and palm fiber. *Journal of Environmental Chemical Engineering*, Vol.9, No.104684, pp 1-11
- Ravi, T., Sundararaman, R. (2020). Synthesis and characterization of chicken eggshell powder coated magnetic nano adsorbent by an ultrasonic bath assisted co-precipitation for Cr(VI) removal from its aqueous mixture. *Journal of Environmental Chemical Engineering*, Vol. 8, No.103877, pp 1-11
- Sankaran, R., Show, P. L., Ooi, C.-W., Ling, T. C., Shu-Jen, C., Chen, S.-Y., Chang, Y.-K. (2020). Feasibility assessment of removal of heavy metals and soluble microbial products from aqueous solutions using eggshell wastes. *Clean Technologies and Environmental Policy*, Vol. 22, pp 773-786
- Saylar, Ö. (2016). Toxic effects of permethrin on *Pseudorasbora parva*. *Journal of environmental biology*, Vol.37, No.6, pp 1247-1253



ISBN: 978-625-7562-96-6